PERFORMANCE STUDIES AND RECEIVER DESIGN OF A MB-OFDM UWB SYSTEM

PNG KHIAM BOON

(B.Eng. (Hons), National University Of Singapore)

A THESIS SUBMITTED

FOR THE DEGREE OF MASTER OF ENGINEERING

DEPARTMENT OF ELECTRICAL & COMPUTER ENGINEERING

NATIONAL UNIVERSITY OF SINGAPORE

2005

Acknowledgements

I like to express my gratitude to all who have helped me in the course of pursuing my post graduate degree. I am grateful to my supervisors Dr Francois Chin Po Shin and Mr Peng Xiaoming for broadening my research horizons and their encouragement and valuable advice during my time with them. Also, I like to thank my colleagues and friends in the Institute for Infocomm Research (I^{2}R) for their valuable insights and suggestions.

Table of Contents

Acknowledgements i

Table of Contents ii

Summary iv

List of Tables vi

List of Figures vii

Chapter 1: Introduction 1

- 1.1 Overview ………………………………………………………. 1
- 1.2 Contributions …………………………………………………... 5
- 1.3 Outline of Thesis ……………………………………………. 6

Chapter 2: MB-OFDM UWB System 7

- 2.1 MB-OFDM UWB System ………………………………….... 7
- 2.2 Channel Models ……………………………………………... 20
- 2.3 Conclusions …….……………………………………………… 22

Chapter 3: Simplified LDPC Code Design for MB-OFDM UWB System 23

- 3.1 Simplified LDPC Codes ……………………………...…… 24
- 3.2 Performance Studies ……………………………………..... 33
- 3.3 Conclusions …….…………………………………………….. 39

Chapter 4: Chip Interleaved Scheme for MB-OFDM UWB System 40

- 4.1 Direct Spreading with Chip Interleaving Scheme for MB-OFDM UWB System …………………………...…….. 41
- 4.2 Performance Studies ……………………………………..... 50
- 4.3 Conclusions …….…………………………………………….. 55

Chapter 5: Frequency Offsets Estimation and Compensation 56

- 5.1 Effects of Frequency Offset …………………………………... 56

5.2 Conventional Frequency Offset Estimation and Compensation 62
5.3 A Novel Joint Frequency Offset Estimation Method ……….. 66
5.4 Performance Studies ……………………………………….. 78
5.5 Conclusions ………………………………………………….. 84

Chapter 6: A Practical Receiver Design for MB-OFDM UWB System 85
6.1 Symbol Synchronization ……………………………………... 85
6.2 Channel Estimation and Equalization ………………………... 89
6.3 Frequency Offset Estimation and Compensation …………… 93
6.4 Practical Receiver Design…………………………………….. 93
6.5 Performance Studies ……………………………………….. 96
6.6 Conclusions ………………………………………………….. 99

Chapter 7: Conclusions and Future Works 101
7.1 Thesis Conclusions ...……………………………………… 101
7.2 Future Works ……………………………………………… 103

Appendix A. Preambles for MB-OFDM UWB System 104

References 112

List of Publications 116

Note 117

Summary

Multi-bands Orthogonal Frequency Division Multiplexing (MB-OFDM) is an effective modulation technique for the Ultra-wideband (UWB) personal area networks (WPANS) protocols. In this thesis, we investigate an alternate error-correcting code, LDPC, as well as a chip interleaving scheme to improve the performance of the proposed MB-OFDM UWB System. We also propose a novel joint carrier and sampling frequency offset estimation algorithm and investigate the receiver design for the proposed system featuring synchronization and channel estimation algorithm in additions to the novel frequency offset estimation algorithm.

Frequency offset between transmitter and receiver clocks in a MB-OFDM UWB system results in serious distortion of the received signal and hence affects the overall performance of the system. A novel algorithm to estimate the frequency offset in a transceiver system with fixed-rate clock, which is simple to implement and perform better than the conventional algorithm, is introduced. The algorithm uses the iterative averaging of the estimates calculated using pilot sub-carriers from individual OFDM symbols to improve the overall estimation accuracy for subsequent received OFDM symbols. A method to counter the phase-wrapping effects based on maximum likelihood principles is also described as part of the algorithm. The mean-squared error of the estimates is significantly reduced using the algorithm especially for long packets. Moreover, the use of the iterative averaging algorithm helps to limit the performance degradation due to frequency offset to less than 1 dB and also achieves very significant performance gain over conventional algorithm. The proposed novel algorithm is incorporated together with other sub-systems such as channel estimator and symbol synchronization system to form a practical receiver design. The performance of the receiver design is tested using simulation and compared to the performance of a receiver in ideal conditions. Results show that the receiver performs well with relatively small performance degradation.

We also designed a simplified low-density parity-check (LDPC) code for the proposed MB-OFDM UWB system, which improves the system performance for high data rate transmission. The LDPC codes, which are designed using a decoder approach, allowed the use of a simpler, more structured decoder design that can be implemented much more easily. Moreover, the use of LDPC code eliminates the need of bits interleaver to counter burst errors which are common in fading channel as the LDPC code are robust to burst errors. Through Monte Carlo simulation, the designed LDPC code was shown to improve the system performance significantly giving a performance gain of 2 to 4 dB when compared to the proposed system using convolutional codes.

A direct spreading with chip interleaving scheme is also applied to the MB-OFDM UWB system and found to improve the system performance for high data rate transmission. The scheme can be easily implemented using simple block interleaver and banks of adders at the transmitter while a simplified form of maximum likelihood detection can be used at the receiver. The proposed scheme achieves a performance gain between 1.5 dB and 5.1 dB depending on the spreading factor used.

List of Tables

Table 2.1: Sub-bands Allocation for MB-OFDM UWB System 8

Table 2.2: Time-Frequency Codes (TFC) for Mode 1 Transmission 9

Table 2.3: Transmission Rate and Related Parameters 11

Table 2.4: Scrambler Initialization Sequence 14

Table 2.5: QPSK Encoding Table 16

Table 2.6: Allocation of Sub-carriers Frequency 18

Table 2.7: Allocation of Guard Sub-carriers Frequency 19

Table 3.1: Salient Features of Simulated System 36

Table 3.2: Number of bit additions for Convolutional and LDPC Code Encoder 38

Table 3.3: Number of real operations for Convolutional and LDPC Code Decoder 38

Table 4.1: Salient Features of Simulated System 53

Table 5.1: Simulation Scenarios for MB-OFDM UWB System. 79

Table 5.2: Salient Features of Simulated System 80

Table 6.1: Simulation Scenarios for MB-OFDM UWB System. 96

Table A.10: Time Frequency Codes and Associated Preamble Patterns. 104

Table A.11: Preamble Cover Sequence. 105

Table A.12: Time-domain Packet Synchronization Sequence for Preamble Pattern 1. 106

Table A.13: Time-domain Packet Synchronization Sequence for Preamble Pattern 2. 107

Table A.14: Time-domain Packet Synchronization Sequence for Preamble Pattern 3. 108

Table A.15: Time-domain Packet Synchronization Sequence for Preamble Pattern 4. 109

Table A.16: Time-domain Packet Synchronization Sequence for Preamble Pattern 5. 110

Table A.17: Frequency Domain Channel Estimation Preamble Sequence. 111

List of Figures

Figure 1.1: UWB Spectral Mask for Indoor Communications Systems. 1

Figure 2.1: Transmission of OFDM Symbols using TFC#1. 9

Figure 2.2: Block Diagram of MB-OFDM UWB Transmitter. 13

Figure 2.3: Puncturing Patterns. 14

Figure 3.1: Example of a bipartite graph representation for a LDPC code. 25

Figure 3.2: Flowchart of Sum-Product Decoding Algorithm. 28

Figure 3.3: A simplified partly parallel (3,k)-regular LDPC decoder architecture. 29

Figure 3.4: Structure of Deterministic Matrices $\mathbf{H}_0$ and $\mathbf{H}_1$. 31

Figure 3.5: Girth Average Histogram of LDPC Codes Ensemble. 32

Figure 3.6: Block Diagram of MB-OFDM UWB System using LDPC Codes. 34

Figure 3.7: PER Performances for MB-OFDM UWB System in CM1. 35

Figure 3.8: PER Performances for MB-OFDM UWB System in CM3. 35

Figure 4.1: Chip Interleaving Scheme for MC-CDMA. 43

Figure 4.2: Frequency Spreading for MB-OFDM. 44

Figure 4.3: Chip Interleaving for MB-OFDM. 45

Figure 4.4: MB-OFDM UWB System with Direct Spreading and Chip-interleaving 51

Figure 4.5: PER Performances for MB-OFDM UWB System in CM1. 54

Figure 4.6: PER Performances for MB-OFDM UWB System in CM3. 54

Figure 5.1: Flowchart of Frequency Offset Estimation and Compensation Algorithm. 71

Figure 5.2: The Wrapping Effect of Measured Phase. 75

Figure 5.3: Correction for Wrapping Effect of Measured Phase. 75

Figure 5.4: Mean-Squared Error of Estimated Normalized Carrier Frequency Offset 77

Figure 5.5: Mean-Squared Error of Estimated Phase Distortions. 77

Figure 5.6: PER Performance of 480 Mbps Transmission in CM1. 80

Figure 5.7: PER Performance of 200 Mbps Transmission in CM2. 81

Figure 5.8: PER Performance of 106.7 Mbps Transmission in CM4. 81

Figure 5.9: PER Performance of 53.3 Mbps Transmission in CM4. 82

Figure 6.1: Autocorrelation Function of x_j. 88

Figure 6.2: Block Diagram of LS-DFT Estimator. 91

Figure 6.3: Block Diagram of Receiver Design. 95

Figure 6.4: PER Performance of 480 Mbps Transmission in CM1. 97

Figure 6.5: PER Performance of 200 Mbps Transmission in CM2. 98

Figure 6.6: PER Performance of 106.7 Mbps Transmission in CM4. 98

Chapter 1

Introduction

Ultra-Wideband (UWB) technology has received a lot of attentions recently [1] and has been widely regarded as a promising solution for future short-range indoor wireless communication applications. Traditionally, UWB technology refers to the use of short-pulse waveforms with a large fractional bandwidth [2]. However, the Federal Communication Commission's (FCC) Report and Order (R&O), adopted 14 Feb 2002 [1] defines UWB as any signal that occupies a spectral frequency band of more than 500 MHz in the allocated 3.1GHz – 10.6 GHz band and meets the specified spectrum mask as illustrated in Figure 1.1.

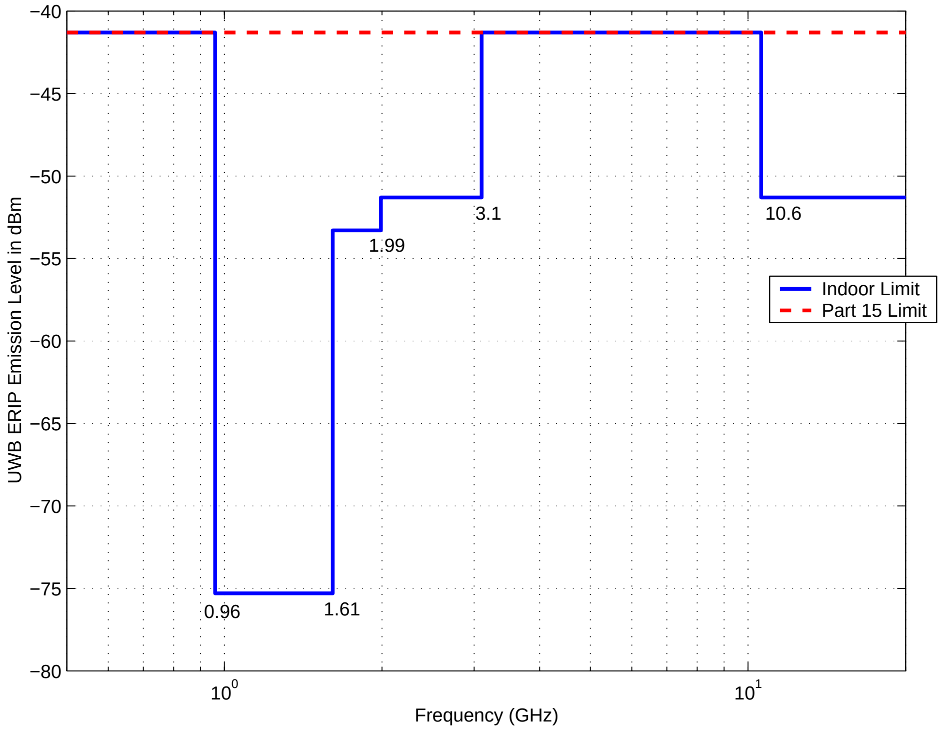

Figure 1.1: UWB Spectral Mask for Indoor Communications Systems.

With the adoption of this new definition by FCC, the view of UWB is shifted from that as a specific technology (i.e. short-pulse radio) to that as an available spectrum for unlicensed use [3]. As such, any transmission signal that satisfies the FCC's requirements for the UWB spectrum can be considered UWB technology. Using this new insight, a group of industry leaders proposed a Multi-band Orthogonal Frequency Division Multiplexing (MB-OFDM) physical layer proposal for IEEE 802.15 Wireless Personal Area Networks (WPAN) Task Group 3a [4]. In this thesis, we will look into the design of a practical receiver that conforms to the specifications given in [4] as well as discuss the possible improvements to the proposed system and analyses the performance of the transceiver through Monte Carlo simulations.

1.1 Overview

The proposed MB-OFDM UWB system essentially partitioned the available UWB spectrum into smaller frequency sub-bands of bandwidth greater than 500 MHz to satisfy FCC's definition and uses OFDM modulation in each sub-bands for transmission. By employing the multi-bands approach, commercially available communication systems can easily be adapted for the UWB indoor communication system. Other advantages of the multi-bands approach include the highly attractive features of scalability and ease of adapting to different radio regulations worldwide. Each sub-band can be treated like a basic building block of the communication system and can be combined in different configurations to help the co-existence of the system with present and future licensed radio services. For the proposed system, each sub-band can be treated as a wideband OFDM transmission system. Multiple accesses can be achieved through defining different hopping sequence between sub-bands for the different users.

The usage of OFDM for each sub-band has great significance in implementation as it can capture the energy in a dense multi-path environment effectively and has the benefit of comparatively low complexity with the use of fast Fourier transform (FFT) algorithms [5]. As an OFDM system in essence, MB-OFDM UWB system transmits data using parallel narrowband sub-carriers within each sub-band. The inter-symbol interference (ISI) in OFDM can be eliminated by adding either a cyclic prefix (CP) or zero prefix (ZP) of duration longer than the anticipated delay spread of the channel. The ability to perform equalization in a multi-paths environment with relatively large bandwidth-delays spread product using a single-tap equalizer in the frequency domain is another critical advantage of OFDM technology [6].

However, OFDM technology does have its disadvantages especially in terms of practical implementation of transceiver. As an OFDM signal is basically a superposition of a large number of modulated sub-carrier signals, it is prone to high instantaneous signal peak with respect to the average signal level. To prevent this high peak-to-average ratio (PAPR) from causing high out-of-band harmonic distortion without the use of a power amplifier with extremely high linearity across the signal level range at the transmitter, clipping have to be performed [5]. This will result in the distortions of the transmitted signal causing degradation in performance. Moreover, studies have shown that time and frequency synchronization accuracy between transmitter and receiver is of paramount importance for the good performance of an OFDM system [5][7][8][9]. A practical MB-OFDM UWB receiver for the proposed system would hence need to be designed so as to ensure minimal performance degradation with manageable complexity. The thesis is devoted to investigations and analysis of such a design.

Another point of contention regarding the proposed MB-OFDM UWB system is the choice of forward error-correcting codes (FEC) employed. For an uncoded OFDM system operating in a multi-paths environment, some of the sub-carriers will experience deep fade and be completely lost. This cause the overall bit error rate to be dependent on the signal-to-noise ratio (SNR) of the weakest sub-carrier and is hence undesirable. To solve the problem, powerful error-correcting codes need to be applied to ensure that the overall bit error rate is dependent on the average received power and not that of the weakest sub-carriers [6]. Therefore, the choice of error-correcting codes is essential in determining the performance of the MB-OFDM UWB system. Due to the implementation limitation, convolutional code is currently considered as the error-correcting code for the proposed MB-OFDM UWB system. Investigations into the use of an alternative code, the low density parity-check (LDPC) code, in the proposed system will be carried out.

Performance of the proposed MB-OFDM UWB system for high data rate transmission are considerably worse than then low rate transmission due to the need to employ high rate FEC. A method that incorporates direct spreading code division multiplexing access (DS-CDMA) with OFDM to improve the system performance is investigated. A novel direct spreading in frequency domain with chip interleaving scheme is found to improve the system performance for high rate transmission. The performance gain is due to the use of the frequency diversity within the frequency selective channel. Simulation results show that the performance gain using the proposed scheme is very significant especially in channel with small coherence bandwidths.

1.2 Contributions

In the first part of the thesis, we discuss and demonstrate the improvement in performance of the MB-OFDM UWB system through the use of a simplified LDPC code and a direct spreading scheme. The 2 schemes are described in details and the performance improvement to the system is discussed with reference to simulated results.

In the second part of the thesis, the emphasis is on the design of a practical transceiver that conforms to the proposed system’s standards. Research on various methods to handle the problems encountered by practical receiver such as packet synchronizations, channel estimations and frequency synchronizations are carried out. New algorithms to handle the problems, which exploited the band-hopping characteristics of the proposed MB-OFDM UWB system, will also be presented. Furthermore, a final joint design of a practical receiver that synthesizes elements from the different sub-systems will be featured.

1.3 Outline of Thesis

This chapter provides the overviews of the research topics and the main contributions made. The rest of the thesis is divided into 6 chapters, each touching on different aspects of the research topics. In Chapter 2, the proposed system and the channel models used for evaluation of the system in [4] will be introduced briefly with emphasis on the salient features. The evaluation criterion, which is used consistently throughout the thesis to determine the performance of the system, will also be covered in details. From Chapter 3 onwards, the discussion in each chapter will concentrate on one of the different research topics covered in the thesis. As such, each chapter will contain the appropriate literature survey on the topic covered as well as the research work, which includes analysis and simulation studies that has been carried out.

In Chapter 3, the emphasis will be on the discussion and evaluation of the performance of a MB-OFDM UWB system using a simplified LDPC codes as an alternative error-correcting codes. In Chapter 4, the discussion is on the direct spreading with chip interleaving scheme for MB-OFDM UWB system. In Chapter 5, discussion will be centered on the frequency offset estimations and compensation methodology of the MB-OFDM UWB system. In Chapter 6, we will concentrate on the discussion of achieving accurate timing and channel estimation as well as present a joint design which incorporates the different elements covered in Chapter 5 and Chapter 6 and highlights the conditions for the synthesis of the sub-systems. Lastly, conclusions of the research works that have been done are given in Chapter 7.

Chapter 2

MB-OFDM UWB System for UWB Communications

The authors in [4] proposed a Multi-bands Orthogonal Frequency Division Multiplexing (MB-OFDM) system for short-range wireless indoor communications using FCC's defined unlicensed ultra-wideband (UWB) spectrum. In this chapter, the salient features of the proposed system will be highlighted. The UWB channel models adopted by the IEEE 802.15.3a task group for the evaluation of proposed physical layer system will also be introduced to facilitate the discussions about the performance of the proposed system. We will also state the evaluation criteria used by IEEE 802.15.3a task group for system performance studies which is adopted for the same purpose in this thesis.

2.1 MB-OFDM UWB System

In the proposal [4], the multi-bands orthogonal frequency division multiplexing (MB-OFDM) system described can operate in 2 different modes depending on the number of sub-bands that is activated. In this thesis, our discussions will be based on mode 1 transmission where only 3 frequency sub-bands is used for communications. However, due to the characteristic of the multi-bands system, the results attained and conclusions made can be easily interpolated for the case of mode 2 transmission. The proposed MB-OFDM UWB system partition the available UWB bandwidth of 7.4 GHz into smaller frequency sub-bands each of 528 MHz. The different sub-bands are shown with their corresponding band numberings in Table 2.1 for the ease of reference. In mode 1 transmission, only band 1 to band 3 are used.

Table 2.1: Sub-bands Allocation for MB-OFDM UWB System.

Band Number	Lower Frequency	Centre Frequency	Upper Frequency
1	3168 MHz	3432 MHz	3696 MHz
2	3696 MHz	3960 MHz	4224 MHz
3	4224 MHz	4488 MHz	4752 MHz
4	4752 MHz	5016 MHz	5280 MHz
5	5280 MHz	5544 MHz	5808 MHz
6	5808 MHz	6072 MHz	6336 MHz
7	6336 MHz	6600 MHz	6864 MHz
8	6864 MHz	7128 MHz	7392 MHz
9	7392 MHz	7656 MHz	7920 MHz
10	7920 MHz	8184 MHz	8448 MHz
11	8448 MHz	8712 MHz	8976 MHz
12	8976 MHz	9240 MHz	9504 MHz
13	9504 MHz	9768 MHz	10032 MHz
14	10032 MHz	10296 MHz	10560 MHz

During any transmission instances, only one of the sub-bands will be used by each transceiver pair. The sub-band used for transmission of a particular packet of data will be changing throughout the transmission duration according to a set of defined time-frequency codes (TFC). These codes, which governs the sub-bands hopping sequence, is shown in Table 2.2. The transmission of OFDM symbols using the particular time-frequency code TFC#1 is illustrated in Figure 2.1.

Table 2.2: Time-Frequency Codes (TFC) for Mode 1 Transmission.

TFC Number	Length 6 Time Frequency Codes					
1	1	2	3	1	2	3
2	1	3	2	1	3	2
3	1	1	2	2	3	3
4	1	1	3	3	2	2
5	1	1	1	1	1	1
6	2	2	2	2	2	2
7	3	3	3	3	3	3

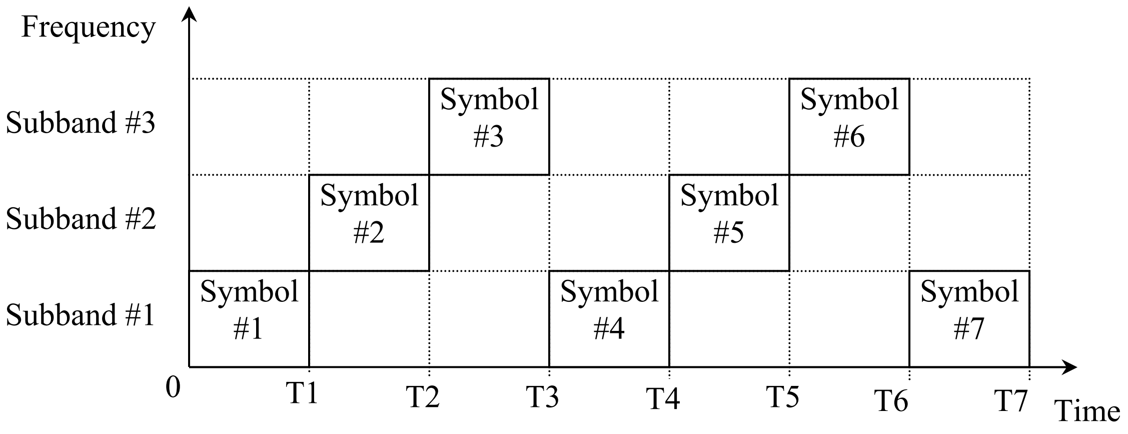

Figure 2.1: Transmission of OFDM Symbols using TFC#1.

The OFDM modulation will be carried out using 128-points Fast Fourier Transform (FFT) giving a sub-carrier frequency spacing of 4.125 MHz. Of the 128 sub-carriers, 100 sub-carriers will be used for data transmission, while 12 sub-carriers will be reserved as pilots and another 10 sub-carriers are designated as guard sub-carriers. The remaining 8 sub-carriers including the d.c. sub-carrier are set to null. By setting the d.c. sub-carrier to null, difficulties in digital-analog converter (DAC) and analog-digital converter (ADC) offsets as well as carrier feed-through in the RF system can be avoided. The OFDM symbol is formed by pre-appending the zero prefix consisting of 32 zero samples to the 128 output samples from the FFT and appending 5 zero samples to the end of the output samples from the FFT. These 5 zero samples represent the guard interval during which the system switch between different carrier frequencies for band-hopping. Therefore the total symbol time duration for one OFDM symbol is 312.5 ns.

For data packets transmission, the transmitter would first transmitted 30 consecutive OFDM symbols consisting of known preambles for the purpose of synchronization and channel estimation. The structure of the preambles as well as the training sequences, which are associated to the different time frequency codes used, that form the preambles are given in Appendix A. Without the loss of generality, we restrict the discussion of the preambles to those designed for TFC#1 here. The preambles for TFC#1 include a packet synchronization sequence portion (21 OFDM symbols), a frame synchronization sequence portion (3 OFDM symbols) and a channel estimation sequence portion (6 OFDM symbols). The packet synchronization sequence can be used for packet detection and acquisition, coarse carrier frequency estimation and coarse symbol timing. The frame synchronization sequence can be used for receiver algorithm synchronization while the channel estimation sequence can be used for channel estimation of the frequency response as well as fine carrier frequency estimation and fine symbol timing [4]. The use of the preambles will be covered in more details in later chapters when we discuss about the estimation methods used.

Following the preambles, the packet header will be transmitted at a fixed data rate of 53.3 Mbps before the frame payload is transmitted at various data rates. The packet header contains data that the receiver needed for decoding the frame payload like the data rate, the length of the data and the scrambler initialization seed, which will be described in more details later on in the section when we discuss the scrambler. The packet header will also include a portion designated as the MAC header which contains the information for medium access control (MAC) layer.

The frame payload can be transmitted in various data rates which will determine the different modulation employed for each sub-carrier, the FEC coding rate, the number of coded bits in each OFDM symbol and the time spreading factor used. The different data rates and their corresponding transmission parameters are summarized in Table 2.3.

Table 2.3: Transmission Rate and Related Parameters.

Data Rates (Mbps)	Sub-carrier Modulation	FEC Code Rate	Conjugate Symmetric Input to FFT	Time Spreading Factor (TSF)	Coded Bits/OFDM Symbol
53.3	QPSK	1/3	Yes	2	100
80	QPSK	1/2	Yes	2	100
106.7	QPSK	1/3	No	2	200
160	QPSK	1/2	No	2	200
200	QPSK	5/8	No	2	200
320	DCM	1/2	No	1	200
400	DCM	5/8	No	1	200
480	DCM	3/4	No	1	200

In Figure 2.2, the block diagram of the proposed transmitter system is illustrated. Data bits are first pass through a data scrambler followed by a rate-1/3 convolutional code encoder. The coded bits are then punctured (or not) according to the required coding rates. After which, the bits stream will be interleaved using a 3-stage interleaving scheme to provide protection against burst errors in the bits stream. The next stage of modulation involves the mapping of the bits stream using the Quadrature Phase Shift Keying (QPSK) constellations or using the Dual Carrier Modulation (DCM) mapping before passing the mapped complex data to the FFT to perform the OFDM modulation. Time domain spreading can then be performed if transmission data rate is less than or equal to 200 Mbps. The time domain data are then pre-appended with a string of 32 zero samples which forms the zero prefix for the OFDM symbol. The baseband OFDM data stream is then passed through the local oscillator to obtain the final transmission signals. Clipping is performed for signals exceeding a designed PAPR level to limit out of band harmonics.

The data scrambler is realized using a pseudo random binary sequence (PRBS) generator which generates the PRBS by

$$x_n = x_{n-14} \oplus x_{n-15} \tag{2.1}$$

where $\oplus$ denotes modulo-2 addition. The scrambled data bits are obtained by performing modulo-2 addition on the unscrambled data bits with the PRBS. Mathematically,

$$s_m = d_m \oplus x_m \tag{2.2}$$

where d_m and s_m represents the unscrambled bits and scrambled bits respectively.

Through the scrambling of the data bits, a specific frame which results in very large PAPR and hence subjected to large distortions due to the clipping can be resent in a different form if the distortions degrade the signal so much that it cannot be recovered at the receiver.

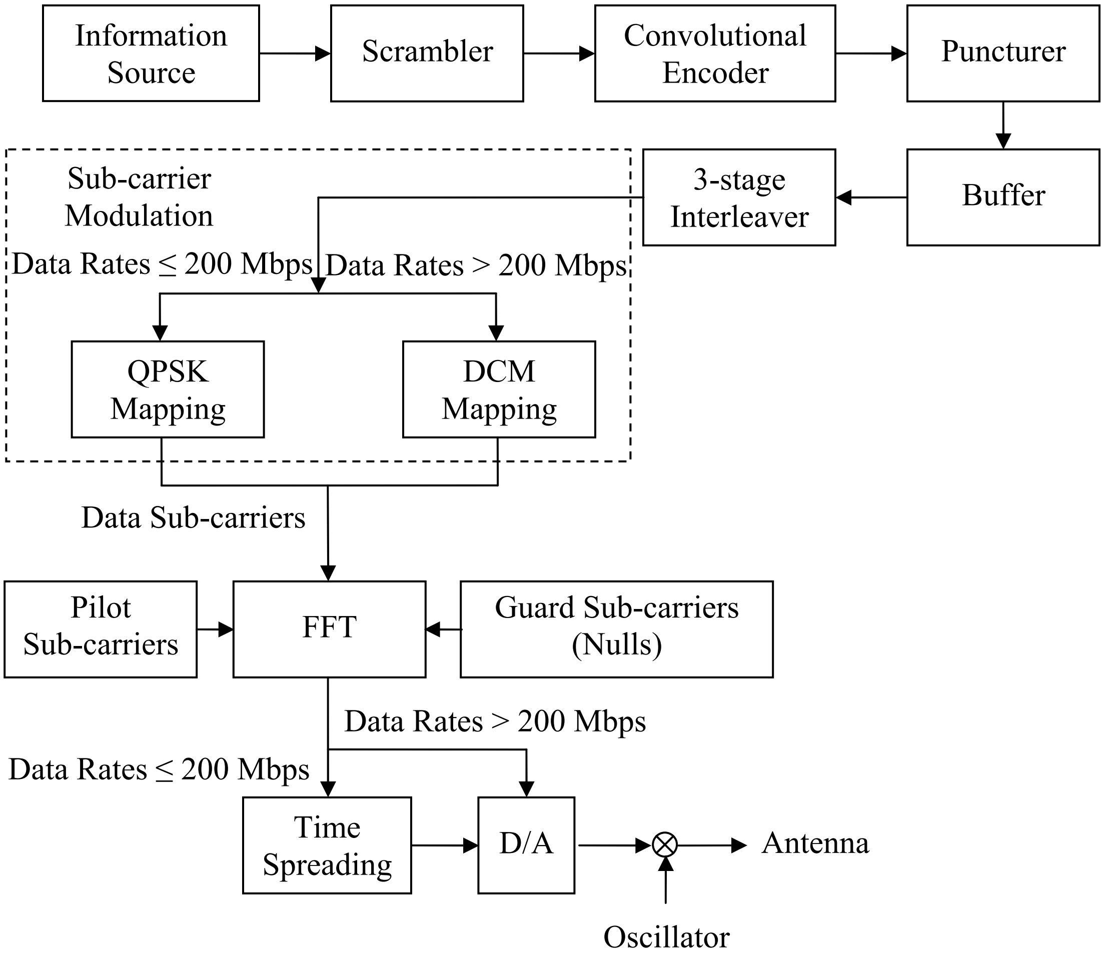

Data Rates: 53.3 Mbps, 80 Mbps, 106.7 Mbps, 160 Mbps, 200 Mbps, 320 Mbps, 400 Mbps and 480 Mbps

Figure 2.2: Block Diagram of MB-OFDM UWB Transmitter.

An initialization sequence is required for the PRBS generator which is determined by a seed identifier transmitted to the receiver through the packet header. The seed identifier value is generated using a 2-bit counter starting at the 00 state for the first transmitted frame and incremented for each frame sent. The seed identifiers and their corresponding initial sequence are given in Table 2.4.

Table 2.4: Scrambler Initialization Sequence.

Seed Identifier	Initialization Sequence
00	0011 1111 1111 1111
01	0111 1111 1111 1111
10	1011 1111 1111 1111
11	1111 1111 1111 1111

The rate-1/3 convolutional encoder used in the proposed system is the industry-standard encoder with generator polynomial, $g_0 = 133_8$, $g_1 = 165_8$ and $g_2 = 171_8$. A tail bits stream of 6 zeros are appended to the end of the frame data bits to return the encoder to the "zero state" in order to lower the error probability of the decoder. The coded bits stream is punctured by omitting some of the encoded bits in the transmitter which will reduce the number of transmitted bits and increase the code rate. At the receiver, dummy zero metric is inserted into the decoder in place of the omitted bits. If the first, second and third bit generated by the encoder is denoted as "A", "B" and "C" respectively, the puncturing patterns used to create the code rate of 1/2, 5/8 and 3/4 can be illustrated as in Figure 2.3.

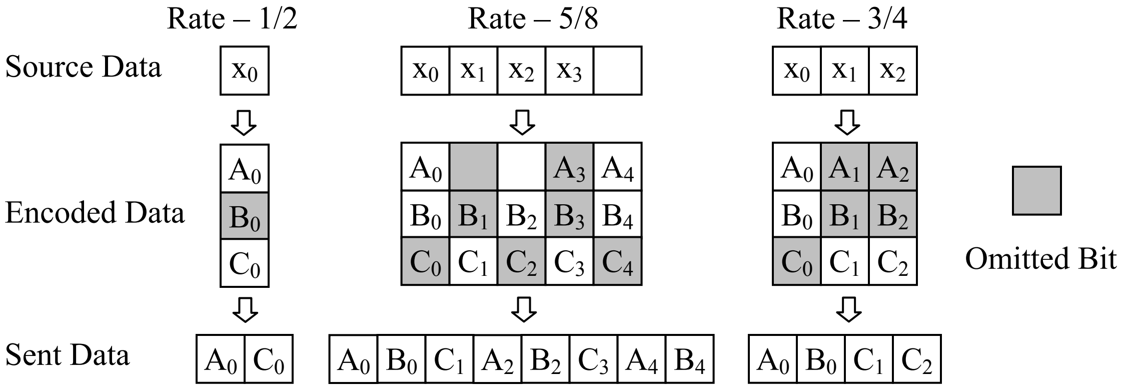

Figure 2.3: Puncturing Patterns.

The 3-stage interleaving scheme used to protect the bits stream from burst errors varies according to the transmission data rates. The punctured bits are buffered to form groups of either 100 or 200 depending on the transmission rates as indicated in Table 2.3. Each of these groups contains the number of bits to be transmitted in an OFDM symbol denoted as N_{CBPS}. The bits stream is partition in groups of 3(3-TSF)N_{CBPS} bits for interleaving with pad bits added if there is not enough information data bits. The order of the bits is then changed by passing the bits through 3 different stages of interleaving consecutively. For the first stage of the interleaving scheme, each group of 3(3-TSF)N_{CBPS} bits are interleaved using a block symbol interleaver. If the input sequence and output sequence of the interleaver is denoted as U(i) and S(i) respectively, i = 0, 1, 2, … 3(3-TSF)N_{CBPS} – 1, the input-output relationship of the interleaver is given by

$$S(i) = U\left(floor\left(\frac{i}{N_{CBPS}} \right) + 3(3 - TSF) \times (i \bmod N_{CBPS}) \right) \tag{2.3}$$

The second stage of the interleaving scheme is a tone interleaver where the order of the bits within a single OFDM symbol is permuted using a block interleaver. If the input sequence and output sequence of the interleaver is denoted as S(i) and T(i) respectively, i = 0, 1, 2, … $N_{CBPS} - 1$, the input-output relationship of the interleaver is given by

$$T(i) = S\left(floor\left(\frac{i}{N_{T\text{int}}} \right) + 10 \times \left(i \bmod N_{T\text{int}} \right) \right) \tag{2.4}$$

where $N_{Tint} = N_{CBPS}/10$. The last stage of the interleaving scheme consists of a cyclic shift of each block of N_{CBPS} bits within the span of the first stage of interleaving. Mathematically, if the input sequence and output sequence of the interleaver is denoted as T(b,i) and V(b,i) respectively, b = 0,1, …, 3(3-TSF) – 1 and i = 0, 1, 2, … $N_{CBPS} - 1$, the input-output relationship of the interleaver is given by

$$V(b,i) = T\left(b, \left(i + \frac{33\left(TSF \times N_{CBPS}\right)}{200} \right) \bmod N_{CBPS} \right) \tag{2.5}$$

For transmission rate less than or equal to 200 Mbps, the interleaved bits are grouped into pairs denoted as $\{b_0, b_1\}$ and mapped to the corresponding complex QPSK constellation points using Table 2.5.

Table 2.5: QPSK Encoding Table.

Input bits $\{b_0 b_1\}$	QPSK Constellation Point
00	$(-1 - j)/\sqrt{2}$
01	$(-1 + j)/\sqrt{2}$
10	$(1 - j)/\sqrt{2}$
11	$(1 + j)/\sqrt{2}$

For transmission rate greater than 200 Mbps, the sub-carriers are modulated using dual-carrier modulation (DCM) which is a form of direct spreading code division multiple access (DS-CDMA) technique applied in the frequency domain. Each group of 200 bits, b_i, i = 0, 1, …, 199, will be mapped to 100 complex symbols, y_n, n = 0, 1, …, 99, to be transmitted in a single OFDM symbol. The bits are first converted into complex symbols x_k, k = 0, 1, …, 99, by Equation 2.6 and x_k are then converted to y_n by Equation 2.7.

$$\begin{bmatrix} x_0 \\ x_1 \\ x_2 \\ \vdots \\ x_{50} \\ x_{51} \\ x_{52} \\ \vdots \\ x_{98} \\ x_{99} \end{bmatrix} = \begin{bmatrix} 2b_0 - 1 \\ 2b_1 - 1 \\ 2b_3 - 1 \\ \vdots \\ 2b_{100} - 1 \\ 2b_{101} - 1 \\ 2b_{102} - 1 \\ \vdots \\ 2b_{148} - 1 \\ 2b_{149} - 1 \end{bmatrix} + j \begin{bmatrix} 2b_{50} - 1 \\ 2b_{51} - 1 \\ 2b_{53} - 1 \\ \vdots \\ 2b_{150} - 1 \\ 2b_{151} - 1 \\ 2b_{152} - 1 \\ \vdots \\ 2b_{198} - 1 \\ 2b_{199} - 1 \end{bmatrix} \tag{2.6}$$

$$\begin{bmatrix} y_m \\ y_{m+50} \end{bmatrix} = \frac{1}{\sqrt{10}} \begin{bmatrix} 2 & 1 \\ 1 & -2 \end{bmatrix} \begin{bmatrix} x_{2m} \\ x_{2m+1} \end{bmatrix}, \qquad \mathrm{m} = 0, 1, \ldots, 49 \tag{2.7}$$

The complex symbols formed by either QPSK mapping or DCM mapping are passed to the FFT together with defined pilots for OFDM modulation. If the complex symbol stream is denoted as d_i, then the complex numbers $c_{n,k}$ which corresponds to the sub-carrier n of the k^th OFDM symbol for k = 0, 1, …, $N_{SYM} - 1$, where N_{SYM} is the total number of OFDM symbols in a frame, can be written as

$$\begin{aligned} c_{n,k} &= d_{n+50\times k} \\ c_{n+50,k} &= d^{*}_{(49-n)+50\times k} \end{aligned} \tag{2.8}$$

for information data rates less than or equal to 80 Mbps and

$$c_{n,k} = d_{n+100\times k} \tag{2.9}$$

for information data rates more than or equal to 106.7 Mbps. In other words, for the lower data rates, the data input to the FFT form pairs of complex conjugates. Allocation of the complex numbers $c_{n,k}$ to the sub-carrier frequencies is shown in Table 2.6.

Table 2.6: Allocation of Sub-carriers Frequency.

Sub-carrier Frequency	Input Complex Symbol
-64 to -62, 0, 62 to 63	Null
-61 to -57, 57 to 61	Guard sub-carriers
-55, -45, -35, -25, -15, -5, 5, 15, 25, 35, 45, 55	Pilot sub-carriers
-56	$c_{0,k}$
-54 to -46	$c_{1,k}$ to $c_{9,k}$
-44 to -36	$c_{10,k}$ to $c_{18,k}$
-34 to -26	$c_{19,k}$ to $c_{27,k}$
-24 to -16	$c_{28,k}$ to $c_{36,k}$
-14 to -6	$c_{37,k}$ to $c_{45,k}$
-4 to -1	$c_{46,k}$ to $c_{49,k}$
1 to 4	$c_{50,k}$ to $c_{53,k}$
6 to 14	$c_{54,k}$ to $c_{62,k}$
16 to 24	$c_{63,k}$ to $c_{71,k}$
26 to 34	$c_{72,k}$ to $c_{80,k}$
36 to 44	$c_{81,k}$ to $c_{89,k}$
46 to 54	$c_{90,k}$ to $c_{98,k}$
56	$c_{99,k}$

The 12 pilot sub-carriers are used to make the coherent detection of the sub-carriers information robust against frequency offsets and phase noise. They are defined using a set of complex symbols $\{P_{n,k}\}$ and a pseudo-random linear feedback shift register (LFSR) sequence ρ_l. The set of complex symbol is defined by

$$P_{n,k} = \rho_{k \bmod 127} \times \begin{cases} \dfrac{1+j}{\sqrt{2}}, & \mathrm{n} = 25, 55 \\ \dfrac{-1-j}{\sqrt{2}}, & \mathrm{n} = 5, 15, 35, 45 \end{cases} . \tag{2.10}$$

$$P_{n,k} = P^{*}_{-n,k}, \quad \mathrm{n} = -5, -15, -25, -35, -45, 55 \tag{2.11}$$

for data rates less than 106.7 Mbps and

$$P_{n,k} = P_{-n,k}, \quad \mathrm{n} = -5, -15, -25, -35, -45, 55 \tag{2.12}$$

for data rates more than and equal to 106.7 Mbps and

$$P_{n,k} = 0, \quad \mathrm{n} = \text{anywhere else} . \tag{2.13}$$

where

$\rho_{0\ldots126}$ = {1, 1, 1, 1, -1, -1, -1, 1, -1, -1, -1, -1, 1, 1, -1, 1, -1, -1, 1, 1, -1, 1, 1, -1, 1, 1, 1, 1, 1, 1, -1, 1, 1, 1, -1, 1, 1, -1, -1, 1, 1, 1, -1, 1, -1, -1, -1, 1, -1, 1, -1, -1, 1, -1, -1, 1, 1, 1, 1, 1, -1, -1, 1, 1, -1, -1, 1, -1, 1, -1, 1, 1, -1, -1, -1, 1, 1, -1, -1, -1, -1, 1, -1, -1, 1, -1, 1, 1, 1, 1, -1, 1, -1, 1, -1, 1, -1, -1, -1, -1, -1, 1, -1, 1, 1, -1, 1, -1, 1, 1, 1, -1, -1, 1, -1, -1, -1, 1, 1, 1, -1, -1, -1, -1, -1, -1, -1}.

The guard sub-carriers are created by copying the five outermost data sub-carriers in an OFDM symbol. The allocation of the guard sub-carriers is given in Table 2.7.

Table 2.7: Allocation of Guard Sub-carriers Frequency.

Guard Sub-carrier Frequency	Input Complex Symbol
-61	$c_{0,k}$
-60 to -57	$c_{1,k}$ to $c_{4,k}$
57 to 60	$c_{95,k}$ to $c_{98,k}$
61	$c_{99,k}$

Time-domain spreading is employed for data rates lower than 320 Mbps to improve frequency diversity through repeating the transmission of the same information using 2 OFDM symbols. If the kth original time domain OFDM symbol generated normally is denoted as $S_k(n)$ and the repeated version of the symbol is denoted as $T_k(n)$, then $T_k(n)$ can be generated as

$$T_{k'}(n) = \begin{cases} \{\mathrm{Im}[S_k(n)] + j\,\mathrm{Re}[S_k(n)]\}\rho_{(k+6)\bmod 127} & \text{no conjugate symmetry} \\ S_k(n)\rho_{(k+6)\bmod 127} & \text{with conjugate symmetry} \end{cases} \tag{2.14}$$

2.2 Channel Models

To evaluate the performance of the proposed MB-OFDM UWB system, an UWB channel model is defined by IEEE P802.15 working group 3a for wireless personal area networks [10]. The channel model is actually a statistical model based on channel measurements taken. The frequency selective multi-path fading channel model is derived from the Saleh-Valenuela model [11] with a couple of slight modifications. The channel model distinguishes between cluster arrival rates and ray arrival rates as in the approach in [11].

Another important characteristic of the model is that the multi-path gain amplitudes are based on lognormal distribution rather than commonly assumed Rayleigh distribution. Also, the independent fading is assumed for each cluster as well as each ray within the cluster.

Four different channel environments model (CM 1-4) were defined. CM1 describes the transmission scenario where the transmitter and receiver are less than 4m apart and there is line-of-sight (LOS) between the two antennas. CM2 describes the scenario with the same transmission range as CM1 but for the case of non-LOS (NLOS) between the antennas. CM3 describes non-LOS transmission for the range of between 4m to 10m. Lastly, CM4 modeled the scenario of transmission in an environment with strong delay dispersion with a delay spread of 25ns. For each different channel model, key parameters like mean excess delay, root-mean-squared (RMS) delay spread and power decay profile are used to derive the model parameters. Based on these parameters, 100 actual realizations for each channel model are derived which are provided by the IEEE P802.15 working group 3a.

The output of the provided channel model is a continuous time arrival and amplitude value which spans the entire UWB frequency band. A consistent methodology is described by the authors in [10] to discretize the model for different sample times without losing the essence of the multi-path model. The discrete channel model described by the discrete channel impulse response is further filtered and down-converted using bandpass filtering and down-conversion to obtain the baseband channel impulse response for the different sub-bands. Mathematically, the discrete channel impulse response of the channel model can be written as

$$h_{n,m}(t) = \sum_{p=0}^{P} h_{n.m}(p)\delta(t\text{-}pT_s) \tag{2.15}$$

where $h_{n,m}(p)$ is the complex multi-path gain coefficient, m is the frequency sub-bands index, n is the channel realization index, T_s is the sampling time duration.

To evaluate the performance of the MB-OFDM UWB system in the UWB channel models, the transmission of 200 packets each containing 1024 bytes of information data in each realization of the channel models are simulated. At the receiver, the packet-error-rate (PER) performance is calculated and the worst performing 10% of the channel realizations are removed. The PER as well as the bit-error-rate (BER) performance of the system is then recalculated using the data from the remaining channel realizations.

2.3 Conclusions

In this chapter, the proposed MB-OFDM UWB system in [4] as well as the UWB channel model used to evaluate the system performance is described in details. This chapter provides the background upon which the discussions in the rest of the thesis are built on.

Chapter 3

Simplified LDPC Code for MB-OFDM UWB System

Forward error-correcting (FEC) codes are very important in determining the performance of MB-OFDM UWB system. Hence, it is essential to employ a powerful error correcting code for MB-OFDM UWB system especially for the higher data rates mode due to the necessity of high code-rate. Due to implementation limitation, convolutional code is currently considered as the error-correcting code for MB-OFDM UWB system [4]. However, convolutional code have limited error-correcting performances compared to more advance error-correcting codes like Turbo codes and Low-Density Parity-Check (LDPC) codes. Turbo codes are very powerful codes with performance approaching the Shannon limits. However, the computational complexities required for a Turbo code decoder creates a significant challenge for high-speed implementation required for high-rate UWB system. LDPC codes, on the other hand, have superior performance to convolutional codes and slightly worse performance than Turbo codes. However, a LDPC code iterative decoder can be implemented using parallel architecture and hence are more suitable for high-speed implementation. In this chapter, the use of LDPC codes as the FEC in the MB-OFDM UWB system is examined. The simulation results shows that using a simplified LDPC code, the performance of the MB-OFDM UWB system is greatly improved. Moreover, the simplified LDPC code has great potential in terms of ease of implementation.

3.1 Simplified LDPC Codes

Low-Density Parity-Check (LDPC) code, first invented by Gallager in 1962 [12], has been rediscovered and brought to the attention of the research community by Mackay and Neal in 1996 [13][14]. LDPC code is a powerful error correcting code that achieves performance close to Shannon limit. The minimum distance of an LDPC code increases proportionally to the code length with a high probability. This is desirable for the high bit-rate transmission that requires very low frame error rate. LDPC can be decoded with iterative soft decision decoding algorithms called message-passing algorithms. The most powerful of these algorithms is known as “belief propagation”. The studies of LDPC for OFDM systems have been conducted in [15]. The results showed that LDPC leads to increased transmission distance, lower power requirements, and increased throughput compared to known error correcting code like convolutional code, Reed-Solomon code and turbo code.

However, in terms of implementation, both the encoding and decoding process LDPC codes are significantly more complex in terms of hardware complexity especially for LDPC codes constructed using semi-random methodology, which is unbearable for high-data rate applications. In this chapter, the design and evaluation of the system performance of a MB-OFDM UWB system using a class of (3, k)-regular LDPC code designed using a joint code and decoder design approach is detailed. The performance of the simplified LDPC code is nearly identical to the normal semi-random LDPC codes while offering the benefits of less hardware complexity, making it the ideal solution for high data-rate application.

LDPC codes are linear block codes with sparse parity check matrix. They can be represented by bipartite graphs where one set of nodes represents the parity check equations (check nodes) and the other represents the coded data variables (variable nodes) as in Figure 3.1. The 1's in the parity-check matrix are the links between the nodes. The shortest length of cycles of any of the nodes in a particular graph is known as the girth of the graph and it has been shown [14] that maximizing the girth of the graph would improve the performance of the corresponding code.

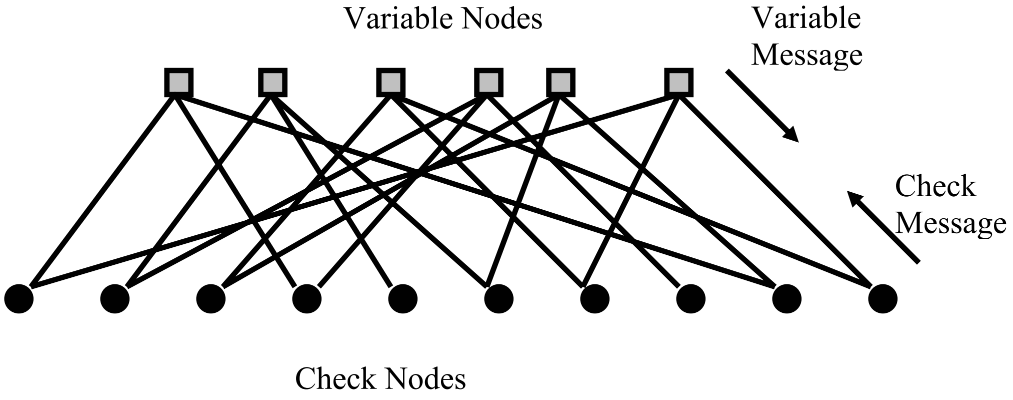

Figure 3.1: Example of a bipartite graph representation for a LDPC code.

.

There are two main groups of LDPC codes: regular and irregular. Regular LDPC codes have the same number of 1s in every column of their parity-check matrices while irregular LDPC codes have a range of values. In [16], the optimal distribution of the 1s in parity-check matrix of irregular LDPC codes is examined and the LDPC codes constructed accordingly have very good performance, surpassing even the best turbo codes. Both types of LDPC codes can be decoded effectively using a well known and simple decoding algorithm known as the sum-product algorithm (or belief propagation algorithm) introduced in [12] which is an iterative decoding algorithm. Let the parity-check matrix of the LDPC code be $\mathbf{H} = |H_{ml}|$, where m is row (i.e. check nodes) index and l is the column (i.e. bit nodes) index. If $H_{ml} = 1$, then the m^{th} check node is connected to l^{th} bit node. The algorithm starts off by assigning *a priori* log-likelihood ratios (LLRs) $L(p_l)$ to each of the bits. For binary phase shift keying (BPSK) modulation in additive white Guasssin noise (AWGN) channel, this ratio is given by

$$L(p_l) = \frac{2}{\sigma^2} c_l \tag{3.1}$$

where c represents the received information about the coded bits and σ^2 is the noise variance. If $L(q_{l\rightarrow m})$ and $L(r_{m\rightarrow l})$ represents the information flowing from bit node to check node and the information flowing from check node to bit node respectively, the decoding algorithm can be simply represented by the flowchart in Figure 3.2.

The simplified LDPC code for the MB-OFDM UWB system considered in this chapter is a regular LDPC code constructed using a partly parallel (3,k)-regular LDPC decoder architecture introduced in [17]. The codes are constructed using the highly-structured decoder architecture in a semi-random fashion. This design also allows an efficient systematic encoding that can be carried out without the use of a dense generator matrix. Instead, the encoding process makes use of sparse matrix multiplication and permutation sequences that can be performed with less computation load and greater speed. The hardware realization of a parallel decoder for an arbitrary LDPC codes is very complex even for small code length (below 10,000 bits) [17]. A fully parallel decoder may be attractive in term of high throughput but the high complexity of the hardware made it unsuitable for practical purposes [17]. Therefore, a more practical partly parallel decoder using the decoder-first design approach is considered for actual hardware implementation.

The structure of the decoder architecture is shown in Figure 3.3. The decoder consists of k^2 memory banks each with 4 random access memory (RAM) used to stored the information used in the decoding process. The i^{th} memory bank is represented as MEM BANK-(x, y), where $x = (i - 1) \bmod k + 1$ and $y = \lfloor (i-1)/k \rfloor + 1$, where $\lfloor \cdot \rfloor$ represents the floor function). Each RAM in the memory banks can store L information (i.e. L addresses) corresponding to a group of L variable nodes. The first RAM, RAM 1, is used to store the variable node information and the other three RAM, E1 - E3, are used to store the check node information. The RAMs are addressed using an Address Generator (AG) associated with the MEM BANK. The address generator is a simple modulo L binary counter that can be preset with any initial start value. Permutation within the L variable nodes is achieved by varying the initial value of each AG. The variable node processor units (VNU) and the check node processor unit (CNU) is used to calculate the information associated to the variable nodes and check nodes respectively. The shuffle network is used to shuffle the connections between the MEM BANKs and the CNUs to enable different permutations.

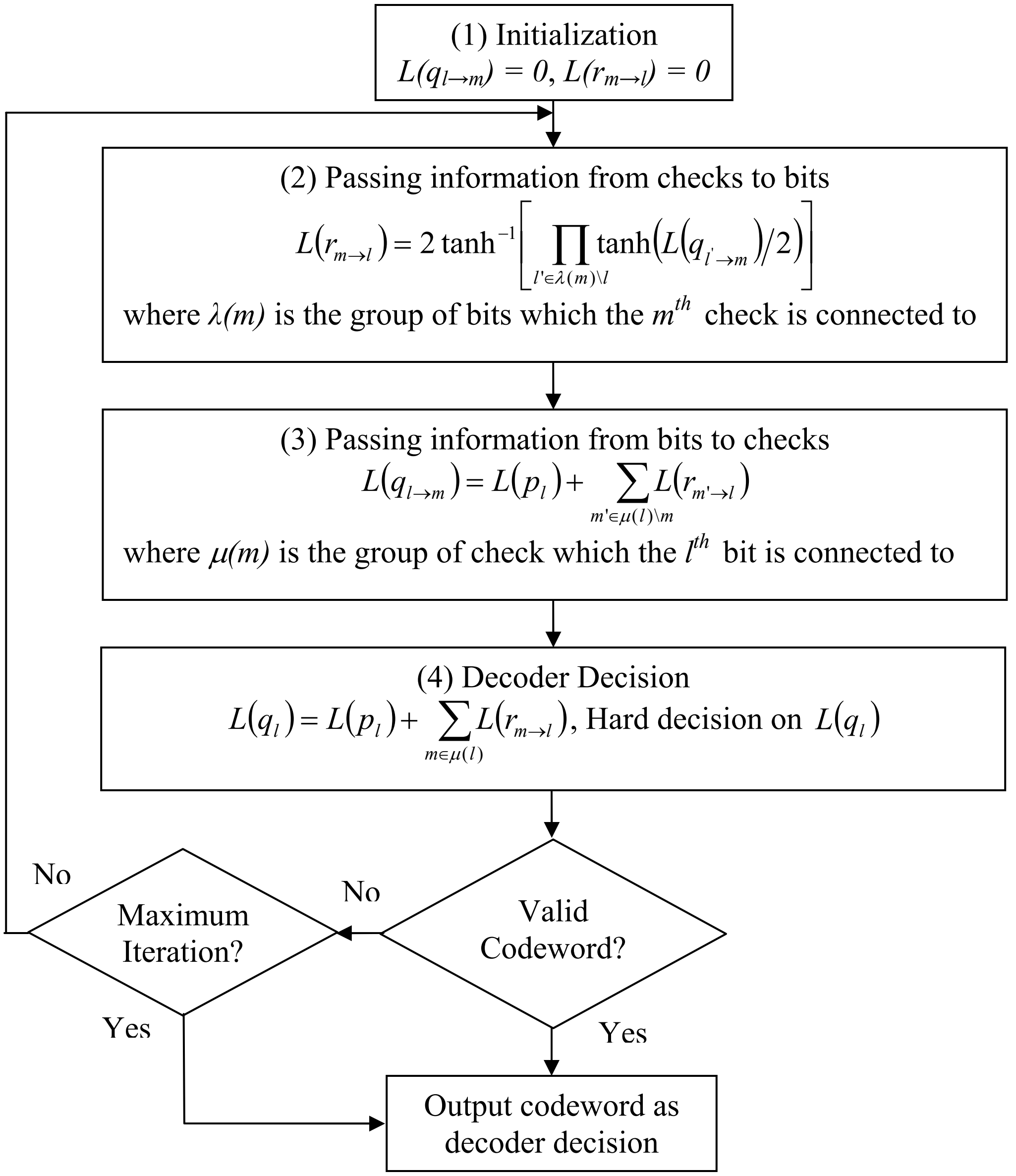

Figure 3.2: Flowchart of Sum-Product Decoding Algorithm.

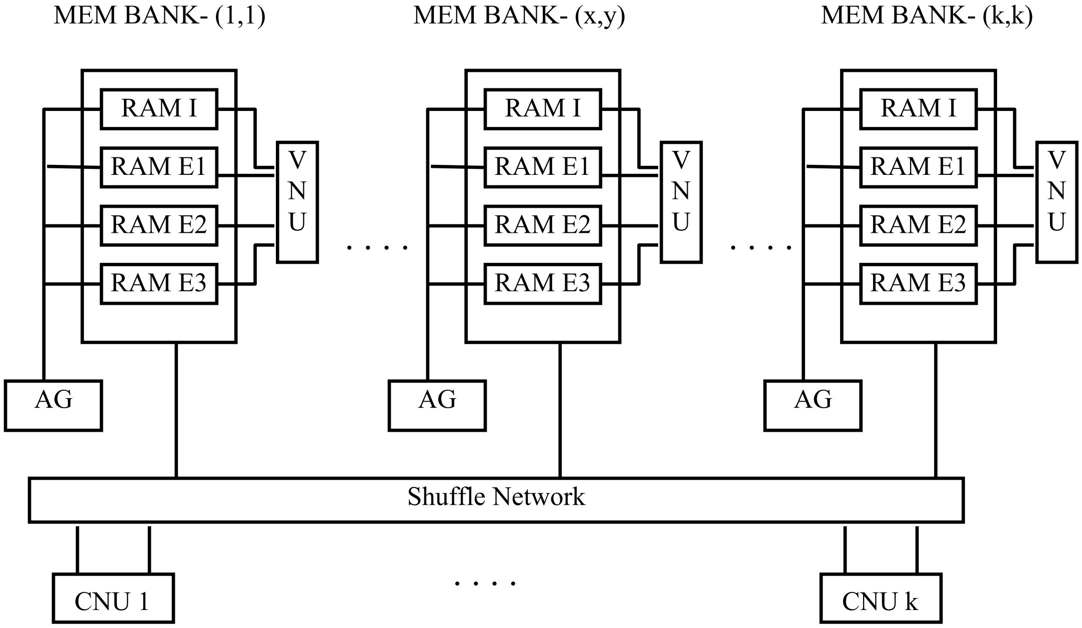

Figure 3.3: A simplified partly parallel (3,k)-regular LDPC decoder architecture.

By controlling the shuffling algorithm of the shuffling network, an ensemble of highly-structured parity-check matrices can be defined. Each of these codes has a parity-check matrix, $\mathbf{H} = \left[\mathbf{H}_0^T, \mathbf{H}_1^T, \mathbf{H}_2^T\right]^T$, where $\mathbf{H}_0$ and $\mathbf{H}_1$ is deterministic and $\mathbf{H}_2$ is semi-random. The structure of the deterministic sub-matrices $\mathbf{H}_0$ and $\mathbf{H}_1$ are shown in Figure 3.4. The column length and row length of the sub-matrices are Lk and $L{\cdot}k^2$ respectively. Each block matrix $\mathbf{I}_{x,y}$ in $\mathbf{H}_0$ represents an LxL identity matrix while each block matrix $\mathbf{P}_{x,y}$ in $\mathbf{H}_1$ represents an LxL identity matrix cyclically shifted to the right by $((x-1).y)\bmod L$. The third sub-matrix $\mathbf{H}_2$ is constructed using the decoder architecture and a Random Permutation Generator (RPG) described in [17] and can be represented as a Lk x $L{\cdot}k^2$ matrix with the properties listed below.

- The entries in $\mathbf{H}_2$ are all zeros except for k^2 block matrices of dimension LxL denoted as $\mathbf{T}_{x,y}$.
- $\mathbf{T}_{x,y}$ is a identity matrix cyclically shifted to the right by $t_{x,y}$ such that:
  - For same x, $t_{x,y_1} \neq t_{x,y_2}, \forall y_1, y_2 \in \{1,\ldots,k\}$.
  - For same y, $t_{x_1,y} - t_{x_2,y} \neq ((x_1 - x_2)y) \bmod L, \forall x_1, x_2 \in \{1,\ldots,k\}$.
- $\mathbf{T}_{x,y}$ are randomly distributed in $\mathbf{H}_2$ with the constraints that there are k blocks of $\mathbf{T}$ matrix for each y and only one block in every groups of L columns in $\mathbf{H}_2$.

An ensemble of codes is generated by randomly constructing $\mathbf{H}_2$ and the *girth average* [17] of their corresponding graphs is compared. The girth average of a bipartite graph G is defined as $\sum_{u \in G} g_u / N$ where g_u is the shortest cycle that passes through node u in the bipartite graph and N is the total number of nodes in G. The girth average has been shown to be an effective criterion for good LDPC codes and is used here to determine the best code from the ensemble. As a rule, the larger the girth average, the better the LDPC code. Hence, the code with the largest girth average is determined to be the best code from the ensemble. The dimensions of the codes in the ensemble are partly constrained by the code rate. The code rate of the code ensemble is lower bounded by $(1 - 3/k)$ and given an arbitrary k, any code length that could be factored as Lk^2 can be constructed provided that L cannot be factored as $L = a \cdot b$, $\forall a, b \in \{0, ..., k-1\}$.

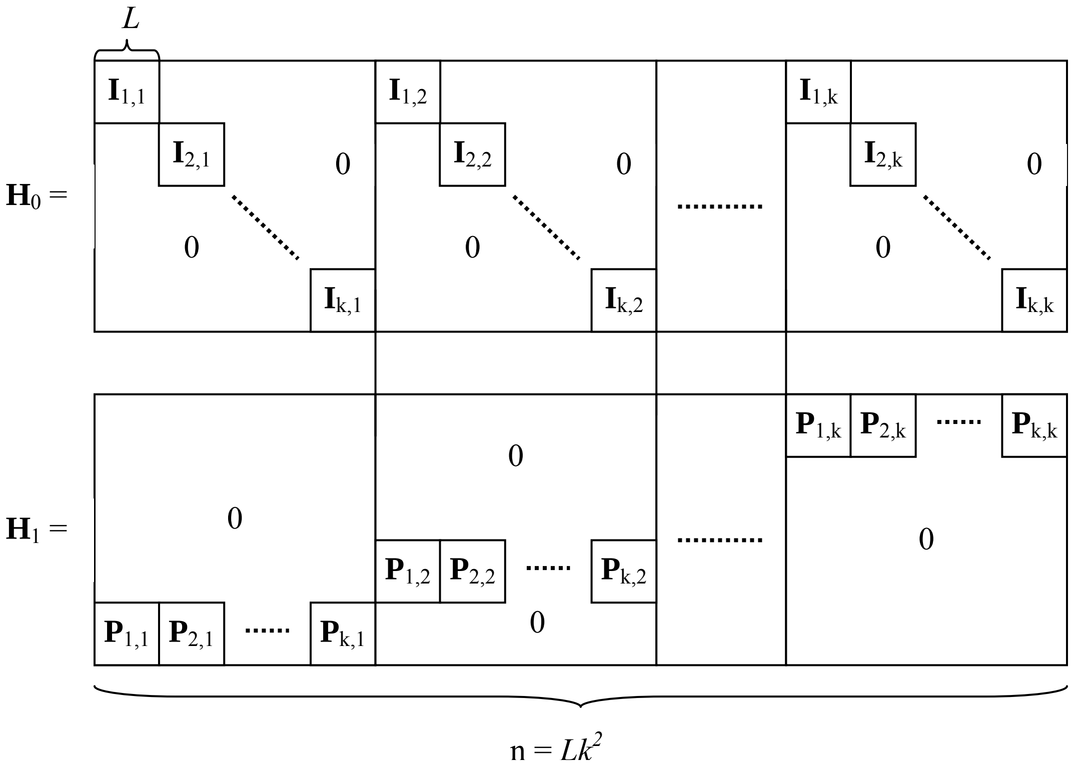

Figure 3.4: Structure of Deterministic Matrices $\mathbf{H}_0$ and $\mathbf{H}_1$.

To evaluate the performance of the simplified LDPC codes in MB-OFDM UWB system, we designed a code suitable for the system [18]. A high-rate LDPC code is designed to replace the rate-¾ convolutional code for 480Mbps transmission mode and system performance is simulated. Due to the use of symbol interleavers in the MB-OFDM UWB system, the decoding process has an unavoidable latency of 6 OFDM symbols. To ensure that the use of LDPC block code will not increase the original latency, the code length is designed to be around 1800 even though a larger code length would normally improve the performance of the LDPC code.

Since the desired code rate is ¾, the value of k is limited by the lower bound on the code rate to be larger than or equal to 12. Setting $k = 12$ will not guarantee a code rate of ¾ but will ensure that the code rate of the design code is greater than ¾. Similarly, as the code length is to be kept around 1800, L is chosen to be 13, giving the actual code length of 1872. Note that the choice of $L = 13$ will result in a code length that is nearest to 1800 given the constraint on L. Using, these parameters, an ensemble of 100 semi-randomly generated LDPC codes is created. The histogram of the ensemble with regards to their girth average is shown in Figure 3.5. The largest girth average of the ensemble is 6.333 and the parity-check matrix with that girth average is selected as the parity-check matrix of the LDPC code for the MB-OFDM UWB system. A systematic generator matrix is computed using the parity-check matrix to use at the encoder. The actual code rate of the selected simplified LDPC codes is 0.7511.

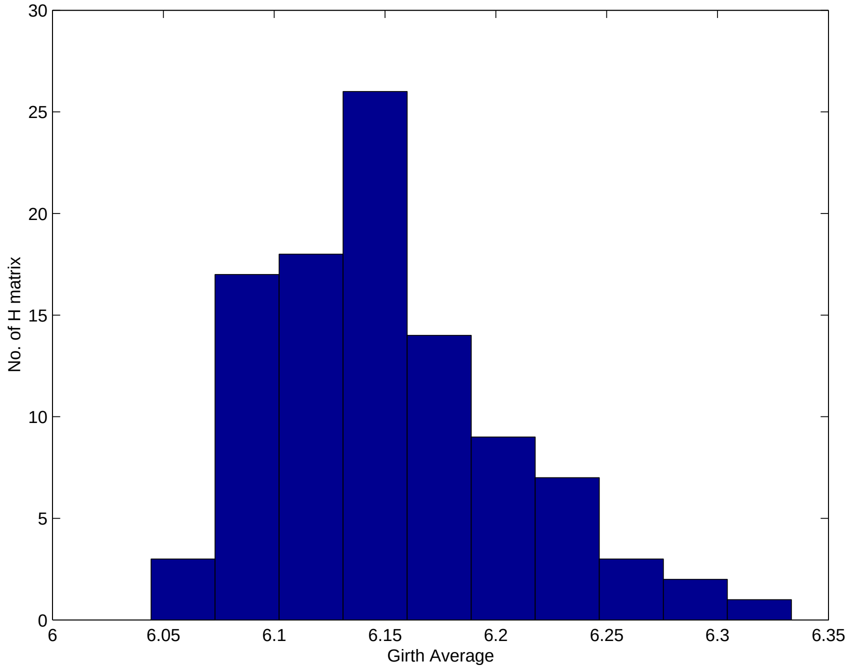

Figure 3.5: Girth Average Histogram of LDPC Codes Ensemble.

3.2 Performance Studies

A LDPC encoder and a decoder using the sum-product algorithm are incorporated into the proposed MB-OFDM UWB system replacing the convolutional encoder and Viterbi decoder in the transmitter and receiver respectively. Moreover, the 3-stage interleaving scheme is removed as LDPC codes have the ability to handle burst errors. The block diagram of the MB-OFDM UWB system using LDPC codes is shown in Figure 3.6. Note that the system uses QPSK sub-carrier modulation instead of the DCM modulation for 480Mbps transmission mode described in Chapter 2. To ensure a fair comparison of the error-correcting performance, a previous version of the proposed MB-OFDM UWB system which uses convolutional codes as FEC and QPSK as sub-carrier modulation for 480Mbps transmission mode will be used for comparison.

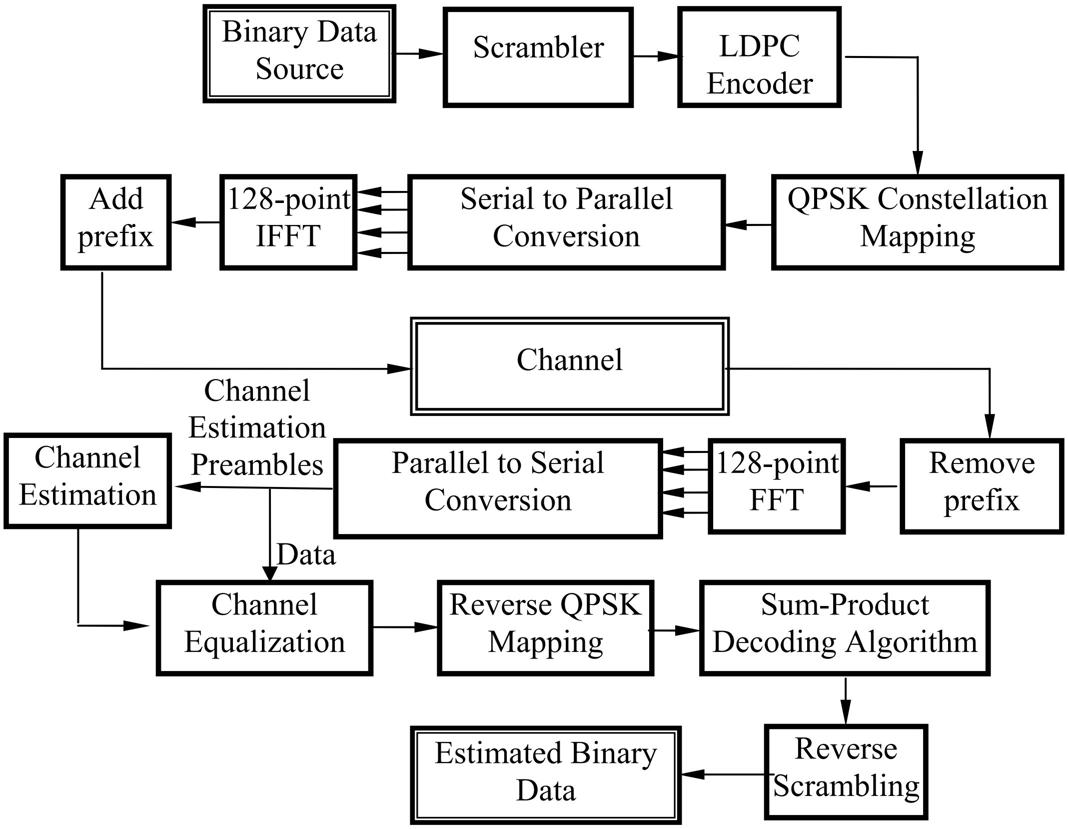

Figure 3.6: Block Diagram of MB-OFDM UWB System using LDPC Codes.

The performances of three different error-correcting codes on the MB-OFDM UWB system are investigated. The three codes are a punctured convolutional code with constraint length 7, an irregular LDPC code constructed randomly and a regular LDPC code constructed using the method discussed in Section 3.1. The code rate of the three codes is set to approximately 0.75. The code length of the irregular and regular LDPC codes is 1800 and 1872 respectively. The convolutional code is decoded using a Viterbi decoder with coding depth of 96 and the LDPC codes are decoded using the sum-product algorithm illustrated in Figure 3.2 with the maximum iterations of decoding set at 8. For the LDPC codes, since each sub-carrier experience different level of fading, the *a priori* log-likelihood ratios (LLRs) $L(p_l)$ of the bits is no longer given by Equation 3.1. Instead, the $L(p_l)$ of the bits is computed to be

$$L(p_l) = \frac{2h_l^2}{\sigma^2} s_l \tag{3.2}$$

where s represents the received in-phase or quad-phase information, h represents the sub-carrier channel strength and σ^2 is the noise variance.

The performance of the MB-OFDM UWB systems in Channel Model 1 and 3 introduced in Chapter 2 is simulated. Channel Model 1 and 3 is chosen as Channel Model 1 represents the best transmission channel with line-of-sight between the transmitter and receiver antenna while Channel Model 3 represents the worst transmission channel modeled accordingly to actual measurement with the longest delay spread statistics and hence the most frequency selective. For each of the channel models, all one hundred realizations of the channel model are used as the channel conditions the system is transmitting over. In both channel models, it is assumed that the channel conditions remain unchanged during the transmission of a single packet of data (quasi-static). The transmission of 200 packets each containing 1024 bytes of information bits in each realization of the channel models are simulated and the packet-error rate (PER) is calculated at the receiver as per detailed in Chapter 2. The salient features of the simulated system is summarized in Table 3.1.

The PER performances of the three codes in Channel Model 1 and 3 are shown in Figure 3.7 and Figure 3.8 respectively. Given the same approximate code rate, the LDPC codes perform much better than the convolutional code in both channel models. The irregular LDPC code and regular LDPC code has a coding gain of 2.23 dB and 2.01 dB respectively at PER = 0.01 in Channel Model 1. In Channel Model 3, the coding gain is 3.44 dB and 3.36 dB respectively. More significantly, the results demonstrated that the two LDPC codes have similar performances in both channel models. The difference between the SNR for a PER of 0.01 is only 0.20 dB in Channel Model 1 and 0.08 dB in Channel Model 3.

Table 3.1: Salient Features of Simulated System.

Systems	System with Convolutional Codes	System with Irregular LDPC Code	System with Regular LDPC Code
Data Rate	480 Mbps	480 Mbps	480 Mbps
FFT Size	128	128	128
Number of data sub-carriers	100	100	100
Code Rate	0.75	0.75	~0.75
Sub-carriers Modulation	QPSK	QPSK	QPSK
FEC	Convolutional Code	LDPC Code	LDPC Code
Bits Inter-leaver	Employed	Not Employed	Not Employed
Conjugate Symmetric Inputs	Not Employed	Not Employed	Not Employed
Time Spreading	Not Employed	Not Employed	Not Employed
Channel Estimation	Prefect Channel Estimates	Prefect Channel Estimates	Prefect Channel Estimates
Frequency Offset	None	None	None

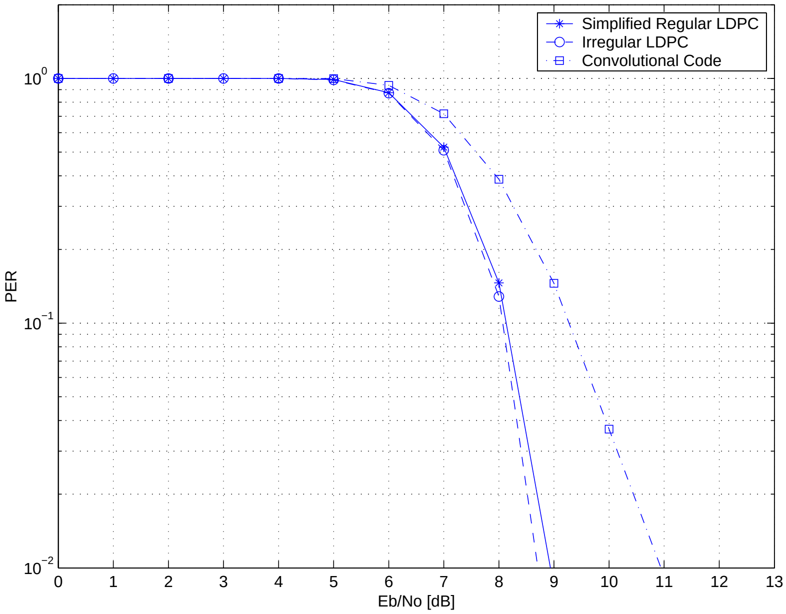

Figure 3.7: PER Performances for MB-OFDM UWB System in CM1.

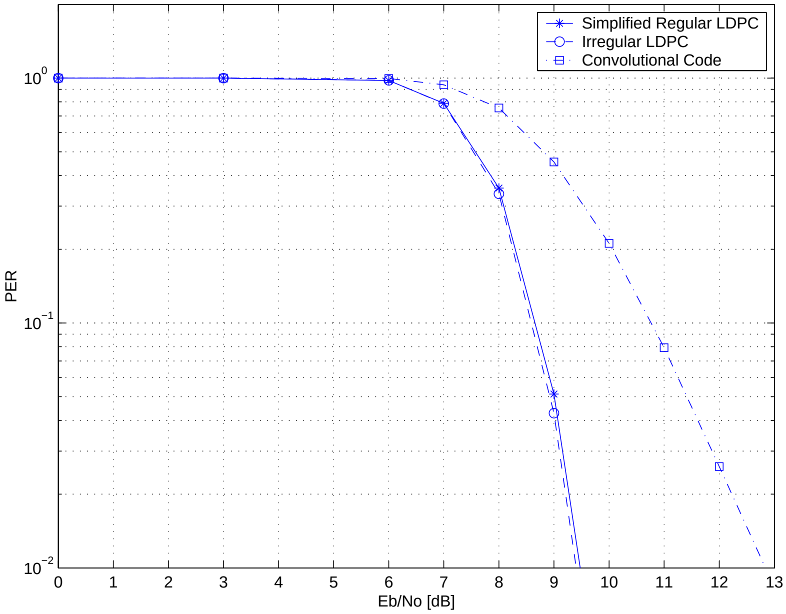

Figure 3.8: PER Performances for MB-OFDM UWB System in CM3.

However, the performance gain using LDPC comes at a price of significant computational complexity. In Table 3.2, we show the computational complexity of the encoder of convolutional codes compared to that of simplified LDPC codes in terms of number of bits addition required. The number of bits additions for convolutional codes is calculated for the equivalent number of coded bits as that of a coded block of the simplified LDPC codes.

Table 3.2: Number of bits additions for Convolutional and LDPC code Encoder.

	Convolutional Code Encoder	LDPC Code Encoder
Number of bits additions	9984	162312

In Table 3.3, the number of real multiplications and additions required for the Viterbi decoder and the LDPC decoder using sum-product algorithm is compared. Similarly, the number of operations is calculated based on the number of coded bits in one coded block of the LDPC codes. The number of operations given in the table for the LDPC decoder is 8 iterations. Even though the convolutional code decoder appears to require a lot more of additions compared to the LDPC code decoder, it does not require any multiplication while the LDPC code decoder requires a lot of multiplication operations.

Table 3.3: Number of real operations for Convolutional and LDPC code Decoder.

	Convolutional Code Decoder (Viterbi Decoder)	LDPC Code Decoder (8 Iterations)
Number of additions	106, 496	56,240
Number of multiplications	0	29,952

3.3 Conclusions

In this chapter, a joint code and decoder design approach is introduced for a simplified LDPC coded MB-OFDM UWB system in this paper to construct a class of (3, k)-regular LDPC code which exactly fit to a partly parallel decoder implementation. The code design simplifies the implementation of LDPC encoder and decoder, especially for high speed applications. The simplified LDPC coded MB-OFDM UWB achieves better performance than that of convolutional coded MB-OFDM UWB system, and is close to that of the conventional irregular LDPC coded MB-OFDM UWB system for high data rate mode. The complexity of the proposed simplified LDPC is very competitive to the convolutional code and much simpler than the irregular LDPC code. The simplified LDPC coded MB-OFDM UWB hence provides the best solution to achieve good performance for high data rate mode while keeping the hardware implementation simple.

Chapter 4

Chip Interleaved Scheme for MB-OFDM UWB System

In a MB-OFDM UWB system, each sub-carrier in the same OFDM symbol will experience different amount of fading in a frequency-selective channel. Hence, there exists inherent frequency diversity in each OFDM symbol that can be used to improve the overall system performance. One method to exploit the frequency diversity is to employ direct spreading code division multiplexing access (DS-CDMA) technique in the frequency domain. Unlike time spreading which is already incorporated in the proposed MB-OFDM system (covered in Chapter 2) for low (53.3 Mbps, 80 Mbps) to intermediate data rates (106.7 Mbps, 160 Mbps, 200 Mbps), direct spreading in the frequency domain does not need to sacrifice the data rate for diversity gain through the use of multi-codes and hence is able to maintain the high data rate (320 Mbps, 400 Mbps, 480 Mbps). However, spreading one symbol over several adjacent sub-carriers will not make effective use of the available diversity as adjacent sub-carriers are strongly correlated. Therefore, if the chips are re-ordered in such a way that the channel variation over the spreading duration of one symbol becomes less correlated, and hence more independent, then the effectiveness of the spreading would be greatly enhanced. In this chapter, we investigate the use of a direct spreading with chip interleaved scheme in MB-OFDM UWB system which, we will show through simulation, improves the system performance.

4.1 Direct Spreading with Chip Interleaving for MB-OFDM UWB System

Multi-carrier code division multiple access (MC-CDMA) based on the combination of OFDM and the conventional CDMA has received much attention [19] [20]. Combining the direct spreading CDMA technique in multi-carrier modulation enabled a system to achieve frequency diversity as CDMA signal is spread over several adjacent sub-carriers. However, by a detailed analysis of the characteristics of the frequency selective fading channel and the spread characteristics of MC-CDMA system, one would find a strong counter argument against this line of reasoning. The channel variation over the spreading duration of one symbol (a symbol is spread over several adjacent sub-carriers) is very much correlated, as the correlation between the adjacent sub-carriers is dependent on the coherent bandwidth. Therefore, such small channel variation would results in little frequency diversity gained by spreading. However, if the chips are re-ordered so that the channel variation over the spreading duration of one symbol is less correlated and more independent, then the channel variation would becomes much larger. This is equivalent to spreading a symbol across non-adjacent sub-carriers and would result in a larger frequency diversity attained.

Although, this re-ordering achieved the aim of the larger channel variation over the spreading duration, it has a negative influence on the orthogonality among the multiplexed code of MC-CDMA system. However, we can solve this problem by employing maximum likelihood detection at the receiver for coded system. In this chapter, we introduce a novel frequency domain interleaving, called chip interleaved scheme for MB-OFDM UWB system by re-ordering the chip sequence to achieve larger frequency diversity for spreading. By integrating block spread and chip interleaver structure, the interleaver structure for the proposed chip interleaved scheme is simple to implement and has less delay latency.

In [21], studies show that the chip level interleaving (CLI) scheme performs well for multi-carrier code division multiple access (MC-CDMA). By modifying a technique, which is essentially used for multi-users access, we developed a multi-code technique that can be applied to a MB-OFDM UWB system. We will show through simulation that the scheme helps to achieve a significant performance gain in such a system.

In an ordinary OFDM system, the frequency domain data from the serial-to-parallel converter output are passed directly to the input of the inverse Fast Fourier Transform (IFFT) for modulation at the transmitter. For our proposed system, before passing the data to the IFFT, a frequency domain block spreading is performed followed by a chip interleaving. For the case of MC-CDMA, the spreading and interleaving at the transmitter is carried out for a single-user as illustrated in Figure 4.1.

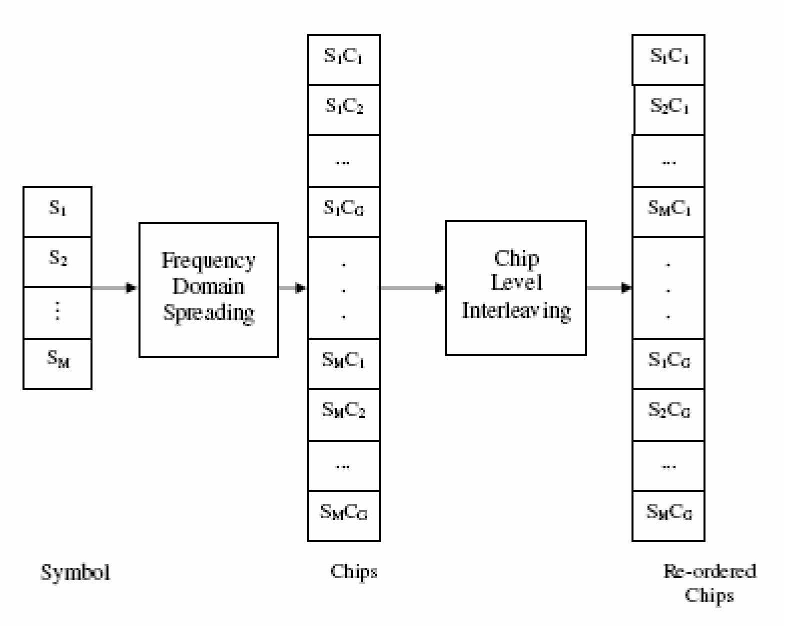

Figure 4.1: Chip Interleaving Scheme for MC-CDMA

As can be seen, the spreading is done using only one of a family of orthogonal codes. For the case of the OFDM system, the situation is slightly more complex as all the codes in the family is used. First the symbols are divided into groups consisting of a number of symbols corresponding to the number of codes in the family. For example, for Walsh-Hadamard codes with spreading factor *G*, there is altogether *G* orthogonal codes. The symbols are hence divided into groups of *G* symbols. Each symbol in the group is then spreaded using a different code in the family and chip interleaving is carried as shown in Figure 4.2 and Figure 4.3 respectively. Note that there is a reuse of code between different groups of symbol. The reuse of the codes is both convenient for implementation and practical as it eliminate the need to look for different families of orthogonal codes. The spreading of the data allows the information in different sub-carriers to be combined at the receiver instead of relying solely on the information of one sub-carrier to carry a particular data. In this way, even if the sub-carrier is lost due to deep fade, there may still be a chance that the data can be recovered by relying on the information collected from other sub-carriers. Moreover, chip interleaving is performed to fully exploit the diversity across the different sub-carriers.

The proposed chip interleaving scheme uses a very simple block interleaver for the chip level interleaving as shown in Figure 4.3. The block interleaver can be viewed as a matrix with *M* rows and *G* columns. The spreaded data can be written in row-wise and then read out column-wise. Alternatively, the block spreading and the interleaver can be combined to simplify the implementation. The *G.M* symbols can be grouped into *M* group of *G* symbols. Each group of *G* symbols can be block spread in such a way that the *G* chips for 1st symbol written in a single row and the *G* chips for the next *G*-1 symbols are added onto the same row consecutively. The process is then repeated for the remaining *M*-1 groups.

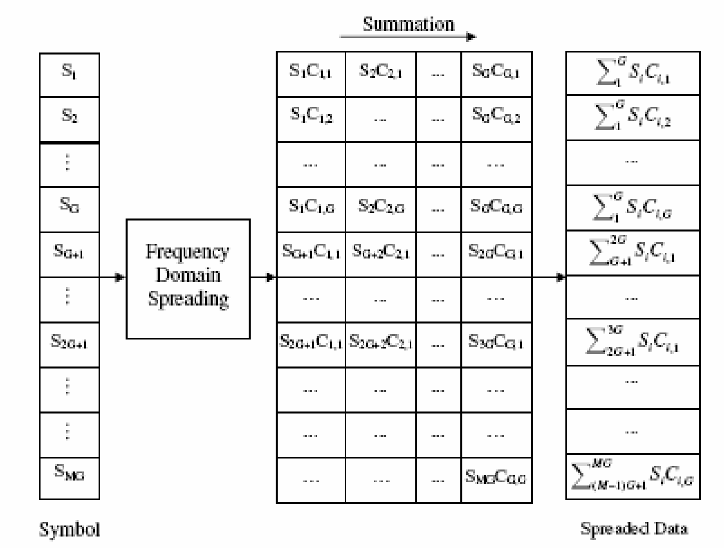

Figure 4.2: Frequency Spreading for MB-OFDM.

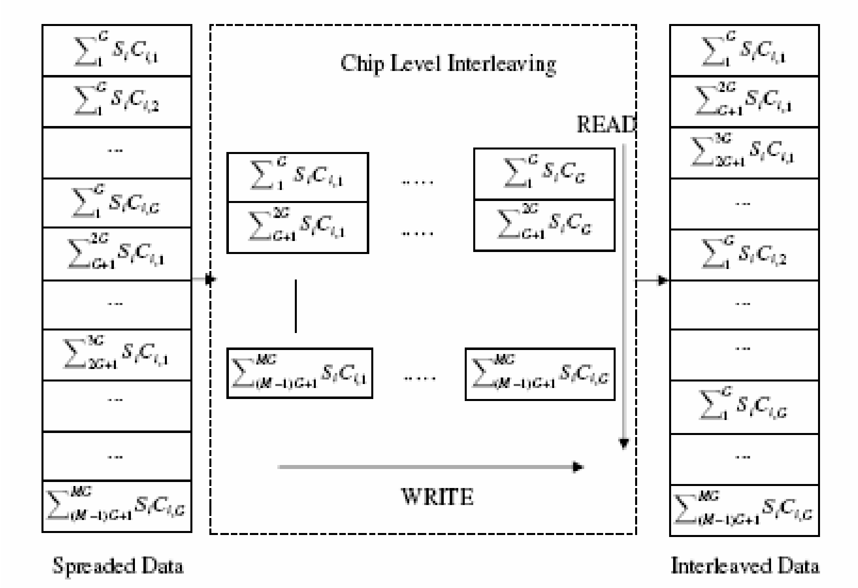

Figure 4.3: Chip Interleaving for MB-OFDM.

Since the primary advantage of spreading of data in the frequency domain is the ability of the receiver combining the information of different sub-carriers together, an effective combination strategy at the receiver is required for the system to perform well. Some common types of diversity combining techniques include maximal ratio combining (MRC), equal gain combining (EGC), orthogonal restoring combining (ORC) and minimum mean squared error combining (MMSEC) [22]. The despreading process would introduce inter-carrier interference (ICI) for MRC, EGC and MMSEC due to the loss of orthogonality of the spreading codes. On the other hand, though ORC can avoid the ICI problem, it would suffer greatly from noise enhancement if some of the sub-carriers have very low energy. However, if maximum likelihood (ML) detection [23] is applied at the receiver, the problem of ICI and noise enhancement can be reduced. While maximum likelihood detection could fully exploit the diversity provided by the direct spreading, it is computationally complex, hence making it difficult for practical implementation. Here, we consider a simplified form of the maximum likelihood detection, which is used to calculate the required log-likelihood ratios (*LLRs*) for the Viterbi decoder. Note that if we were to incorporate the LDPC coding (covered in Chapter 3) into the system, the *LLRs* calculation is the same.

We will illustrate the maximum likelihood detection used as well as the simplified form by considering a simple OFDM system with the number of data sub-carriers equal to the spreading factor used. In other words, we consider a system using Walsh-Hadamard spreading codes with G data sub-carriers where G is the spreading factor. Since each symbol is spreaded across all of the data sub-carriers, no chip interleaving is done. One can, however, easily extend the illustrated concept for the general case of a MB-OFDM system, which has a larger number of data sub-carriers than the spreading factor used and where the proposed chip interleaving is also performed.

Let the group of QPSK symbols transmitted within an OFDM symbol be denoted as X_g where g = 1, …, G and $X_g = b_{g,R} + \mathrm{j}b_{g,I}$ where $b_{g,R}$ and $b_{g,I}$ are antipodal signal corresponding to the information bits. Also let $b^{+}_{g,R/I}$ represents the event where $b_{g,R/I}$ = 1 and $b^{-}_{g,R/I}$ represents the event where $b_{g,R/I}$ = -1. The spreaded data S_i can then be written as

$$S_i = \sum_{g=1}^{G} X_g c_{g,i} \tag{4.1}$$

where $c_{d,p}$ is the p^{th} chip in the d^{th} code in the family of Walsh-Hadammard codes with spreading factor G.

At the receiver, the received frequency domain complex symbol at the output of the FFT can be written as

$$R_i = H_i \sum_{g=1}^{G} X_g c_{g,i} + N_i \tag{4.2}$$

where H_i is the complex baseband frequency response of the channel at the i^{th} sub-carrier, and N_i is a complex zero-mean Gaussian random variable with variance σ^2 representing the additive white Gaussian noise (AWGN).

The complex symbols are then pass through a single-tap linear equalizer and the equalized data are given by

$$\begin{aligned} E_i &= \frac{H_i^*}{|H_i|} R_i \\ &= |H_i| \sum_{g=1}^{G} X_g c_{g,i} + N_i^{'} \end{aligned} \tag{4.3}$$

where $N_i^{'}$ is a complex zero-mean Gaussian random variable with variance σ^2.

Let **E** represent the group of equalized data, E_i, $i = 1, \ldots, G$. If we are to apply the maximum likelihood detection principles at the output of the equalizer, we need to calculate the *LLRs* required by the Viterbi decoder (or sum-product decoder if LDPC codes is used) to determine maximum likelihood path. The *LLR* for each bit is based on the conditional probability $P\left(b_{g,R/I}^{+}\middle|\mathbf{E}\right)$ and $P\left(b_{g,R/I}^{-}\middle|\mathbf{E}\right)$ and is given by

$$\begin{aligned} L\left(b_{g,R/I}\right) &= \ln\frac{P\left(b_{g,R/I}^{+}\middle|\mathbf{E}\right)}{P\left(b_{g,R/I}^{-}\middle|\mathbf{E}\right)} \\ &= \ln\frac{P\left(\mathbf{E}\left|b_{g,R/I}^{+}\right.\right)P\left(b_{g,R}^{+}\right)}{P\left(\mathbf{E}\left|b_{g,R/I}^{-}\right.\right)P\left(b_{g,R}^{-}\right)} \qquad (4.4) \\ &= \ln\frac{P\left(\mathbf{E}\left|b_{g,R/I}^{+}\right.\right)}{P\left(\mathbf{E}\left|b_{g,R/I}^{-}\right.\right)} \end{aligned}$$

Since we are using Walsh-Hadammard codes, the real part and imagery part of E_i is independent of each other. Therefore we can simplify the computation process by considering the 2 parts separately. Let $E_{i,R}$ and $E_{i,I}$ represent the real and imagery part of E_i respectively.

With some straightforward simplifications, we can write the *LLR* for each bit as

$$L\left(b_{g,R/I}\right) = \ln\frac{\sum\limits_{\forall S_i \in D^{+}} \exp\left(-\frac{1}{\sigma^2}\left(\sum\limits_{i=1}^{G} E_{i,R/I} - \left|H_i\right| S_{i,R/I}\right)^2\right)}{\sum\limits_{\forall S_i \in D^{-}} \exp\left(-\frac{1}{\sigma^2}\left(\sum\limits_{i=1}^{G} E_{i,R/I} - \left|H_i\right| S_{i,R/I}\right)^2\right)} \qquad (4.5)$$

where D^+ and D^- refer to the set of spreaded data that corresponds to the event $b_{g,R/I}^{+}$ and $b_{g,R/I}^{-}$ respectively.

If we look at Equation (4.5) carefully, the calculations of the *LLRs* are very complicated, involving not only complex functions like the exponential and logarithm functions but also the noise variance σ^2. In a practical system, the noise variance is not easily obtained and usually required sophisticated estimation algorithm. Hence, we proposed to simplify the calculation of *LLR* by making a simple assumption and arrived at a simplified form of the maximum likelihood detection.

The assumption we make is that the noise corruption at the operating range is small enough that the conditional probability of $P(\mathbf{E}\,|\mathbf{S}_{TRUE})$, where $\mathbf{S}_{\mathrm{TRUE}}$ is the correct transmitted spreaded data, is very much larger than the other conditional probability. If we use this assumption, then instead of calculating the *LLRs* using the sum of the conditional probabilities of the sets D^+ and D^-, the *LLRs* can be calculated by using only the maximum conditional probability in each of the set.

In other words, the simplified *LLRs* are given by

$$\begin{aligned} L\left(b_{g,R/I}\right) &= \ln \frac{\max\limits_{\forall S_i \in D^+}\left[\exp\left(-\frac{1}{\sigma^2}\left(\sum_{i=1}^{G} E_{i,R/I} - |H_i| S_{i,R/I}\right)^2\right)\right]}{\max\limits_{\forall S_i \in D^-}\left[\exp\left(-\frac{1}{\sigma^2}\left(\sum_{i=1}^{G} E_{i,R/I} - |H_i| S_{i,R/I}\right)^2\right)\right]} \\ &= \min_{\forall S_i \in D^-}\left[\left(\sum_{i=1}^{G} E_{i,R/I} - |H_i| S_{i,R/I}\right)^2\right] - \min_{\forall S_i \in D^+}\left[\left(\sum_{i=1}^{G} E_{i,R/I} - |H_i| S_{i,R/I}\right)^2\right] \end{aligned} \tag{4.6}$$

From Equation (4.6), we can see that the *LLRs* calculation is greatly simplified using the assumption made. In the later section, we will prove through simulation that the simplified form does not incur any significant performance degradation.

4.2 Performance Studies

The direct spreading with chip interleaving scheme is incorporated into a MB-OFDM UWB system that is similar to the proposed MB-OFDM UWB system. The only difference between the 2 systems is that for the 480 Mbps transmission, QPSK modulation is used in this chapter instead of DCM modulation mentioned in Chapter 2. This is to provide for a clear insight into the effect of the proposed scheme on the MB-OFDM UWB system.

At the transmitter side, our proposed MB-OFDM UWB system with direct spreading and chip interleaving differs from the system described in Chapter 2 in that the complex QPSK data, S_i, $i = 1, 2, ..., M.G$, after passing through a serial-to-parallel converter is block spreaded using Walsh-Hadammard codes and pass through a chip-interleaving process before modulated using IFFT. Since the total number of data sub-carriers($M.G$) is fixed at 100, we can calculate M based on the different spreading factor G used. At the receiver, the *LLR* for each bit is calculated as illustrated in Section 4.1. We shall compare the performance of the maximum likelihood detection receiver and its simplified form for spreading factor of 2, 4 and 8. We shall simulate the system performance for the data rate of 480 Mbps and the block diagram of the transceiver structure is given in Figure 4.4. Note that in our simulation, we consider convolutional codes as the error-correcting codes instead of the LDPC codes discussed in Chapter 3 so that the performance improvement due to the use of spreading can be more clearly illustrated.

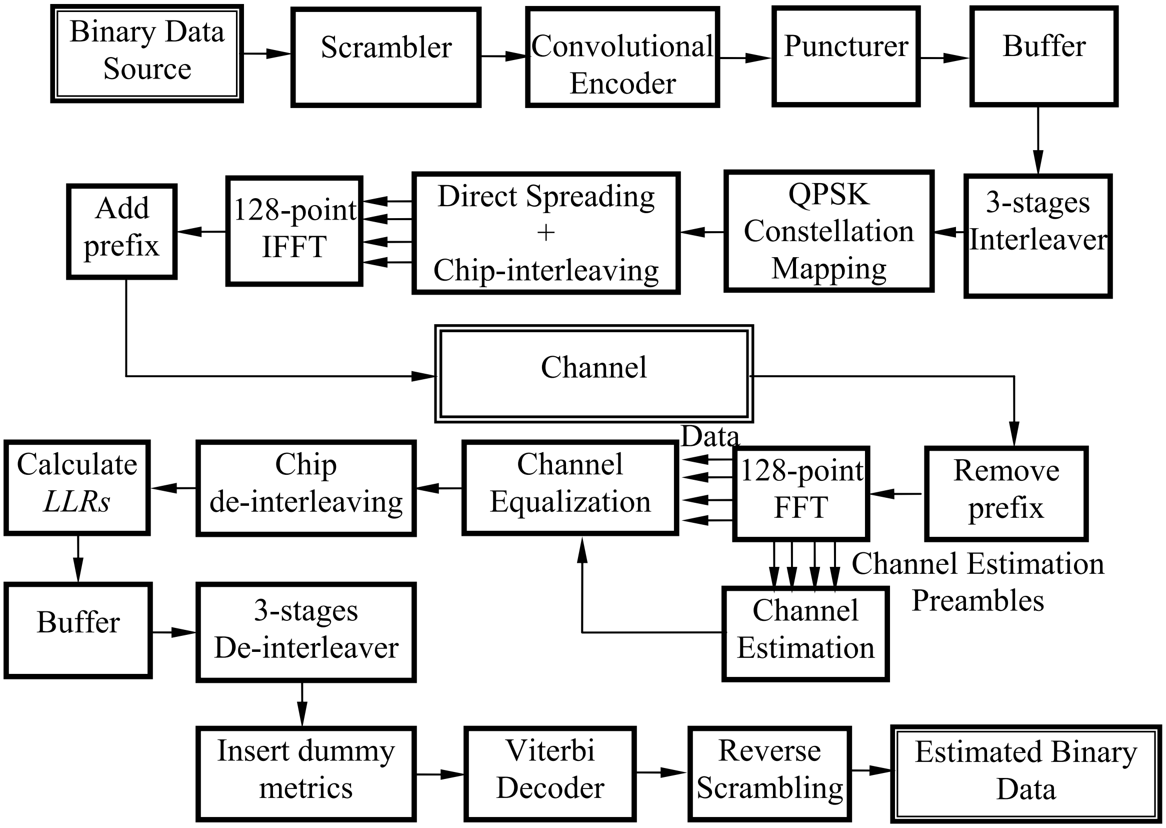

Figure 4.4: MB-OFDM UWB System with direct spreading and chip-interleaving.

The performance of the proposed MB-OFDM UWB system in Channel Model 1 and 3 introduced in Chapter 2 is simulated and compared to the performance of a MB-OFDM UWB system without direct spreading. Channel Model 1 and 3 is chosen as Channel Model 1 represents the best transmission channel with line-of-sight between the transmitter and receiver antenna while Channel Model 3 represents the worst transmission channel modeled accordingly to actual measurement with the longest delay spread statistics and hence the most frequency selective. For each of the channel models, all one hundred realizations of the channel model are used as the channel conditions the system is transmitting over. In both channel models, it is assumed that the channel conditions remain unchanged during the transmission of a single packet of data (quasi-static). The transmission of 50 packets each containing 1024 bytes of information bits in each realization of the channel models are simulated and the packet-error rate (PER) is calculated at the receiver as per detailed in Chapter 2. The salient features of the simulated system are summarized in Table 4.1.

The PER performances of the systems in Channel Model 1 and 3 are shown in Figure 4.5 and Figure 4.6 respectively. From the figures, it can be seen that the proposed direct spreading helps to improve the performance of the MB-OFDM UWB system. Using maximum likelihood detection, taking PER = 0.08 as reference, there is a performance gain of 1.5 dB, 2.5 dB and 3.1 dB in CM1 for spreading factor = 2, 4 and 8 respectively. In CM3, the performance gain is more significant at 2.0 dB, 3.9 dB and 5.1 dB respectively. The performance gain in CM3 is more significant as CM3 represents channel conditions with relatively longer delay spread and hence smaller bandwidth coherence. Therefore, the frequency diversity among the sub-carriers is more significant in CM3 than in CM1. Since, the direct spreading improve the performance by exploiting the frequency diversity among the sub-carriers, the proposed system is able to achieve higher gain in CM3. Also, we can see that the performance gain does not increase in proportion with the spreading factor used. This is natural, as with a fixed number of data sub-carriers, the increase in spreading factor would result in a decrease in the channel variations between the sub-carriers carrying the same symbol. In other words, there is a limit to the amount of frequency diversity available in each sub-band.

Table 4.1: Salient Features of Simulated System

Systems	System without Frequency Spreading	System with Frequency Spreading (ML Decoder)	System with Frequency Spreading (Simplified Decoder)
Data Rate	480 Mbps	480 Mbps	480 Mbps
FFT Size	128	128	128
Number of Data sub-carriers	100	100	100
Code Rate	0.75	0.75	0.75
Sub-carriers Modulation	QPSK	QPSK	QPSK
FEC	Convolutional Code	Convolutional Code	Convolutional Code
Direct Frequency Spreading with Chip-interleaving	Not Employed	Employed	Employed
Conjugate Symmetric Inputs	Not Employed	Not Employed	Not Employed
Time Spreading	Not Employed	Not Employed	Not Employed
Channel Estimation	Prefect Channel Estimates	Prefect Channel Estimates	Prefect Channel Estimates
Frequency Offset	None	None	None
Spreading Decoding	Not Employed	Maximum Likelihoods Decoder	Simplified Decoder

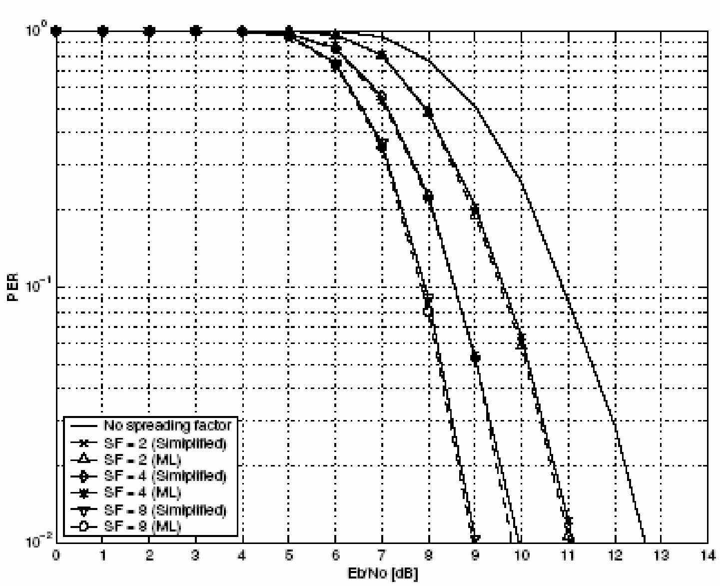

Figure 4.5: PER Performance for MB-OFDM UWB in CM1.

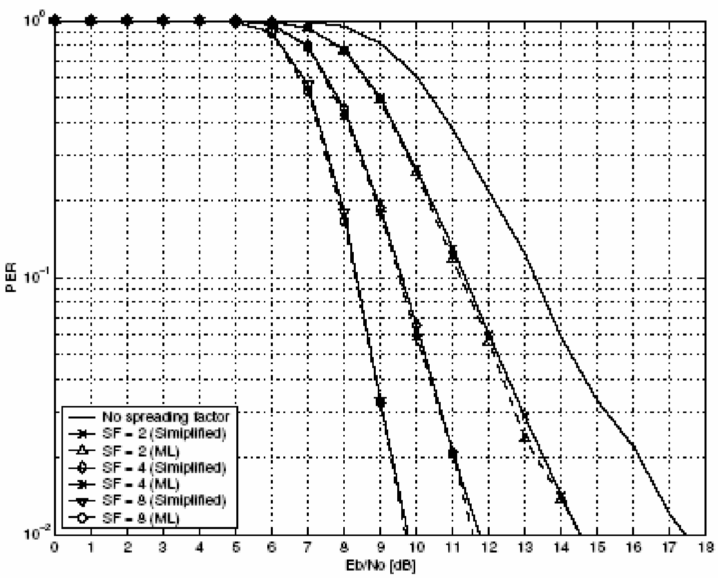

Figure 4.6: PER Performance for MB-OFDM UWB in CM3.

As for the performance of the simplified form of the maximum likelihood detection receiver, the simulation results show that there is no significant degradation in performance compared to the maximum likelihood detection receiver. Moreover, the simplified method reduces the amount of computational complexity required to perform maximum likelihood detection for high spreading factor significantly. The simulation results also shown that we are able to improve the performance of a MB-OFDM UWB system with a relatively simple block spreading and chip interleaving scheme.

4.3 Conclusions

In this chapter, a novel block spreading with chip interleaving scheme is applied for MB-OFDM UWB system. Through simulation, it has been shown that the system performance can be improved by this relatively simple modification. At PER = 0.08, the proposed system with spreading factor of 8 achieves a performance gain of of 3.1 dB and 5.1 dB in Channel Model 1 and Channel Model 3 respectively. Furthermore, the block spreading and chip interleaving scheme can be combined and be easily implemented using a simple block interleaver and banks of adders. At the receiver, a simplified maximum likelihood detection method is employed to effectively make use of the diversity gain due to the direct spreading. Simulation results show that there is no appreciable degradation in performance using the simplified method compared to using maximum likelihood detection. The results also show that the performance of the proposed scheme improves with increasing the spreading factor. Hence the possibility exists for a trade-off between receiver complexity and system performance.

Chapter 5

Frequency Offsets Estimation and Compensation

A major disadvantage of multi-band OFDM (MB-OFDM) system is its performance sensitivity to frequency offset. The effect of a fixed frequency offset between the transmitter and receiver local oscillators on the performance of OFDM system is well-known [7][9]. As such there are a lot of algorithms [24]-[28] that aims to estimate and compensate for the effects of the frequency offset in OFDM system. In this chapter, we describe a few of these methods and discuss the feasibility of using them in a MB-OFDM UWB system. Furthermore, a new estimation and compensation algorithm for frequency offsets in MB-OFDM UWB system will be introduced and evaluated though the use of simulation of a MB-OFDM UWB system using the new algorithm.

5.1 Effects of Frequency Offset

In a practical OFDM system, a fixed frequency offset between the transmitter and receiver local oscillators usually exists. For the proposed MB-OFDM UWB system, the transmitter and receiver will each function using a single local oscillator for generating the different carrier frequency as well as the sampling frequency. Also, the authors of the proposed system recommended the use of oscillator components that will limit the offset of the generated frequency to the desired frequency by a maximum of ±20 parts per million (ppm).

Following the methods used in [9][29], we derived the effects of frequency offset on the received data in the proposed MB-OFDM UWB system. Let the carrier frequencies for the 3 different sub-bands generated at the transmitter be f_1, f_2 and f_3 respectively. Next, denote the carrier frequencies generated at the receiver as

$$\begin{aligned} f_1' &= f_1 + \delta f_1 \\ f_2' &= f_2 + \delta f_2 \\ f_3' &= f_3 + \delta f_3 \end{aligned} \tag{5.1}$$

where δ represents the normalized frequency offsets between the transmitter and receiver.

Since the offset in the local oscillator generated frequency is limited to ±20ppm, $|\delta| \leq 40$ppm. Similarly, the sampling frequency generated at the transmitter and receiver can be denoted as f_s and $f_s' = (1+\delta) f_s$ respectively. The sampling frequency offset will result in an offset in sampling interval. If the sampling interval at the transmitter is denoted as T_s, then the sampling interval at the receiver would be written as

$$\begin{aligned} T_s' &= \frac{1}{(1+\delta) f_s} \\ &= \frac{1}{1+\delta} T_s \\ &= T_s - \frac{\delta}{1+\delta} T_s \\ &= T_s + \Delta T_s \end{aligned} \tag{5.2}$$

where

$$\Delta = -\frac{\delta}{1+\delta} \tag{5.3}$$

For simplicity, we assume that the designed prefix duration for the MB-OFDM UWB system is long enough to ensure that no inter-symbol interference (ISI) occurs. Let N be the number of FFT sample points and M be the number of total samples per OFDM symbol including the zero prefix samples and guard interval samples introduced in Chapter 2. We denote the complex symbol at the k^{th} sub-carrier for the i^{th} OFDM symbol as $X_{i,k}$ and the complex baseband transfer function of the c^{th} sub-band channel at the k^{th} sub-carrier as $H_{c,k}$. Here we assume that the radio frequency channel is quasi-static in that it does not fluctuate with time during one packet transmission duration. For ease of representation, we also introduced a sequence c_i, govern by the time-frequency codes (TFC) used for the transmission, which represent the sub-bands number for the i^{th} symbol.

Using the defined notations, the received complex baseband signal can then be written as

$$r(t) = \sum_i \left[\left(\frac{1}{N} \sum_{k=-\frac{N}{2}}^{\frac{N}{2}-1} X_{i,k} H_{c_i,k} e^{j2\pi \frac{k}{NT_s}(t-iMT_s)} \right) e^{j2\pi \delta f_{c_i} t} \right] u\left(t - iMT_s\right) + \eta(t) \qquad (5.4)$$

where $\eta(t)$ is the complex baseband additive white Gaussian noise (AWGN) and $u\left(t\right)$ is a rectangle function defined by Equation (4.5) below.

$$u(t) = \begin{cases} 1 & 0 \le t \le MT_s \\ 0 & elsewhere \end{cases} \qquad (5.5)$$

At the receiver, the received signal is sampled according to the sampling frequency of the local oscillator to obtain the N sample points for each OFDM symbol required for the demodulation process. Let n denotes the sample index at the receiver for each OFDM symbol such that n = 0, 1,…, N-1. If the initial symbol timing synchronization is accurate, the received N samples for the i^{th} OFDM symbol will then be given by

$$\begin{aligned} r_{i,n} &= r((iM+n)T_s') \\ &= e^{j2\pi\delta f_{c_i}(iM+n)T_s'}\left(\frac{1}{N}\sum_{k=-\frac{N}{2}}^{\frac{N}{2}-1} X_{i,k}H_{c_i,k}e^{j2\pi\frac{iM\Delta k}{N}}e^{j2\pi\frac{nk}{N}(1+\Delta)}\right)+\eta_{i,n} \end{aligned} \tag{5.6}$$

Applying FFT to the each group of N samples, we can obtain the received complex symbol, $R_{i,m}$, for the m^{th} sub-carrier of the i^{th} OFDM symbol.

$$\begin{aligned} R_{i,m} &= \sum_{n=0}^{N-1}\left(e^{j2\pi\delta f_{c_i}(iM+n)T_s'}\left(\frac{1}{N}\sum_{k=-\frac{N}{2}}^{\frac{N}{2}-1} X_{i,k}H_{c_i,k}e^{j2\pi\frac{iM\Delta k}{N}}e^{j2\pi\frac{nk}{N}(1+\Delta)}\right)\right)e^{-j2\pi\frac{nm}{N}}+V_{i,m} \\ &= \frac{1}{N}\sum_{k=-\frac{N}{2}}^{\frac{N}{2}-1} X_{i,k}H_{c_i,k}e^{j2\pi\frac{iM\Delta k}{N}}e^{j2\pi iM\delta f_{c_i}T_s'}\sum_{n=0}^{N-1}e^{j2\pi\delta f_{c_i}nT_s'}e^{j2\pi\frac{nk}{N}(1+\Delta)}e^{-j2\pi\frac{nm}{N}}+V_{i,m} \\ &= \frac{1}{N}\sum_{k=-\frac{N}{2}}^{\frac{N}{2}-1}\widetilde{X}_{i,k}\sum_{n=0}^{N-1}e^{j2\pi\delta f_{c_i}nT_s'}e^{j2\pi\frac{nk}{N}(1+\Delta)}e^{-j2\pi\frac{nm}{N}}+V_{i,m} \\ &= \widetilde{X}_{i,m}I_{m,m}+\sum_{\substack{k=-\frac{N}{2} \\ k\neq m}}^{\frac{N}{2}-1}\widetilde{X}_{i,k}I_{k,m}+V_{i,m} \end{aligned} \tag{5.7}$$

where

$$\widetilde{X}_{i,k} = X_{i,k}H_{c_i,k}e^{j2\pi\frac{iM\Delta k}{N}}e^{j2\pi iM\delta f_{c_i}T_s'} \tag{5.8}$$

$$I_{k,m} = \frac{1}{N}\sum_{n=0}^{N-1}e^{j2\pi\delta f_{c_i}nT_s'}e^{j2\pi\frac{nk}{N}(1+\Delta)}e^{-j2\pi\frac{nm}{N}} \tag{5.9}$$

and $V_{i,m}$ is the FFT transform of the AWGN component. $I_{k,m}$ can be simplified by considering it as a sum of geometric series.

Therefore,

$$
\begin{aligned}
I_{k,m} &= \frac{1}{N}\sum_{n=0}^{N-1}\exp\left(j2\pi\delta f_{c_i} nT_s'\right)\exp\left(j2\pi\frac{nk}{N}(1+\Delta)_s\right)\exp\left(-j2\pi\frac{nm}{N}\right)\\
&= \frac{1}{N}\sum_{n=0}^{N-1}\exp\left\{j2\pi n\left(\delta f_{c_i}T_s' + \frac{1}{N}\left[(1+\Delta)k - m\right]\right)\right\}\\
&= \frac{1}{N}\frac{1-\exp\left\{j2\pi N\left(\delta f_{c_i}T_s' + \frac{1}{N}\left[(1+\Delta)k - m\right]\right)\right\}}{1-\exp\left\{j2\pi\left(\delta f_{c_i}T_s' + \frac{1}{N}\left[(1+\Delta)k - m\right]\right)\right\}}\\
&= \left(\frac{1}{N}\left\{\frac{\exp\left\{-j\pi N\left(\delta f_{c_i}T_s' + \frac{1}{N}\left[(1+\Delta)k - m\right]\right)\right\} - \exp\left\{j\pi N\left(\delta f_{c_i}T_s' + \frac{1}{N}\left[(1+\Delta)k - m\right]\right)\right\}}{\exp\left\{-j\pi\left(\delta f_{c_i}T_s' + \frac{1}{N}\left[(1+\Delta)k - m\right]\right)\right\} - \exp\left\{j\pi\left(\delta f_{c_i}T_s' + \frac{1}{N}\left[(1+\Delta)k - m\right]\right)\right\}}\right\}\right.\\
&\qquad\left.\cdot\left\{\frac{\exp\left\{j\pi N\left(\delta f_{c_i}T_s' + \frac{1}{N}\left[(1+\Delta)k - m\right]\right)\right\}}{\exp\left\{j\pi\left(\delta f_{c_i}T_s' + \frac{1}{N}\left[(1+\Delta)k - m\right]\right)\right\}}\right\}\right)
\end{aligned}
$$

giving

$$
I_{k,m} = \frac{\sin\left(\pi\left(k\frac{T_s'}{T_s} - m + N\delta f_{c_i}T_s'\right)\right)}{N\sin\left(\frac{\pi}{N}\left(k\frac{T_s'}{T_s} - m + N\delta f_{c_i}T_s'\right)\right)}\exp\left(j\pi\frac{N-1}{N}\left(k\frac{T_s'}{T_s} - m + N\delta f_{c_i}T_s'\right)\right) \qquad (5.10)
$$

For the case of k = m,

$$
I_{m,m} = \frac{\sin\left(\pi\left(m\Delta + N\delta f_{c_i}T_s'\right)\right)}{N\sin\left(\frac{\pi}{N}\left(m\Delta + N\delta f_{c_i}T_s'\right)\right)}\exp\left(j\pi\frac{N-1}{N}\left(m\Delta + N\delta f_{c_i}T_s'\right)\right) \qquad (5.11)
$$

From Equation (5.7), we can see that the frequency offset causes inter-carrier interference (ICI) among the sub-carriers as represented by the second term in Equation (5.7). For zero-mean and uncorrelated transmitted complex symbols, the mean and variance of the ICI component is given by Equation (5.12) and Equation (5.13) respectively. Here, we assume that the average channel gain, $E\left[\left|H_{c_i,k}\right|^2\right] = |H|^2$, is a constant for all sub-bands and the transmitted signal energy is denoted as E_s.

$$E\left[\sum_{\substack{k=-\frac{N}{2} \\ k\neq m}}^{\frac{N}{2}-1} \widetilde{X}_{i,k} I_{k,m}\right] = \sum_{\substack{k=-\frac{N}{2} \\ k\neq m}}^{\frac{N}{2}-1} E\left[\widetilde{X}_{i,k}\right] I_{k,m} = 0 \tag{5.12}$$

$$\begin{aligned} Var\left[\sum_{\substack{k=-\frac{N}{2} \\ k\neq m}}^{\frac{N}{2}-1} \widetilde{X}_{i,k} I_{k,m}\right] &= E\left[\left(\sum_{\substack{k=-\frac{N}{2} \\ k\neq m}}^{\frac{N}{2}-1} \widetilde{X}_{i,k} I_{k,m}\right)\left(\sum_{\substack{k=-\frac{N}{2} \\ k\neq m}}^{\frac{N}{2}-1} \widetilde{X}_{i,k} I_{k,m}\right)^*\right] \\ &= \left|X_{i,k}\right|^2 \sum_{\substack{k=-\frac{N}{2} \\ k\neq m}}^{\frac{N}{2}-1} \left|I_{k,m}\right|^2 E\left[\left|H_{c_i,k}\right|^2\right] \\ &= \frac{E_s|H|^2}{N^2} \sum_{\substack{k=-\frac{N}{2} \\ k\neq m}}^{\frac{N}{2}-1} \frac{\sin^2\left(\pi\left(k\frac{T_s'}{T_s} - m + N\delta f_{c_i} T_s'\right)\right)}{\sin^2\left(\frac{\pi}{N}\left(k\frac{T_s'}{T_s} - m + N\delta f_{c_i} T_s'\right)\right)} \end{aligned} \tag{5.13}$$

The variance of the ICI term is dependent on the sub-carrier index *m* and the frequency offset. Moreover, the effect of the carrier frequency offset represented by the term

$N\delta f_{c_i} T_s'$ on the ICI variance is much more significant than that of the sampling frequency offset.

In addition to causing ICI, the frequency offset will also result in attenuation and phase rotation of the received complex symbol strength as can be seen from Equation (5.8) and Equation (5.11). The received complex symbols suffer from 4 different types of phase distortion due to frequency offset. We can divide the phase rotation into 4 different types of phase rotations, ϕ_a, ϕ_b, ϕ_c and ϕ_d accordingly to their characteristics,

$$\begin{aligned} \phi_a &= 2\pi \frac{iM\Delta k}{N} \\ \phi_b &= 2\pi iM\delta f_{c_i} T_s' \\ \phi_c &= \pi k\Delta \frac{N-1}{N} \\ \phi_d &= \pi(N-1)\delta f_{c_i} T_s' \end{aligned} \tag{5.14}$$

As can be seen from Equation (5.12), the magnitudes of ϕ_a and ϕ_b increase over time while those of ϕ_c and ϕ_d remain constant. The phase rotations ϕ_b and ϕ_d are the result of the carrier frequency offset while ϕ_a and ϕ_c are the result of the sampling frequency offset. Also, of the 4 phase rotations only ϕ_a and ϕ_c are dependent of the sub-carrier index while the rest are independent of it.

5.2 Conventional Frequency Offset Estimation and Compensation

From the discussion in the section above, if one disregards the contribution of ICI term, the effects of frequency offset can be said to be predominately a phase distortion of the transmitted complex sub-carrier symbol. Therefore it is possible to estimate the frequency offset by transmitting a few known preamble OFDM symbols before each frame and derived the frequency offset from the phase distortion information received [25]. More specifically, by considering the phase difference between successive preamble OFDM symbols, the phase distortions denoted as ϕ_c and ϕ_d can be eliminated. The sampling frequency offset can then be estimated by calculating the phase shift between adjacent sub-carriers. The carrier frequency offset is then estimated using the sampling frequency offset estimate obtained [25]. Assuming that 2 identical preamble OFDM symbols is transmitted in the same sub-band and the frequency domain received symbols are denoted as $R_{1,m}$ and $R_{2,m}$, the estimate of the normalized sampling offset is then given by

$$\hat{\Delta} = \frac{N}{2M\pi(N-1)} \sum_{m=-\frac{N}{2}+1}^{\frac{N}{2}-1} \left[\tan^{-1}\left(\frac{\operatorname{Im}\{R_{2,m}R_{1,m}^{*}\}}{\operatorname{Re}\{R_{2,m}R_{1,m}^{*}\}} \right) - \tan^{-1}\left(\frac{\operatorname{Im}\{R_{2,m-1}R_{1,m-1}^{*}\}}{\operatorname{Re}\{R_{2,m-1}R_{1,m-1}^{*}\}} \right) \right] \tag{5.15}$$

and the normalized carrier frequency offset is given by

$$\hat{\delta} = \frac{1}{2\pi MNf_{c_i}\hat{T}'_s} \sum_{m=-\frac{N}{2}}^{\frac{N}{2}-1} \left[\tan^{-1}\left(\frac{\operatorname{Im}\{R_{2,m}R_{1,m}^{*}\}}{\operatorname{Re}\{R_{2,m}R_{1,m}^{*}\}} \right) - 2\pi\frac{mM}{N}\hat{\Delta} \right] \tag{5.16}$$

In Equation (5.15), the estimates of the sampling offset are averaged without regards to the performance of the estimator in noisy environment. Other possible averaging methods like weighted averaging using the signal-to-noise ratio (SNR) of the different sub-carriers as weights [26] or adaptive averaging algorithm can be used [27] to better the performance of the estimator. Naturally, these methods can also be extended to the averaging of the carrier frequency offset estimates. Though these averaging algorithms would help in increasing the accuracy of the estimates, the use of them could not counter the influence of the ICI term on the estimates efficiently.

As can be seen from Equation (5.13), the ICI term is very significant even for small normalized carrier frequency offset especially if the carrier frequency f_{c_i} is very much larger than the sub-carrier frequency spacing $1/NT_s$ as usually is the case for UWB MB-OFDM UWB system. In the presence of significant ICI, estimates obtained using Equations (5.15) and (5.16) with or without advanced averaging algorithm will not be accurate or reliable. To minimize the ICI term, compensation of the carrier frequency offset to the time domain samples must be made prior to the FFT process. In other words, an estimation of the carrier frequency offset must be made using time domain received data. One estimation algorithm is to make use of auto-correlation of the received time domain samples of 2 identical transmitted OFDM symbol preambles [25][28]. For example, let 2 identical OFDM symbols be transmitted in Band 1 consecutively and assuming that the sampling frequency offset is negligible, the estimation of the frequency offset will then be given by Equation (5.17) where $r_{0,n}$ and $r_{1,n}$ are the received time domain samples.

$$\hat{\delta f}_1 = \frac{1}{2\pi MT} \tan^{-1}\left(\frac{\mathrm{Im}\left\{ \sum_{n=0}^{N} r_{0,n}^{*} r_{1,n} \right\}}{\mathrm{Re}\left\{ \sum_{n=0}^{N} r_{0,n}^{*} r_{1,n} \right\}} \right) \tag{5.17}$$

In Equation (5.17), the assumption that the magnitude of the phase difference caused by the carrier frequency offset is less than π so as to ignore the possibilities of ambiguity [28]. In other words,

$$\left|\tan^{-1}\left(\frac{\operatorname{Im}\left\{\sum_{n=0}^{N} r_{0,n}^{*} r_{1,n}\right\}}{\operatorname{Re}\left\{\sum_{n=0}^{N} r_{0,n}^{*} r_{1,n}\right\}}\right)\right| < \pi \tag{5.18}$$

The validity of the assumption given in Equation (5.18) can be easily proven by considering the magnitude of the phase difference that would be caused by the maximum specified normalized frequency offset of 40ppm and largest carrier frequency f_3.

$$\begin{aligned}\max\left(\left|\tan^{-1}\left(\frac{\operatorname{Im}\left\{\sum_{n=0}^{N} r_{0,n}^{*} r_{1,n}\right\}}{\operatorname{Re}\left\{\sum_{n=0}^{N} r_{0,n}^{*} r_{1,n}\right\}}\right)\right|\right) &= \max\left(\left|2\pi MT\hat{\delta f}_3\right|\right) \\ &= 2\pi MT\max\left(\left|\delta f_3\right|\right) \\ &= 0.1122\pi \end{aligned} \tag{5.19}$$

These conventional methods of joint estimating the carrier and sampling frequency offset effects proved to be very effective for single-band OFDM system [25][26] and can be used together with compensation techniques such as digital interpolation [29] or digital domain equalizer [9] to counteract the distortions.

However, a critical change is needed in the algorithms to adapt them for the frequency hopping characteristic in a MB-OFDM UWB system. Since consecutive OFDM symbols are transmitted in different sub-bands, the consecutive received preambles cannot be used to determine the sampling and carrier frequency offset like in Equations (5.15) to (5.17). Instead, adjacent OFDM preambles transmitted in each of the different sub-bands must be used. In other words, instead of storing the received data for 2 preambles to do the frequency offset estimation, 6 preambles data must be stored. Moreover, the estimation of the normalized frequency offset is done for different sub-bands even though the estimates are of the same quantity. Of course one can choose to do the estimation for a particular sub-band only and use the appropriate transformation to do compensation for the remaining sub-bands. However, this would then require an adaptive selection of the best sub-band to do the estimation in order to achieve a consistently high quality in the estimates.

5.3 A Novel Joint Frequency Offset Estimation Method

In this section, we introduced a novel joint carrier and sampling frequency offset estimation algorithm for MB-OFDM UWB system that enable use to obtain accurate estimates that can be used to compensate for the phase distortions using a digital domain equalizer [9]. The algorithm first uses 6 preambles (2 for each sub-band) of the 18 preambles provided for in the proposed system detailed in Chapter 2 to estimate the carrier frequency offset. The estimate obtained is then used to correct for the carrier frequency offset in the time domain for the data symbols. Next, we use the phase information of the pilot sub-carriers available in each OFDM symbol to carry out an iterative estimation of the sampling frequency offset as well as any residual carrier frequency offset that may be present.

Let assume that the transmission of packets are carried out using TFC#1 mentioned in Chapter 2. The carrier frequency offset for each sub-band is estimated using 3 OFDM preamble symbols. The estimation is done by using a variation of Equation (5.17). Instead of using consecutive OFDM preambles for estimation, adjacent OFDM preambles transmitted in each sub-band are used. If we indexed the 9 preamble symbols from 0 to 8, then the preambles indexed 0, 3 and 6 will be transmitted in Band 1, the preambles indexed 1, 4 and 7 will be transmitted in Band 2 and the preambles indexed 2, 5 and 8 will be transmitted in Band 3. Mathematically, the estimates of the carrier frequency offsets are given by Equation (5.20).

$$\begin{aligned}
\hat{\delta}_1 f_1 &= \frac{1}{6\pi M T_s}\tan^{-1}\left(\frac{\operatorname{Im}\left\{\sum_{i=0,3}\sum_{n=0}^{N} r_{i,n}^{*} r_{i+3,n}\right\}}{\operatorname{Re}\left\{\sum_{i=0,3}\sum_{n=0}^{N} r_{i,n}^{*} r_{i+3,n}\right\}}\right) \\
\hat{\delta}_2 f_2 &= \frac{1}{6\pi M T_s}\tan^{-1}\left(\frac{\operatorname{Im}\left\{\sum_{i=1,4}\sum_{n=0}^{N} r_{i,n}^{*} r_{i+3,n}\right\}}{\operatorname{Re}\left\{\sum_{i=1,4}\sum_{n=0}^{N} r_{i,n}^{*} r_{i+3,n}\right\}}\right) \\
\hat{\delta}_3 f_3 &= \frac{1}{6\pi M T_s}\tan^{-1}\left(\frac{\operatorname{Im}\left\{\sum_{i=2,5}\sum_{n=0}^{N} r_{i,n}^{*} r_{i+3,n}\right\}}{\operatorname{Re}\left\{\sum_{i=2,5}\sum_{n=0}^{N} r_{i,n}^{*} r_{i+3,n}\right\}}\right)
\end{aligned} \tag{5.20}$$

Note that Equation (5.20) also satisfies the assumption laid out in Equation (5.18). In other words, the magnitude of the phase difference between adjacent symbols in the same sub-band does not exceed π. The estimates from each sub-band is averaged to form an averaged estimate, $\bar{\hat{\delta}}$, which is are then used to correct the time domain samples for the subsequent OFDM data symbols [25].

$$\bar{\hat{\delta}} = \frac{1}{3}\sum_{i=1}^{3}\hat{\delta}_i \tag{5.21}$$

The corrected samples are then passed to the FFT to do demodulation. The received complex symbol, $R_{i,m}$, initially represented by Equation (5.7) is rewritten to take into account the phase correction in time domain. If we denote the residual normalized frequency offset after the correction as $\tilde{\delta}$ where

$$\tilde{\delta} = \delta - \bar{\hat{\delta}} \tag{5.22}$$

then the received complex symbol $R_{i,m}$ is rewritten as

$$R_{i,m} = \tilde{X}_{i,m} I'_{m,m} + \sum_{\substack{k=-\frac{N}{2} \\ k \neq m}}^{\frac{N}{2}-1} \tilde{X}_{i,k} I'_{k,m} + V_{i,m} \tag{5.23}$$

where

$$I'_{k,m} = \frac{\sin\left(\pi\left(k\frac{T'_s}{T_s} - m + N\tilde{\delta} f_{c_i} T'_s\right)\right)}{N\sin\left(\frac{\pi}{N}\left(k\frac{T'_s}{T_s} - m + N\tilde{\delta} f_{c_i} T'_s\right)\right)} \exp\left(j\pi\frac{N-1}{N}\left(k\frac{T'_s}{T_s} - m + N\tilde{\delta} f_{c_i} T'_s\right)\right) \tag{5.24}$$

At the FFT output, a single-tap equalizer is used to neutralize the effects of the frequency-selective fading. For simplicity, we assume that the prefect channel estimates for each sub-carrier is available at the receiver in this chapter. The estimation of the channel and its effects will be discussed in more details in Chapter 6. The equalization process can be written as

$$\begin{aligned} Y_{i,k} &= H_{c_i,k} R_{i,k} \\ &= X_{i,k} \left| H_{c_i,k} \right|^2 e^{j2\pi \frac{iM\Delta k}{N}} e^{j2\pi i M \delta f_{c_i} T_s'} I'_{m,m} + H_{c_i,k} \left(\sum_{\substack{k=-\frac{N}{2} \\ k \neq m}}^{\frac{N}{2}-1} \widetilde{X}_{i,k} I'_{k,m} + V_{i,m} \right) \end{aligned} \tag{5.25}$$

where $Y_{i,k}$ is the output of the equalizer.

Ignoring the ICI and AWGN term, the phase distortion to the equalized k^{th} sub-carrier can therefore be written as

$$\theta_{i,k} = k \cdot \left(i \cdot \varphi_a + \varphi_c \right) + i \cdot f_{c_i} \cdot \varphi_b + f_{c_i} \cdot \varphi_d \tag{5.26}$$

where

$$\begin{aligned} \varphi_a &= 2\pi \frac{M\Delta}{N} \\ \varphi_b &= 2\pi M \widetilde{\delta} T_s' \\ \varphi_c &= \pi \frac{\Delta(N-1)}{N} \\ \varphi_d &= \pi (N-1) \widetilde{\delta} T_s' \end{aligned} \tag{5.27}$$

and φ_a, φ_b, φ_c and φ_d are constants throughout a packet.

To obtain the phase distortion for the pilot sub-carriers, the output of the equalizer is divided by the known transmitted data and the phase of the resulting complex numbers is calculated. For a particular OFDM index *i,* the phase distortion can be said to be a linear function of the sub-carrier index *k*. Hence, it is possible to apply the linear least-square curve fitting criterion to the noisy pilot phase data to obtain a linear best-fit line for each OFDM symbol's phase distortion plot. Incidentally, this method is commonly used to estimate and correct for the phase distortions due to the frequency offset.

Moreover, one can easily observed that the gradient of the linear best-fit line actually gives an estimation of a linear function, μ_i, which relates the phase distortion to the OFDM symbol index while the phase-intercept gives an estimation of another linear function λ_i that relates the phase distortion to the OFDM symbol index.

$$\begin{aligned} \mu_i &= i \cdot \varphi_a + \varphi_c \\ \lambda_i &= i \cdot f_{c_i} \cdot \varphi_b + f_{c_i} \cdot \varphi_d \end{aligned} \tag{5.28}$$

To better the estimates, the averaging of the estimates across the symbol index can be performed. Based on this principle of two-dimensional estimation, an iterative estimation of the phase distortion is carried out. In Figure 5.1, the flowchart of the estimation algorithm is illustrated.

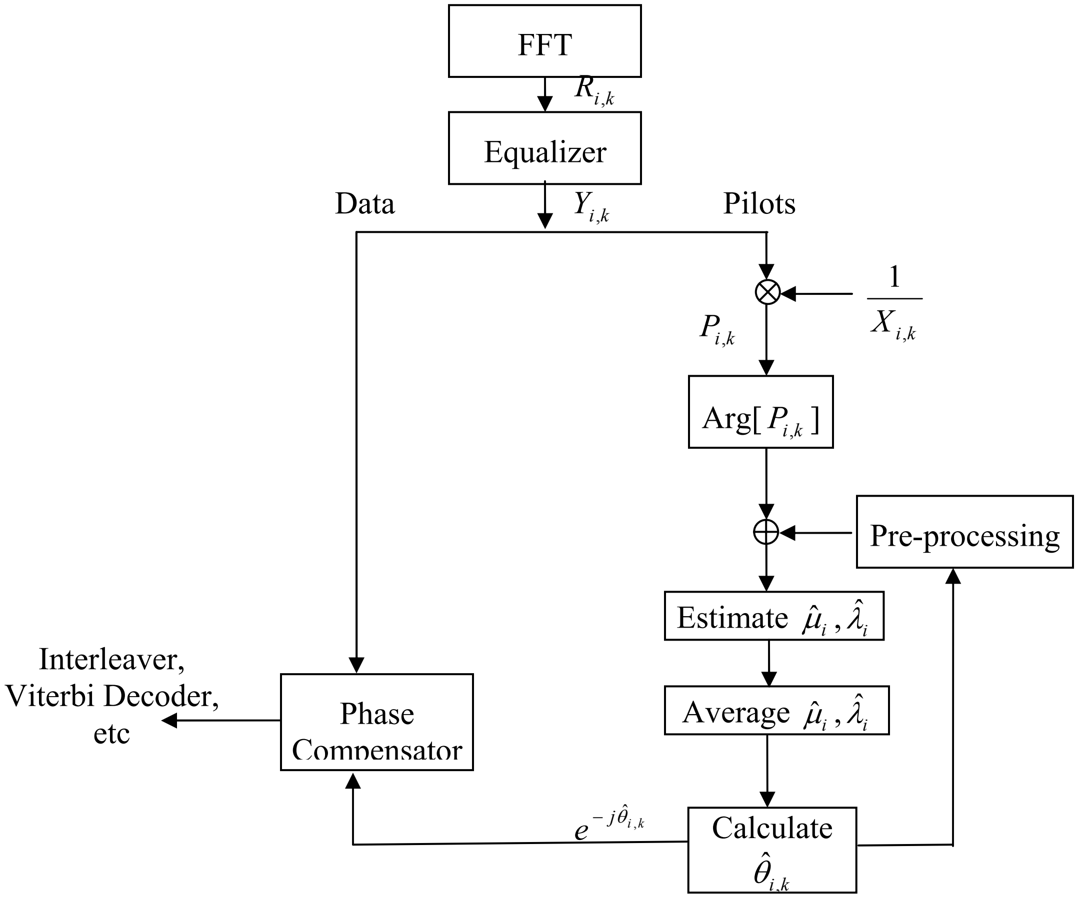

Figure 5.1: Flowchart of Frequency Offset Estimation and Compensation Algorithm.

If k_p denotes the group of the pilot sub-carrier index, k_p = [-55, -45, …, 0, 5, …, 55], then

$$\rho_{i,k} = \mathrm{Arg}\left[\frac{Y_{i,k}}{X_{i,k}}\right], k \in k_g \tag{5.29}$$

Hence, $\rho_{i,k}$ denotes the measured phase of the pilot sub-carrier after equalization and division by known transmitted data. Applying the linear least-square curve fitting criterion [30] to the set of measured phases and pilot sub-carrier indices and simplifying the expressions, we get the estimations of μ_i and λ_i as

$$\hat{\mu}_i = \frac{\sum_{k \in k_p} k \cdot \rho_{i,k}}{\sum_{k \in k_p} k^2} \tag{5.30}$$

$$\hat{\lambda}_i = \frac{1}{N_p} \sum_{k \in k_p} \rho_{i,k} \tag{5.31}$$

From Equation (5.27), note that the contributions of φ_c and φ_d to the overall phase distortion are small and negligible especially for large *i*. Therefore, ignoring φ_c and φ_d in the averaging process, we get the average estimations of μ_i and λ_i across successive OFDM symbols as

$$\overline{\hat{\mu}}_i = i \cdot \frac{\sum_{\gamma=1}^{i} \hat{\mu}_\gamma}{\sum_{\gamma=1}^{i} \gamma} \tag{5.32}$$

$$\overline{\hat{\lambda}}_i = i \cdot \frac{\sum_{\gamma=1}^{i} \hat{\lambda}_\gamma \big/ f_{c_\gamma}}{\sum_{\gamma=1}^{i} \gamma} \tag{5.33}$$

To avoid excessive storage of variables, Equation (5.32) and Equation (5.33) can be rewritten in an iterative form.

$$\begin{aligned}
\bar{\hat{\mu}}_i &= i \cdot \frac{\sum\limits_{\gamma=1}^{i} \hat{\mu}_\gamma}{\sum\limits_{\gamma=1}^{i} \gamma} \\
&= i \cdot \left(\frac{\left(\sum\limits_{\gamma=1}^{i-1} \gamma \right)}{\left(\sum\limits_{\gamma=1}^{i-1} \gamma \right)} \frac{\left(\hat{\mu}_i + \sum\limits_{\gamma=1}^{i-1} \hat{\mu}_\gamma \right)}{\left(\sum\limits_{\gamma=1}^{i} \gamma \right)} \right) \\
&= i \cdot \left(\frac{\frac{1}{2}(i-1)i}{\frac{1}{2} i(i+1)\left(i-1\right)} \bar{\hat{\mu}}_{i-1} + \frac{1}{\frac{1}{2} i(i+1)} \hat{\mu} \right) \\
&= \frac{i}{i+1} \bar{\hat{\mu}}_{i-1} + \frac{2}{i+1} \hat{\mu}_i
\end{aligned} \tag{5.34}$$

$$\begin{aligned}
\bar{\hat{\lambda}}_i &= i \cdot \frac{\sum\limits_{\gamma=1}^{i} \hat{\lambda}_\gamma \big/ f_{c_\gamma}}{\sum\limits_{\gamma=1}^{i} \gamma} \\
&= i \cdot \left(\frac{\left(\sum\limits_{\gamma=1}^{i-1} \gamma \right)}{\left(\sum\limits_{\gamma=1}^{i-1} \gamma \right)} \frac{\left(\hat{\lambda}_i \big/ f_{c_i} + \sum\limits_{\gamma=1}^{i-1} \hat{\lambda}_\gamma \big/ f_{c_\gamma} \right)}{\left(\sum\limits_{\gamma=1}^{i} \gamma \right)} \right) \\
&= i \cdot \left(\frac{\frac{1}{2}(i-1)i}{\frac{1}{2} i(i+1)\left(i-1\right)} \bar{\hat{\lambda}}_{i-1} + \frac{1}{\frac{1}{2} i(i+1)} \hat{\lambda}_i \big/ f_{c_i} \right) \\
&= \frac{i}{i+1} \bar{\hat{\lambda}}_{i-1} + \frac{2}{i+1} \hat{\lambda}_i \big/ f_{c_i}
\end{aligned} \tag{5.35}$$

with initial value $\bar{\hat{\mu}}_1 = \hat{\mu}_1$ and $\bar{\hat{\lambda}}_1 = \hat{\lambda}_1$.

Hence, the phase distortion estimation is given by

$$\hat{\theta}_{i,k} = k \cdot \bar{\hat{\mu}}_i + f_{c_i} \cdot \bar{\hat{\lambda}}_i \tag{5.36}$$

The phase compensation for the distortion in each of the data symbols is then done based on the estimates given in Equation (5.36) using a digital domain equalizer [9].

The use of measured phase $\rho_{i,k}$ for gradient estimation is usually accurate. However, if the number of OFDM symbols in a packet is large, causing a phase wrapping effect on the measured phase, some pre-processing of $\rho_{i,k}$ is needed to combat the effect. Since the measured phase is limited to the principle region of $-\pi$ to π, a phase distortion of magnitude larger than π would be wrapped around as illustrated in Figure 5.2. Using the measured phases to find the best fit-line will hence result in getting a wrong best-fit line as shown. In Figure 5.2, note that the signal-to-noise ratio is set at very high to clearly illustrate the phase wrapping effect and error in the best fit-line.

Therefore, to combat the phase wrapping effect, the past estimates of $\theta_{i,k}$ is feed back to a pre-processing unit to adjust the measured phase before the estimate of the gradient is performed using the linear least-square curve fitting criterion. Using the past estimates, the projected maximum likelihood ranges of the measured phases are determined and the phases are shifted accordingly as shown in Figure 5.3. The adjusted phases are then used to estimate the gradient instead of the measured phases. Note that in Figure 5.3, the signal-to-noise ratio is also set at very high for illustration purpose.

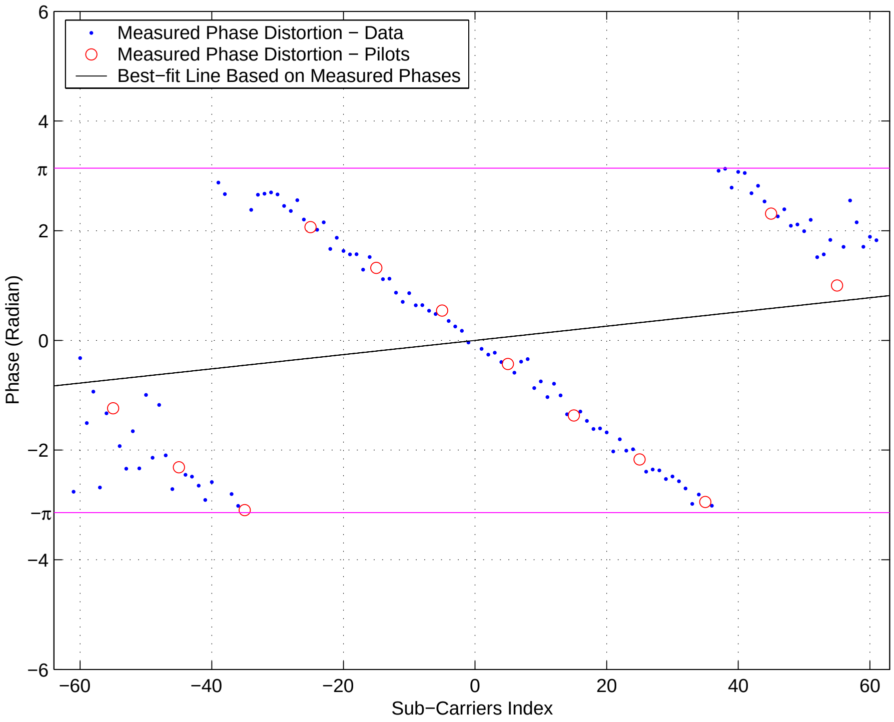

Figure 5.2: The Wrapping Effect of Measured Phase.

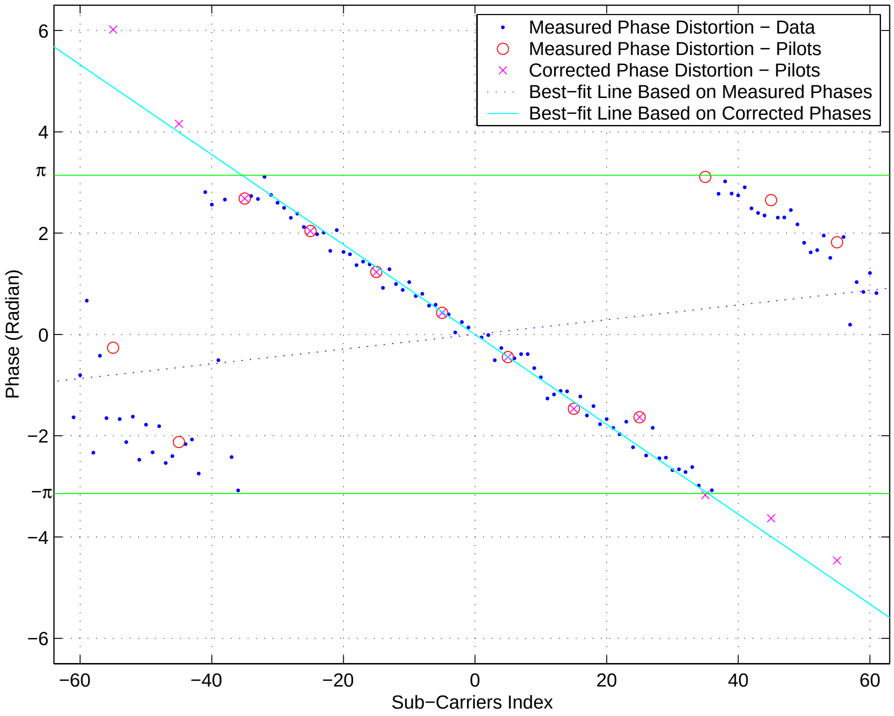

Figure 5.3: Correction for Wrapping Effect of Measured Phase.

To obtain the projected maximum likelihood range of the measured phase, we let the projected phases based on past estimates be

$$\tilde{\theta}_{i,k} = \left(\frac{i}{i-1} \bar{\hat{\mu}}_{i-1} \right) \cdot k + \left(\frac{i}{i-1} \bar{\hat{\lambda}}_{i-1} \right) \cdot f_{c_i}, \qquad k \in k_g \tag{5.37}$$

The projected maximum likelihood range, which is the most likely range which the phase distortions would be in if there had not been any phase wrapping, is defined as the range lower-bounded by $\tilde{\theta}_{i,k} - \pi$ and upper-bounded by $\tilde{\theta}_{i,k} + \pi$. The absolute difference between the projected phase and the measured phase is denoted as

$$\Delta\rho_{i,k} = \left| \tilde{\theta}_{i,k} - \tilde{\rho}_{i,k} \right| \tag{5.38}$$

Hence, the correction to the measured phase is given mathematically by

$$\xi_{\rho_{i,k}} = 2\pi \left\lfloor \frac{1}{2} \left(\left\lfloor \frac{\Delta\rho_{i,k}}{\pi} \right\rfloor + 1 \right) \right\rfloor sign\left(\tilde{\theta}_{i,k} \right) \tag{5.39}$$

where $\lfloor \bullet \rfloor$ is the floor function.

To evaluate the performance of the estimation algorithm, a simulation of a MB-OFDM UWB system using the algorithm operating in an AWGN channel is carried out. The transmission of 5000 packets each containing 1024 bytes at the rate of 200 Mbps is simulated. The normalized frequency offset between the transmitter and receiver is set at 40 ppm for the simulation and the estimated phase distortions at the receiver are recorded. In Figure 5.4, the mean-squared error (MSE) of the normalized carrier frequency offset estimated using Equation (5.21) is plotted against E_b/N_0.In Figure 5.5, the mean-squared error of the estimation of the phase distortions is plotted against the received OFDM symbol indices for various E_b/N_0.

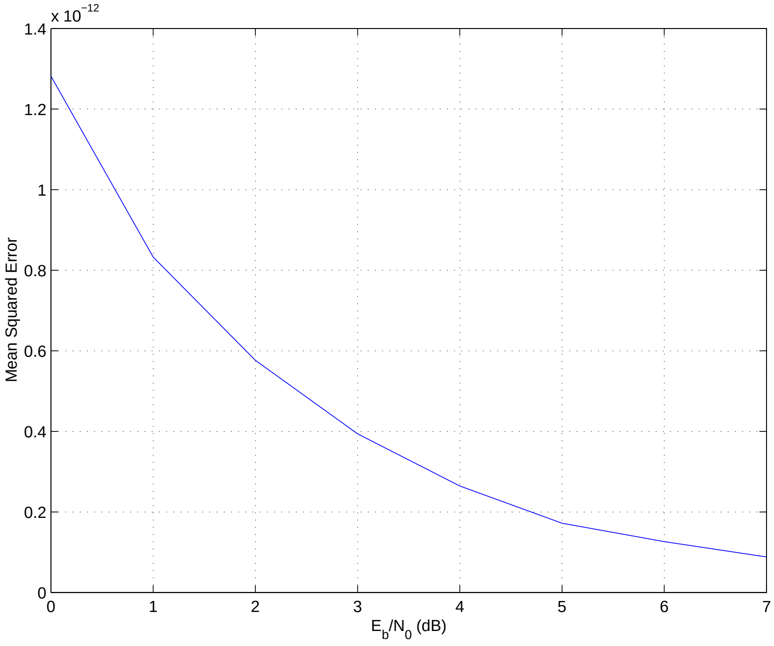

Figure 5.4: Mean-Squared Error of Estimated Normalized Carrier Frequency Offset.

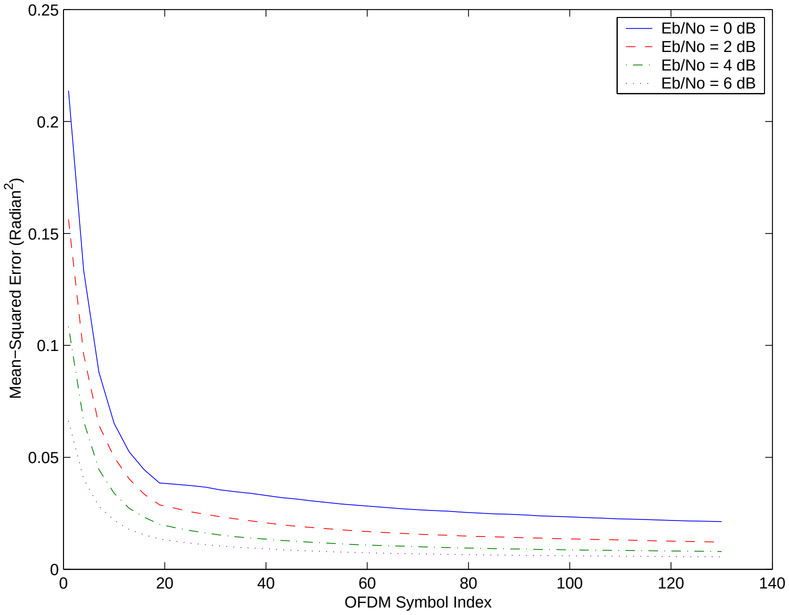

Figure 5.5: Mean-Squared Error of Estimated Phase Distortions.

From Figure 5.5, it can be seen that the use of the iterative averaging over the OFDM symbols index helps to lower the mean-squared error of the estimation significantly and the magnitude of the mean-square error actually decrease exponentially with increasing OFDM symbol index.

5.4 Performance Studies

To evaluate the performance of the joint frequency estimation and compensation algorithm in the MB-OFDM UWB system in Chapter 2, the performance of a system using the described algorithm for various data rates in different channel models are simulated and compared to that of a system without any frequency offset. The different simulation scenarios are summarized in Table 5.1. Furthermore, the performance of a MB-OFDM UWB system, which uses a memory-less frequency offset estimation algorithm, is simulated and serves as a comparison to illustrate the gain in performance with the use of the proposed iterative averaging. In essence, the system uses an algorithm which employs neither iterative averaging of estimates nor adjustments to measured phases based on past estimates. We also simulate the performance of a MB-OFDM UWB system which uses the algorithm in [25] as a comparison. In total, we simulated the performance of 4 different systems labeling them System A, B, C and D. System A is a system which experiences no frequency offset, System B is a system which uses the proposed algorithm, System C is a system which uses the memory-less estimation algorithm while System D uses the algorithm proposed in [25].

Table 5. 1: Simulation Scenarios for MB-OFDM UWB System.

Scenarios	Scenario 1	Scenario 2	Scenario 3	Scenario 4
Data Rate	480 Mbps	200 Mbps	106.7 Mbps	53.3 Mbps
Channel Model	CM1	CM2	CM4	CM4
FFT Size	128	128	128	128
Number of Data sub-carriers	100	100	100	100
FEC Code Rate	3/4	5/8	1/3	1/3
Sub-carriers Modulation	DCM	QPSK	QPSK	QPSK
Conjugate Symmetric Inputs	No	No	No	Yes
Time Spreading	No	Yes	Yes	Yes

For each of the channel models, one hundred realizations of the channel model are used as the channel conditions the system is transmitting over and it is assumed that the channel conditions remain unchanged during the transmission of a single packet of data (quasi-static). For each simulation, the normalized frequency offset between the transmitter and receiver is set at 40 ppm and the transmission of 200 packets each containing 1024 bytes of information bits in each realization of the channel models are simulated and the packet-error rate (PER) is calculated at the receiver as detailed in Chapter 2. The salient features of the simulated system are summarized in Table 5.2. and the simulation results are presented in the graphs in Figure 5.6 to Figure 5.9.

Table 5. 2: Salient Features of Simulated System

Systems	System A	System B	System C	System D
Channel Estimation	Prefect Channel Estimates	Prefect Channel Estimates	Prefect Channel Estimates	Prefect Channel Estimates
Frequency Offset	None	40 ppm	40 ppm	40 ppm
FEC	Convolutional Coding	Convolutional Coding	Convolutional Coding	Convolutional Coding

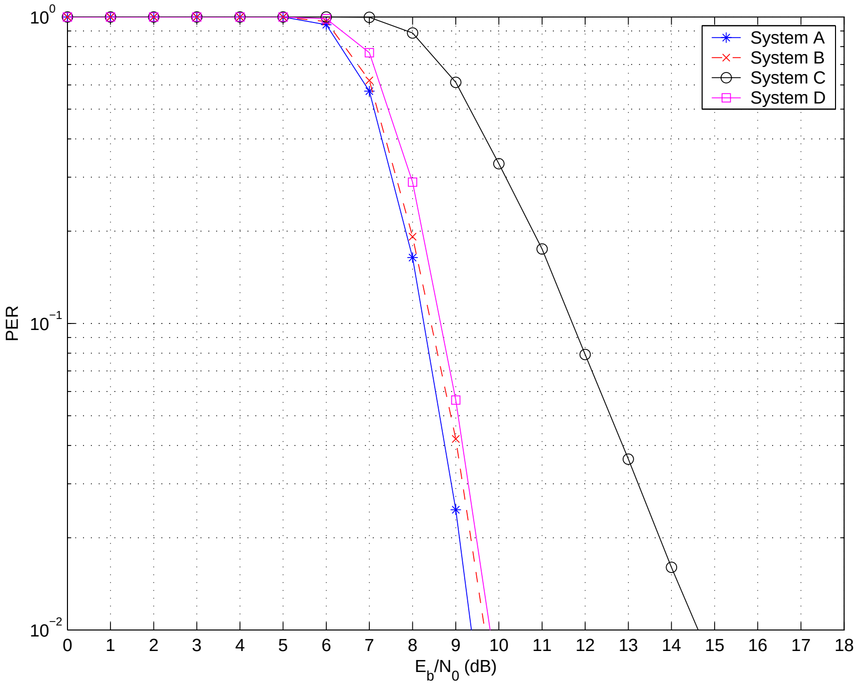

Figure 5.6: PER Performance of 480 Mbps Transmission in CM1.

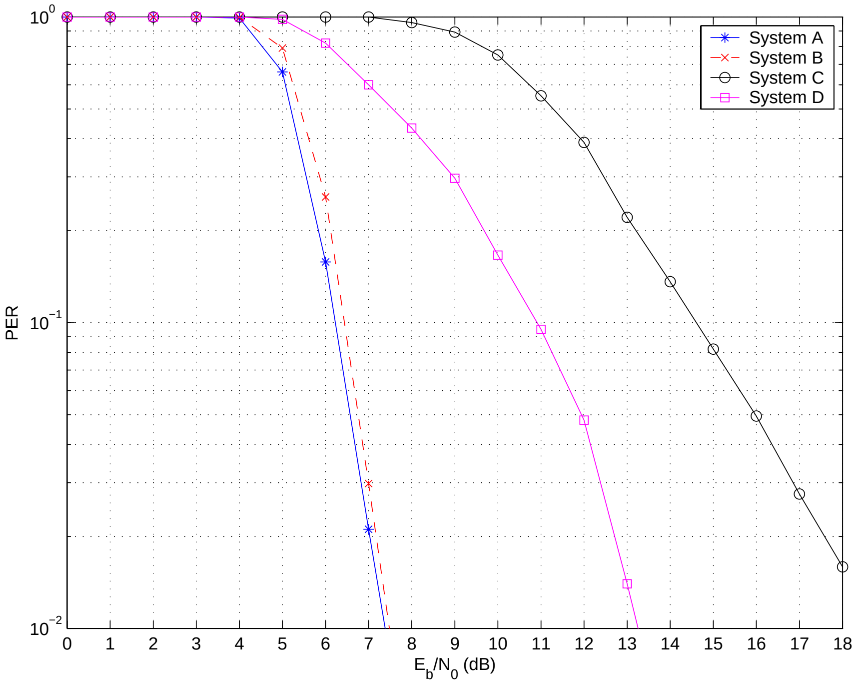

Figure 5.7: PER Performance of 200 Mbps Transmission in CM2.

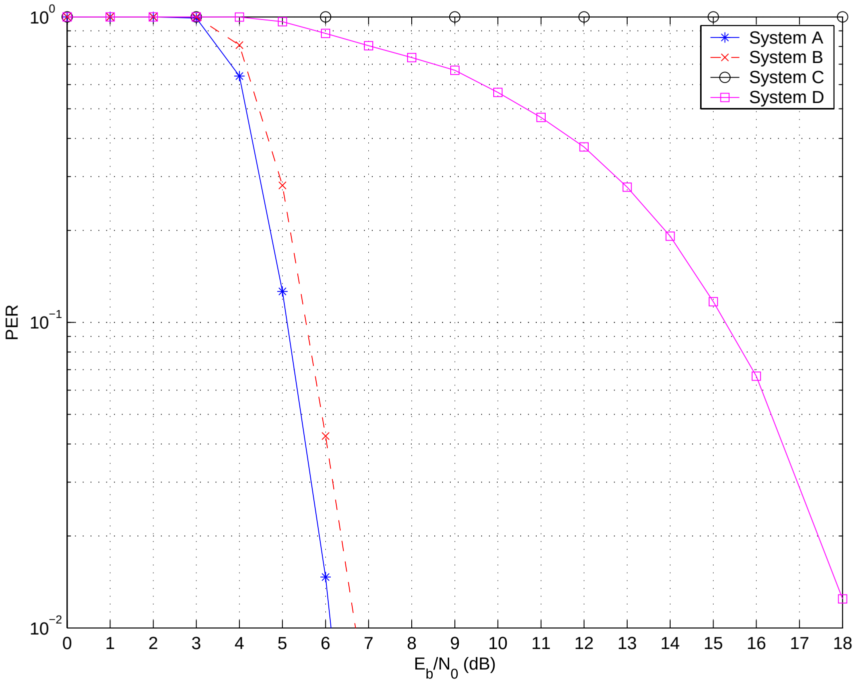

Figure 5.8: PER Performance of 106.7 Mbps Transmission in CM4.

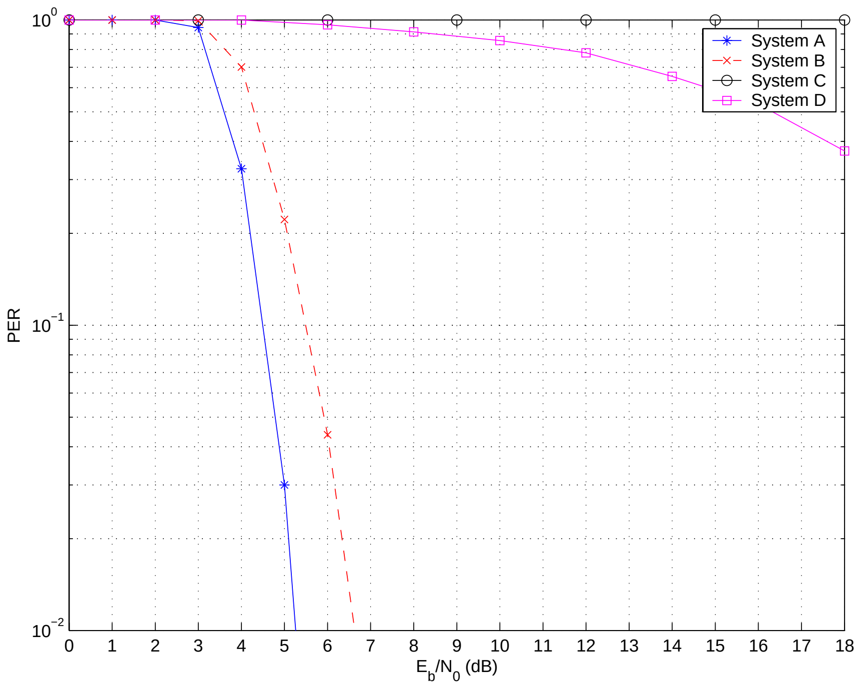

Figure 5.9: PER Performance of 53.3 Mbps Transmission in CM4.

From the figures above, it can be seen that the use of the iterative averaging over the OFDM symbols index resulted in only a very small performance loss compared to a system which experienced no frequency offset. For all 4 transmission scenarios, the loss in system performance at PER = 0.08 is less than 1 dB. Moreover, the new system, which uses iterative averaging and measured phase adjustments, performed considerably better than the system that does not and the system using the algorithm in [25].

Looking at the simulation result individually, in Figure 5.6, the new system using estimation with memory, System B, resulted in only 0.2 dB performance loss compared to the System C (system using memory-less estimation) which incurred almost 3.8 dB loss and System D (system using algorithm in [25]) which incurred loss of 0.4 dB at PER

= 0.08. For the simulation result of 200 Mbps transmission in CM2 shown in Figure 5.7, the performance gain of the new system is even more significant. The performance gain of System B compared to System C and System D is 8.0 dB and 5.0 dB respectively, partly due to the longer packets used in 200 Mbps transmission. The phase wrapping effect, which is more apparent in longer packets, resulted in significant estimation error of the phase ramp towards the end of the packet, hence limiting the performance of System C. However, the adjustment of the measured phase in System B allowed the estimated best-fit line to remain accurate even in the presence of phase wrapping. System D, which do not face the problem of phase wrapping as the estimation is done in the preamble symbols only, also perform worse than System B as the iterative averaging resulted in greater estimation accuracy.

For the simulation result of 106.7 Mbps transmission in CM4 shown in Figure 5.8, System C is totally unable to handle the phase wrapping effects and consistently give wrong estimation at the tail end of the packet resulting in packets errors in every packet transmitted. As the phase wrapping effect in the long packets is more dominant than noise, the increase in E_b/N_0 does not improve the PER performance of System C. Similarly, the PER performance of System C for 53.3 Mbps transmission in CM4 remain consistently at 1 as shown in Figure 5.9. On the other hand, System B only resulted in 0.5 dB and 0.8 dB performance loss compared to the system without frequency offset as shown in Figure 5.8 and Figure 5.9 respectively.

5.5 Conclusions

In this chapter, the effect of frequency offset between transmitter and receiver clock on MB-OFDM UWB system is discussed and conventional algorithms used to counteract the effect in OFDM system are presented in brief details. Moreover, a novel joint carrier and sampling frequency offset estimation and compensation algorithm for MB-OFDM UWB system is introduced and examined. The new algorithm is proven, through the use of extensive simulation, to perform well in the MB-OFDM UWB system and is able to keep the system performance loss due to the presence of frequency offset to a minimum.

Chapter 6

A Practical Receiver Design for MB-OFDM UWB System

In this chapter, the design of a practical MB-OFDM UWB receiver that meets the requirements of the transmitter protocols in [4] is detailed. The design considerations include symbol synchronization, channel estimation and equalization as well as frequency offset estimation and compensation. We will analyze the effect on the system performance due to non-ideal symbol synchronization and channel estimations and discuss the performance of our design algorithms. The various algorithms used in the receiver will be discussed separately but will be synthesized together to form a complete receiver design. Simulation results of the performance of the MB-OFDM UWB receiver for different transmission scenarios will also be shown and compared to that of a receiver in ideal conditions.

6.1 Symbol Synchronization

An OFDM receiver must be able to determine correctly the start of the fast Fourier transform (FFT) window of the OFDM symbols in order to successfully demodulate the transmitted signals. In other words, the receiver must be able to achieve symbol synchronization before any demodulation process. Likewise, the MB-OFDM UWB receiver for the proposed system also needs to be able to perform symbol synchronization to meet the criterion for successful data transmission. The effect of time domain synchronization error in a MB-OFDM is two-fold. Firstly, if the FFT window is offset by a large duration it will result in significant inter-symbol interference (ISI) as the receiver will perform the FFT demodulation on 2 consecutive OFDM symbols instead on a single OFDM symbol. Secondly, a small misalignment of the FFT window will result in an evolving phase shift of the frequency domain complex symbol which is disastrous for coherent sub-carrier modulation used in the proposed system [4] as the phase shift will result in a total loss of the reference phase [5]. Suppose the misalignment of the receiver's FFT window is given by mT_s , then from Fourier transform theorem, the frequency domain channel transfer function [5] due to the misalignment is given by

$$H_{\Delta}(k) = e^{-j2\pi\frac{km}{N}} \tag{6.1}$$

where T_s is the sampling interval, k is the sub-carrier index and N is the total number of FFT samples.

Symbol synchronization algorithm can be differentiated into 2 portions. The first portion, which is usually designated as coarse symbol synchronization, strives to align the FFT window within a few samples duration to avoid catastrophic ISI. The second portion, termed fine symbol synchronization, aims to negate the phase shift resulted from any small misalignment of the FTT window. In the proposed MB-OFDM UWB system, the coarse symbol synchronization can be done using the first 4 of the packet synchronization sequence preambles while the fine symbol synchronization can be done using the channel estimation sequence preambles.

For coarse symbol synchronization, the receiver used a cross-correlation summation of received data samples to determine the start of the FFT window. Note that since all time frequency codes (TFC) would transmit in Band 1 first, the coarse symbol synchronization will be done exclusively in Band 1 as the receiver cannot determine the band hopping timing without knowing the symbol FFT starting point first.

If we let the discrete baseband tapped-delay-line channel impulse model [30] of Band 1 be represented by $h_{1,i}$, $i = 0, 1, 2, \ldots, L-1$, where L is the length of channel impulse, and let the preambles sequence samples used for coarse symbol synchronization be represented by x_j, $j = 0, 1, 2, \ldots, N-1$, $N = 128$, then the noiseless discrete received samples is given by

$$r_n = \sum_{i=0}^{n} x_i h_{1,n-i} \tag{6.2}$$

The correct starting point of the FFT window is thus at $n = 0$. At the receiver, the received samples are correlated with the stored version of the known transmitted preambles, x_j. The output of the correlator, y_m can be written as

$$\begin{aligned} y_m &= \sum_{j=0}^{N-1} r_{m+j} x_j \\ &= \sum_{j=0}^{N-1} x_j \sum_{i=0}^{m+j} x_i h_{1,m+j-i} \\ &= \sum_{j=0}^{N-1} x_j^2 h_{1,m} + \sum_{j=0}^{N-1} \sum_{\substack{i=0 \\ i \neq m}}^{m+j} x_j x_{m+j-i} h_{1,i} \end{aligned} \tag{6.3}$$

Therefore, the correlator output is actually the autocorrelation function [32] of the sequence x_j multiplied by the channel tap coefficients. In Figure 6.1, the autocorrelation function $R(\tau)$ of the sequence x_j is shown.

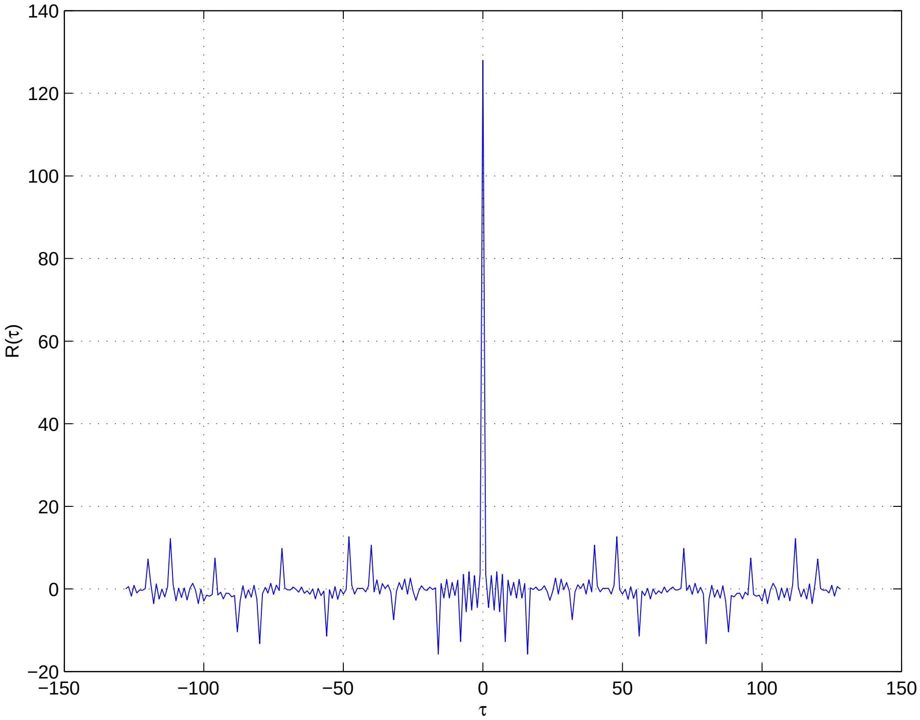

Figure 6.1: Autocorrelation Function of x_j.

As can be seen from Figure 6.1, $R(0)$ is comparatively larger than $R(\tau)\big|_{\tau\neq 0}$. Hence, we can approximate y_m by

$$y_m \approx \sum_{j=0}^{N-1} x_j^2 h_{1,m} \tag{6.4}$$

Since the channel is assumed to have finite delay duration smaller than the designed prefix of the OFDM symbol, we can determine the starting point of the FFT window as the maximum of the running summation of $|y_m|$ over P samples duration, where P is the prefix length of the OFDM symbols and is equal to 32 for the proposed system. Hence, the estimated starting point of FFT window $\hat{\kappa}$ is given by

$$\hat{\kappa} = \arg\max_{\kappa}\left\{\sum_{m=\kappa}^{\kappa+P}|y_m|\right\} \tag{6.5}$$

After achieving coarse symbol synchronization, the demodulation process can be carried out with small or negligible ISI. To achieve fine symbol synchronization, the frequency domain channel transfer function due to the misalignment, $H_{\Delta}(k)$, as given in Equation (6.1) is estimated along with the channel transfer function, $H(k)$, using the channel estimation sequence. In other words, since the received channel estimation sequence will suffer from the same FFT window misalignment as the data symbols in the same packet, the estimated channel transfer function, $\hat{H}(k)$, is actually the product of $H_{\Delta}(k)$ and $H(k)$. Hence the estimated transfer function will be used to perform fine symbol synchronization together with channel equalization.

6.2 Channel Estimation and Equalization

An advantage of OFDM system is the ease of which the received signal can be equalized to counter the effects of frequency-selective channel environment. If the receiver has the knowledge of frequency domain channel transfer function, it can perform channel equalization in the frequency domain by using a single-tap equalizer. The main issue in channel equalization in a practical system is hence to obtain a good estimate of channel transfer function. Channel estimation can be done in packet transmission by transmitting a known channel estimation preamble before actual transmission of data provided that the channel conditions and hence the channel transfer function remain relatively unchanged throughout the packet duration.

For effective channel estimation, the influence of noise on the channel transfer function estimates must be limited. A common and simple OFDM channel estimator is the least-squares (LS) channel estimators. The LS estimate is computationally appealing but has high mean-square error [33] due to noise enhancement. Another common estimator, the minimum mean-square error (MMSE) estimator, has considerably lower mean-square error but suffers from high complexity [33]. However, using the theory of optimal rank-reduction on the MMSE estimator and hence performing the channel estimation by singular value decomposition (SVD), the complexity of the estimator can be reduced significantly [34]. Both the MMSE and SVD estimator enhances the accuracy of the channel estimates in noisy environment through the exploitation of the known channel correlation and signal-to-noise ratio (SNR). Since in practice these are not known *a priori*, they will have to be estimated by the receiver. Therefore, the MMSE and SVD estimators are computationally more complex than the simple LS estimator.

For our receiver design, the channel estimation is performed using least-square-discrete-Fourier-transform-based (LS-DFT) estimator. The estimator make use of the fact that the channel impulse response given by the inverse FFT of the frequency domain channel transfer function is relatively short compared to the OFDM symbol with most of the power concentrated within the designed prefix duration. The LS-DFT estimator essentially obtained the least-square channel estimates, $\hat{H}_{LS,k}$, as per the LS estimator but in addition, the LS-DFT estimator performs a inverse discrete Fourier transform on the frequency domain channel estimates to obtain the estimates for the discrete channel impulse response, $\hat{h}_{LS,n}$. Then the coefficients of the discrete channel impulse response which is longer than the prefix is set to zero and the amended discrete channel response coefficients are converted back to the discrete frequency domain channel transfer function, $\hat{H}_{LS-DFT,k}$, using FFT as illustrated in Figure 6.2.

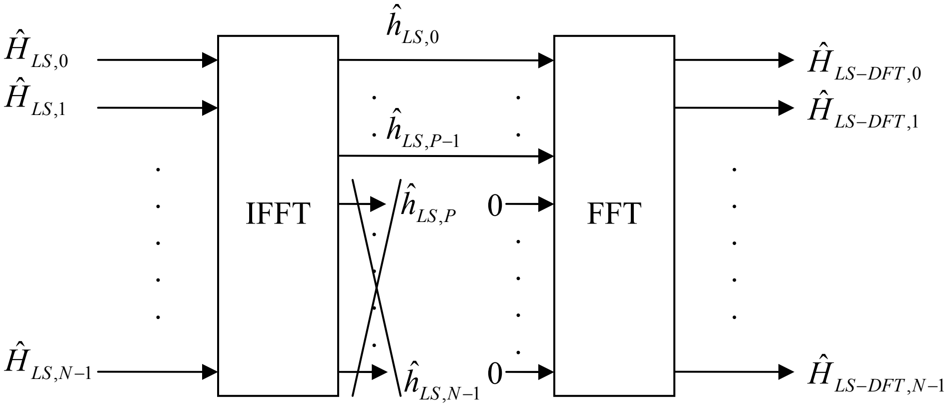

Figure 6.2: Block Diagram of LS-DFT Estimator.

The LS-DFT estimator improves the channel estimation by effectively increasing the SNR of channel estimates. However, in a practical system, doing 2 FFT operations is computationally complex and cumbersome. Hence we replace the inverse FFT and the

FFT operation by a single periodic convolution of the least-square channel estimates, $\hat{H}_{LS,k}$ and a pre-calculated sequence F_P as shown in Equation (6.7).

$$
\begin{aligned}
\hat{H}_{LS-DFT,k} &= \frac{1}{N}\sum_{m=0}^{N-1}\sum_{n=0}^{P-1}\hat{H}_{LS,m}e^{j\frac{2\pi}{N}n(m-k)} \\
&= \frac{P}{N}\hat{H}_{LS,k} + \frac{1}{N}\sum_{\substack{m=0 \\ m\neq k}}^{N-1}\hat{H}_{LS,m}\frac{1-e^{j\frac{2\pi}{N}P(m-k)}}{1-e^{j\frac{2\pi}{N}(m-k)}} \\
&= \frac{P}{N}\hat{H}_{LS,k} + \frac{1}{N}\sum_{\substack{m=0 \\ m\neq k}}^{N-1}\hat{H}_{LS,m}\frac{\sin\left(\frac{\pi P(k-m)}{N}\right)}{\sin\left(\frac{\pi(k-m)}{N}\right)}e^{-j2\pi\frac{(P-1)}{N}(k-m)} \qquad (6.6) \\
&= \sum_{m=0}^{N-1}\hat{H}_{LS,m}F_{P,k-m} \\
&= \hat{H}_{LS,m} * F_{P,m}
\end{aligned}
$$

where

$$
F_{P,m} = \begin{cases} \dfrac{P}{N}, & m = 0 \\ \dfrac{\sin\left(\frac{\pi P m}{N}\right)}{N\sin\left(\frac{\pi m}{N}\right)}e^{-j2\pi\frac{(P-1)}{N}m}, & m = 1, 2, ..., N\text{-}1 \end{cases} \qquad (6.7)
$$

The LS-DFT channel estimates obtained are used to equalize the data symbols in the frequency domain using a single-tap maximal ratio combining (MRC) equalizer. MRC equalizer is chosen because of the simplicity in implementation and its ability to retain the information of the relative SNR of each individual sub-carrier which can be used by the Viterbi decoder to improve the error-correction accuracy.

6.3 Frequency Offset Estimation and Compensation

The novel frequency offset estimation and compensation described in Chapter 5 is used in the overall receiver design. The main difference is that since the channel estimation preambles also suffer from the frequency offset phase distortion, the channel estimates used for equalization will be able to correct for part of the phase distortion specifically the distortions labeled as φ_c and $f_{c_i} \cdot \varphi_d$ in Chapter 5. Note that the sampling and residual carrier frequency offset estimation start after the channel estimates are obtained.

6.4 Practical Receiver Design

In Figure 6.3, the block diagram of the overall practical receiver design is shown. Note that since the transmitter used zero prefix instead of cyclic prefix, the receiver need to perform an overlap and add operation on the received samples after locking on to the start of the FFT window. If the start of the FFT window is at the received samples r_0, the input samples r_n' to the FFT is then calculated using the overlap and add method as

$$r_n' = \begin{cases} r_n + r_{n+N}, & n = 0,1,\ldots,P-1 \\ r_n, & n = P, P+1,\ldots,N-1 \end{cases} \tag{6.8}$$

Also, for the transmission rates equal or higher than 320 Mbps when dual-carrier modulation (DCM) is used instead of QPSK, the log-likelihood ratio of each bit is passed to the Viterbi decoder for decoding. If each group of 200 bits transmitted in an OFDM symbol is denoted as $b_0, b_1, \ldots, b_{199}$, then with reference to Chapter 2, the log-likelihood ratio at the receiver is given by

$$LLR(b_n) = \begin{cases} \dfrac{2(syr + 2dyr)}{\sigma^2\sqrt{10}} + \log\left\{ \dfrac{1 + e^{\left(\frac{1}{\sigma^2}\left[C - \frac{3}{\sqrt{10}}dyr + \frac{1}{\sqrt{10}}syr\right]\right)}}{1 + e^{\left(\frac{1}{\sigma^2}\left[C + \frac{3}{\sqrt{10}}dyr - \frac{1}{\sqrt{10}}syr\right]\right)}} \right\}, n = 0,2,\ldots,48,100,\ldots,148 \\ \dfrac{2(syr + 2dyr)}{\sigma^2\sqrt{10}} + \log\left\{ \dfrac{1 + e^{\left(\frac{1}{\sigma^2}\left[C - \frac{3}{\sqrt{10}}syr - \frac{1}{\sqrt{10}}dyr\right]\right)}}{1 + e^{\left(\frac{1}{\sigma^2}\left[C + \frac{3}{\sqrt{10}}syr + \frac{1}{\sqrt{10}}dyr\right]\right)}} \right\}, n = 1,3,\ldots,49,101,\ldots,149 \\ \dfrac{2(syi + 2dyi)}{\sigma^2\sqrt{10}} + \log\left\{ \dfrac{1 + e^{\left(\frac{1}{\sigma^2}\left[C - \frac{3}{\sqrt{10}}dyi + \frac{1}{\sqrt{10}}syi\right]\right)}}{1 + e^{\left(\frac{1}{\sigma^2}\left[C + \frac{3}{\sqrt{10}}dyi - \frac{1}{\sqrt{10}}syi\right]\right)}} \right\}, n = 50,52,\ldots,98,150,\ldots,198 \\ \dfrac{2(syi + 2dyi)}{\sigma^2\sqrt{10}} + \log\left\{ \dfrac{1 + e^{\left(\frac{1}{\sigma^2}\left[C - \frac{3}{\sqrt{10}}syi - \frac{1}{\sqrt{10}}dyi\right]\right)}}{1 + e^{\left(\frac{1}{\sigma^2}\left[C + \frac{3}{\sqrt{10}}syi + \frac{1}{\sqrt{10}}dyi\right]\right)}} \right\}, n = 51,53,\ldots,99,151,\ldots,199 \end{cases} \quad (6.9)$$

where

$$C = \frac{2}{5}\left(\left| \hat{H}_{LS-DFT,2m} \right|^2 - \left| \hat{H}_{LS-DFT,2m+1} \right|^2 \right), m = 0,1,\ldots,49 \quad (6.10)$$

and

$$syr = \mathrm{Re}[E_{2m}] + \mathrm{Re}[E_{2m+1}] \quad (6.11)$$

$$dyr = \mathrm{Re}[E_{2m}] - \mathrm{Re}[E_{2m+1}] \quad (6.12)$$

$$syi = \mathrm{Im}[E_{2m}] + \mathrm{Im}[E_{2m+1}] \quad (6.13)$$

$$dyi = \mathrm{Im}[E_{2m}] - \mathrm{Im}[E_{2m+1}] \quad (6.14)$$

where E_n is the equalized received data for the n^{th} sub-carrier.

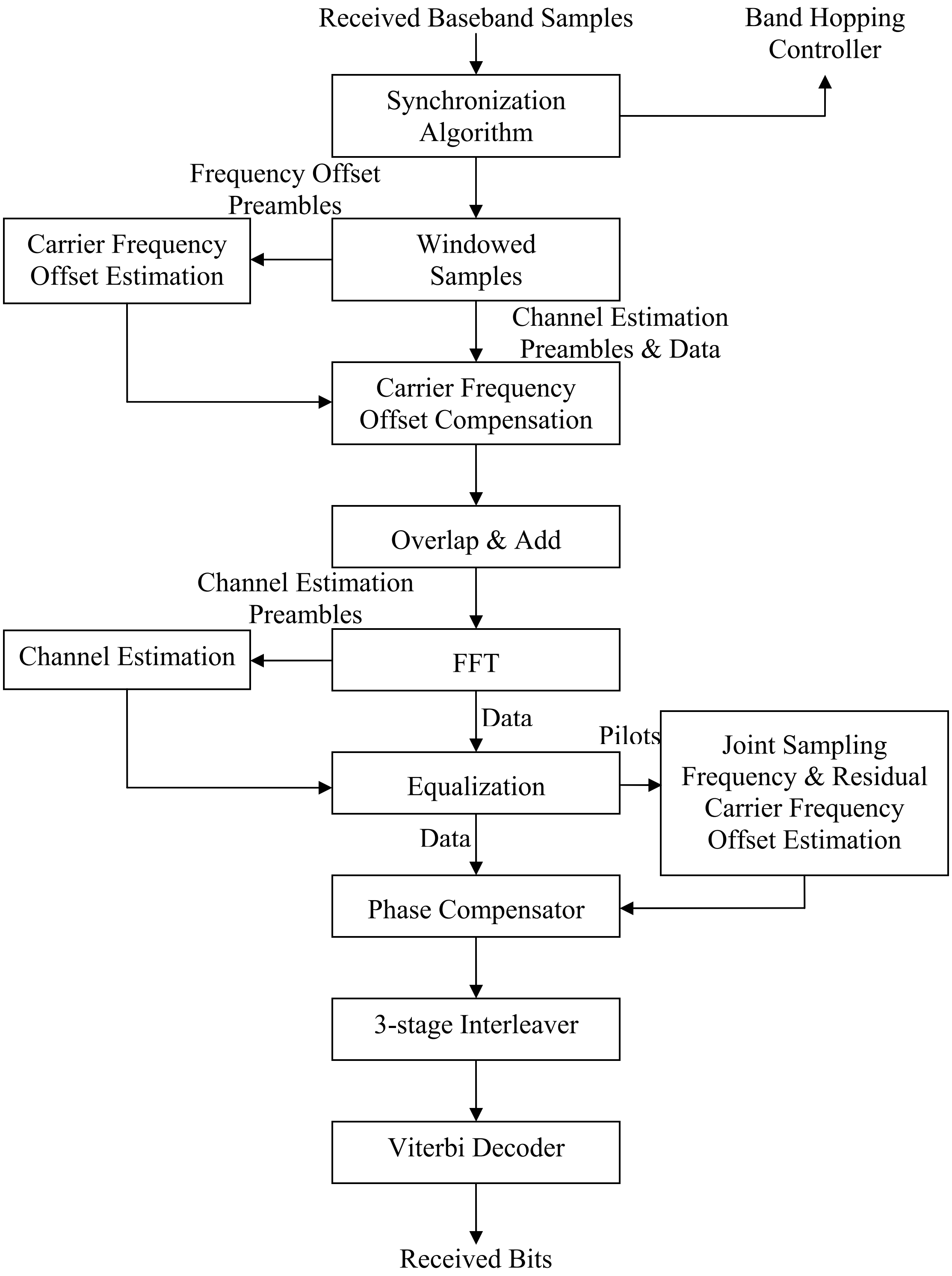

Figure 6.3: Block Diagram of Receiver Design.

6.5 Performance Studies

To evaluate the performance of the receiver design, the performance of the receiver is simulated and compare to that of a receiver in ideal condition. The ideal condition is defined as the receiver having ideal synchronization and complete knowledge of the channel transfer function. Moreover, the receiver experiences no frequency offset and hence requires no offset estimation and compensation. The different simulation scenarios are summarized in Table 6.1.

Table 6.1: Simulation Scenarios for MB-OFDM UWB System.

Scenarios	Scenario 1	Scenario 2	Scenario 3	Scenario 4
Data Rate	480 Mbps	200 Mbps	106.7 Mbps	53.3 Mbps
Channel Model	CM1	CM2	CM4	CM4
FFT Size	128	128	128	128
Number of Data sub-carriers	100	100	100	100
FEC Code Rate	3/4	5/8	1/3	1/3
Sub-carriers Modulation	DCM	QPSK	QPSK	QPSK
Conjugate Symmetric Inputs	No	No	No	Yes
Time Spreading	No	Yes	Yes	Yes

For each of the channel models, one hundred realizations of the channel model are used as the channel conditions the system is transmitting over and it is assumed that the channel conditions remain unchanged during the transmission of a single packet of data (quasi-static). For the simulation of the practical receiver, the normalized frequency offset between the transmitter and receiver is set at 40 ppm and the transmission of 50 packets each containing 1024 bytes of information bits in each realization of the channel models are simulated and the packet-error rate (PER) is calculated at the receiver as detailed in Chapter 2. The simulation results are presented in the graphs in Figure 6.4 to Figure 6.7.

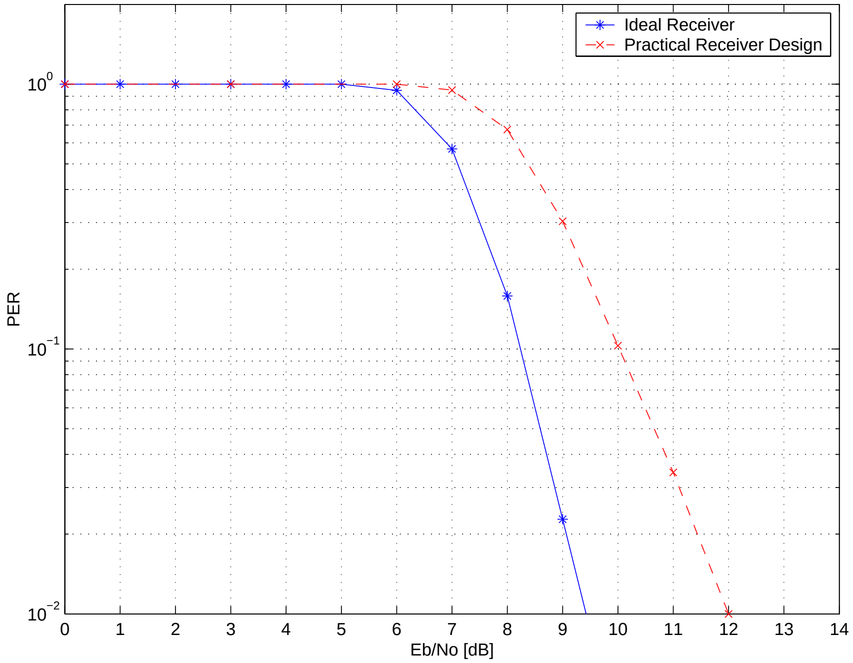

Figure 6.4: PER Performance of 480 Mbps Transmission in CM1.

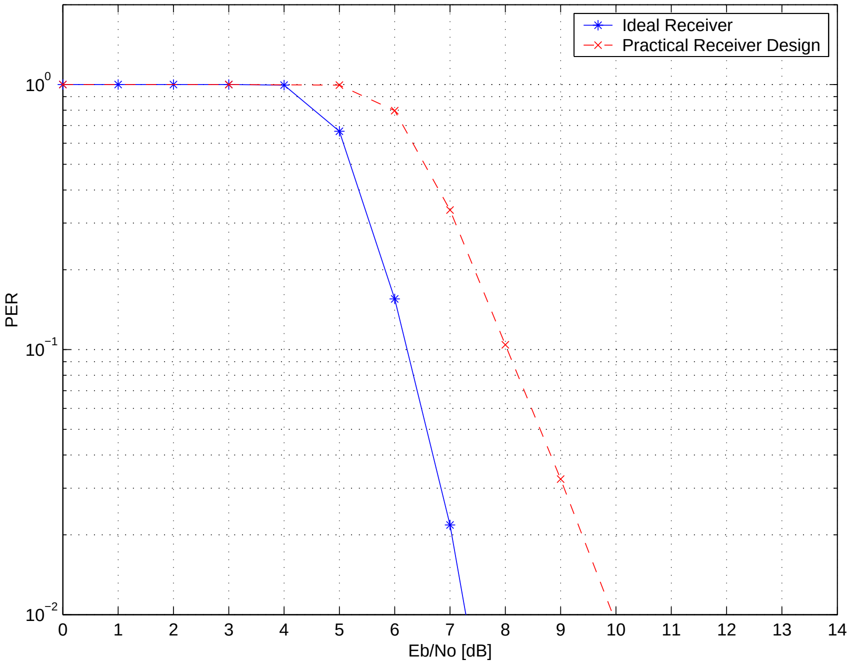

Figure 6.5: PER Performance of 200 Mbps Transmission in CM2.

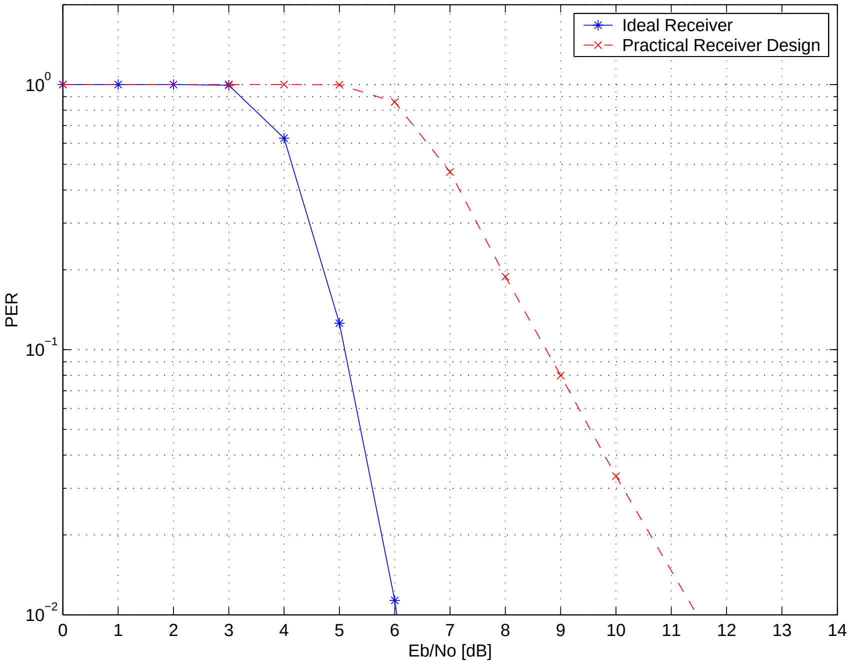

Figure 6.6: PER Performance of 106.7 Mbps Transmission in CM4.

From the simulation results shown in the figures above, the practical receiver design detailed in this chapter compared favorably to the ideal receiver. The practical receiver resulted in less than 2 dB performance degradation when compared to the ideal receiver for transmission in CM1 and CM2 with the performance indicator as PER = 0.08. For 480 Mbps transmission in CM1 as shown in Figure 6.4, the practical receiver only resulted in 1.8 dB performance degradation while for 200 Mbps transmission in CM2 as shown in Figure 6.5, the practical receiver's performance degradation is only 2.0 dB. In Figure 6.6, the degradation in performance for 106.7 Mbps transmission in CM4 is more significant at 3.8 dB for PER = 0.08. The degradation is largely due to the loss in the accuracy of the channel estimates. The comparatively longer delay spread characteristic of CM4 resulted in the inability of the LS-DFT channel estimator to reduce the SNR of the channel estimates significantly through truncation of discrete channel impulse response.

6.6 Conclusions

In this chapter, a complete practical receiver design incorporating different sub-systems like symbol synchronization system, channel estimation system and frequency offset estimation and compensation system are presented. The performance of the receiver design is simulated and compared to the performance of the ideal receiver. Through the simulation results, it can be seen that the designed practical receiver performance is only slightly worse then the ideal receiver performance in all channel environments. The receiver design is also robust to symbol synchronization offset and frequency offset between the transmitter and receiver.

Chapter 7

Conclusions and Future Works

In this chapter, the conclusions about the research on the design of a practical MB-OFDM UWB receiver carried out and detailed in this thesis are summarized and highlighted. Future works that can be carried out pertaining to the research on receiver design and ultra wide-band transmission as a whole are also mentioned.

7.1 Thesis Conclusions

In this thesis, we examine the design of a practical receiver on the performance of the ultra-wideband (UWB) multi-band orthogonal frequency division multiplexing (MB-OFDM) system as well as the effects of the use of low-density parity-check (LDPC) as the error correcting codes in the same system. Also, a novel joint carrier and sampling frequency offset estimation and compensation technique is introduced as part of the practical receiver design.

In Chapter 3, a simplified LDPC code is used as the error-correcting codes in place of the proposed convolutional codes. The use of LDPC codes eliminates the need for bits interleaver due to its capabilities of burst errors protection. More importantly, the performance simulation shows that the performance of a high-rate MB-OFDM UWB system can be improved by 2 dB to 4 dB through the use of LDPC codes. Also, it is significant that the use of LDPC codes makes the system more robust to channel degradation due to the superior error correction ability of LDPC codes as illustrated by the simulation results.

In Chapter 4, a direct spreading with chip interleaving scheme is applied to MB-OFDM UWB system and found to perform exceedingly well especially in frequency-selective channel with small coherence bandwidth. Simulation results show that by using a simplified form of maximum likelihood detection at the receiver, the receiver complexity can be significantly reduced while maintaining the same performance gain.

In Chapter 5 and Chapter 6, the detailed algorithms used for symbol synchronization, channel estimation and frequency offset estimation for the practical receiver design are described. System performance simulation of a MB-OFDM UWB system using the designed receiver is then carried out. From the system simulation results, the designed receiver is shown to perform well, showing only 1 dB to 4 dB energy losses when compared with an ideal receiver. Moreover in Chapter 5, we show that the proposed novel frequency offset estimation algorithm is able to achieve very high level of accuracy even at extremely low E_b/N_0. Therefore, the performance loss due to the frequency offset distortion is kept at very small level.

Most of the performance loss of the designed receiver can be attributed to the channel estimator. As we used a LS-DFT channel estimator, the accuracy of the estimator is dependent on the channel delay spread statistics. When the channel delay is significantly more than the designed zero prefix length of the OFDM symbol, the accuracy of the estimator decreased. From the simulation results, the performance of the system in CM4, which has a significantly longer delay spread, is much worse compared to the performance of the system in CM1 or CM2 which have comparatively much shorter delay spread.

7.2 Future Works

As mentioned above, the performance of the channel estimator is unsatisfactory in channel with longer channel delay spread. Therefore, a search for a better channel estimator technique in CM3 and CM4 can be conducted. Ideally, the algorithm must be robust to channel statistics and also simple in terms of implementation. Also, the use of maximum likelihood (ML) decoding for dual carrier modulation (DCM) required a good signal-to-noise ratio (SNR) estimator which is assumed to be prefect in the preceding simulations. The design of the SNR estimator would need to be taken into consideration for future design.

Regarding the use of LDPC codes in MB-OFDM UWB system, future research efforts can be put into the investigations of the use of irregular codes that can offer protection priorities. In other words, instead having similar error protection for each coded bits, the coded information bits using systematic encoding are given better protection than the parity-check bits.

Appendix A

Preambles for MB-OFDM UWB System

The packet and frame synchronization sequences for each time frequency code (TFC) shown in Table A.1 are defined based on the preamble cover sequence shown in Table A.2 and the time domain synchronization sequences shown in Table A.3 through Table A.7. Each period of the time domain synchronization sequence, $p_t(n)$, is a 165-sample sequence constructed by appending a zero pad interval of 37 “zero samples” to the 128 length sequence chosen from Table A.3 through Table A.7. Next, the appropriate cover sequence $p_c(n)$ (of length 24) corresponding to the TFC in use is chosen based on Table A.1 from Table A.2, and the combined packet and frame synchronization portion of the PLCP preamble are generated as the Kronecker product of the two sequences, $p(n) = p_c(n) \otimes p_t(n)$. This is equivalent to multiplying the chosen synchronization sequence with each element of the cover sequence, and concatenating the resulting 24 sequences to form the combined packet and frame synchronization sequence. The channel estimation sequence in frequency domain is given in Table A.8.

Table A.8: Time Frequency Codes and Associated Preamble Patterns.

TFC Number	Preamble Pattern Number	Cover Sequence Number
1	1	1
2	2	1
3	3	2
4	4	2
5	5	3
6	5	3
7	5	3

Table A.9: Preamble Cover Sequence.

Sample index	Sequence index		
	(TFCs 1,2)	(TFCs 3,4)	(TFCs 5,6,7)
0	1	1	-1
1	1	1	-1
2	1	1	-1
3	1	1	-1
4	1	1	-1
5	1	1	-1
6	1	1	-1
7	1	1	1
8	1	1	-1
9	1	1	-1
10	1	1	1
11	1	1	-1
12	1	1	-1
13	1	1	1
14	1	1	-1
15	1	1	-1
16	1	1	1
17	1	1	-1
18	1	1	-1
19	1	-1	1
20	1	1	-1
21	-1	-1	1
22	-1	1	1
23	-1	-1	1

Table A.10: Time-domain Packet Synchronization Sequence for Preamble Pattern 1.

Index	Value	Index	Value	Index	Value	Index	Value
C_0	0.6564	C_{32}	-0.0844	C_{64}	-0.2095	C_{96}	0.4232
C_1	-1.3671	C_{33}	1.1974	C_{65}	1.1640	C_{97}	-1.2684
C_2	-0.9958	C_{34}	1.2261	C_{66}	1.2334	C_{98}	-1.8151
C_3	-1.3981	C_{35}	1.4401	C_{67}	1.5338	C_{99}	-1.4829
C_4	0.8481	C_{36}	-0.5988	C_{68}	-0.8844	C_{100}	1.0302
C_5	1.0892	C_{37}	-0.4675	C_{69}	-0.3857	C_{101}	0.9419
C_6	-0.8621	C_{38}	0.8520	C_{70}	0.7730	C_{102}	-1.1472
C_7	1.1512	C_{39}	-0.8922	C_{71}	-0.9754	C_{103}	1.4858
C_8	0.9602	C_{40}	-0.5603	C_{72}	-0.2315	C_{104}	-0.6794
C_9	-1.3581	C_{41}	1.1886	C_{73}	0.5579	C_{105}	0.9573
C_{10}	-0.8354	C_{42}	1.1128	C_{74}	0.4035	C_{106}	1.0807
C_{11}	-1.3249	C_{43}	1.0833	C_{75}	0.4248	C_{107}	1.1445
C_{12}	1.0964	C_{44}	-0.9073	C_{76}	-0.3359	C_{108}	-1.2312
C_{13}	1.3334	C_{45}	-1.6227	C_{77}	-0.9914	C_{109}	-0.6643
C_{14}	-0.7378	C_{46}	1.0013	C_{78}	0.5975	C_{110}	0.3836
C_{15}	1.3565	C_{47}	-1.6067	C_{79}	-0.8408	C_{111}	-1.1482
C_{16}	0.9361	C_{48}	0.3360	C_{80}	0.3587	C_{112}	-0.0353
C_{17}	-0.8212	C_{49}	-1.3136	C_{81}	-0.9604	C_{113}	-0.6747
C_{18}	-0.2662	C_{50}	-1.4447	C_{82}	-1.0002	C_{114}	-1.1653
C_{19}	-0.6866	C_{51}	-1.7238	C_{83}	-1.1636	C_{115}	-0.8896
C_{20}	0.8437	C_{52}	1.0287	C_{84}	0.9590	C_{116}	0.2414
C_{21}	1.1237	C_{53}	0.6100	C_{85}	0.7137	C_{117}	0.1160
C_{22}	-0.3265	C_{54}	-0.9237	C_{86}	-0.6776	C_{118}	-0.6987
C_{23}	1.0511	C_{55}	1.2618	C_{87}	0.9824	C_{119}	0.4781
C_{24}	0.7927	C_{56}	0.5974	C_{88}	-0.5454	C_{120}	0.1821
C_{25}	-0.3363	C_{57}	-1.0976	C_{89}	1.1022	C_{121}	-1.0672
C_{26}	-0.1342	C_{58}	-0.9776	C_{90}	1.6485	C_{122}	-0.9676
C_{27}	-0.1546	C_{59}	-0.9982	C_{91}	1.3307	C_{123}	-1.2321
C_{28}	0.6955	C_{60}	0.8967	C_{92}	-1.2852	C_{124}	0.5003
C_{29}	1.0608	C_{61}	1.7640	C_{93}	-1.2659	C_{125}	0.7419
C_{30}	-0.1600	C_{62}	-1.0211	C_{94}	0.9435	C_{126}	-0.8934
C_{31}	0.9442	C_{63}	1.6913	C_{95}	-1.6809	C_{127}	0.8391

Table A.11: Time-domain Packet Synchronization Sequence for Preamble Pattern 2.

Index	Value	Index	Value	Index	Value	Index	Value
C_{0}	0.9679	C_{32}	-1.2905	C_{64}	1.5280	C_{96}	0.5193
C_{1}	-1.0186	C_{33}	1.1040	C_{65}	-0.9193	C_{97}	-0.3439
C_{2}	0.4883	C_{34}	-1.2408	C_{66}	1.1246	C_{98}	0.1428
C_{3}	0.5432	C_{35}	-0.8062	C_{67}	1.2622	C_{99}	0.6251
C_{4}	-1.4702	C_{36}	1.5425	C_{68}	-1.4406	C_{100}	-1.0468
C_{5}	-1.4507	C_{37}	1.0955	C_{69}	-1.4929	C_{101}	-0.5798
C_{6}	-1.1752	C_{38}	1.4284	C_{70}	-1.1508	C_{102}	-0.8237
C_{7}	-0.0730	C_{39}	-0.4593	C_{71}	0.4126	C_{103}	0.2667
C_{8}	-1.2445	C_{40}	-1.0408	C_{72}	-1.0462	C_{104}	-0.9564
C_{9}	0.3143	C_{41}	1.0542	C_{73}	0.7232	C_{105}	0.6016
C_{10}	-1.3951	C_{42}	-0.4446	C_{74}	-1.1574	C_{106}	-0.9964
C_{11}	-0.9694	C_{43}	-0.7929	C_{75}	-0.7102	C_{107}	-0.3541
C_{12}	0.4563	C_{44}	1.6733	C_{76}	0.8502	C_{108}	0.3965
C_{13}	0.3073	C_{45}	1.7568	C_{77}	0.6260	C_{109}	0.5201
C_{14}	0.6408	C_{46}	1.3273	C_{78}	0.9530	C_{110}	0.4733
C_{15}	-0.9798	C_{47}	-0.2465	C_{79}	-0.4971	C_{111}	-0.2362
C_{16}	-1.4116	C_{48}	1.6850	C_{80}	-0.8633	C_{112}	-0.6892
C_{17}	0.6038	C_{49}	-0.7091	C_{81}	0.6910	C_{113}	0.4787
C_{18}	-1.3860	C_{50}	1.1396	C_{82}	-0.3639	C_{114}	-0.2605
C_{19}	-1.0888	C_{51}	1.5114	C_{83}	-0.8874	C_{115}	-0.5887
C_{20}	1.1036	C_{52}	-1.4343	C_{84}	1.5311	C_{116}	0.9411
C_{21}	0.7067	C_{53}	-1.5005	C_{85}	1.1546	C_{117}	0.7364
C_{22}	1.1667	C_{54}	-1.2572	C_{86}	1.1935	C_{118}	0.6714
C_{23}	-1.0225	C_{55}	0.8274	C_{87}	-0.2930	C_{119}	-0.1746
C_{24}	-1.2471	C_{56}	-1.5140	C_{88}	1.3285	C_{120}	1.1776
C_{25}	0.7788	C_{57}	1.1421	C_{89}	-0.7231	C_{121}	-0.8803
C_{26}	-1.2716	C_{58}	-1.0135	C_{90}	1.2832	C_{122}	1.2542
C_{27}	-0.8745	C_{59}	-1.0657	C_{91}	0.7878	C_{123}	0.5111
C_{28}	1.2175	C_{60}	1.4073	C_{92}	-0.8095	C_{124}	-0.8209
C_{29}	0.8419	C_{61}	1.8196	C_{93}	-0.7463	C_{125}	-0.8975
C_{30}	1.2881	C_{62}	1.1679	C_{94}	-0.8973	C_{126}	-0.9091
C_{31}	-0.8210	C_{63}	-0.4131	C_{95}	0.5560	C_{127}	0.2562

Table A.12: Time-domain Packet Synchronization Sequence for Preamble Pattern 3.

Index	Value	Index	Value	Index	Value	Index	Value
C_0	0.4047	C_{32}	-0.9671	C_{64}	-0.7298	C_{96}	0.2424
C_1	0.5799	C_{33}	-0.9819	C_{65}	-0.9662	C_{97}	0.5703
C_2	-0.3407	C_{34}	0.7980	C_{66}	0.9694	C_{98}	-0.6381
C_3	0.4343	C_{35}	-0.8158	C_{67}	-0.8053	C_{99}	0.7861
C_4	0.0973	C_{36}	-0.9188	C_{68}	-0.9052	C_{100}	0.9175
C_5	-0.7637	C_{37}	1.5146	C_{69}	1.5933	C_{101}	-0.4595
C_6	-0.6181	C_{38}	0.8138	C_{70}	0.8418	C_{102}	-0.2201
C_7	-0.6539	C_{39}	1.3773	C_{71}	1.5363	C_{103}	-0.7755
C_8	0.3768	C_{40}	0.2108	C_{72}	0.3085	C_{104}	-0.2965
C_9	0.7241	C_{41}	0.9245	C_{73}	1.3016	C_{105}	-1.1220
C_{10}	-1.2095	C_{42}	-1.2138	C_{74}	-1.5546	C_{106}	1.7152
C_{11}	0.6027	C_{43}	1.1252	C_{75}	1.5347	C_{107}	-1.2756
C_{12}	0.4587	C_{44}	0.9663	C_{76}	1.0935	C_{108}	-0.7731
C_{13}	-1.3879	C_{45}	-0.8418	C_{77}	-0.8978	C_{109}	1.0724
C_{14}	-1.0592	C_{46}	-0.6811	C_{78}	-0.9712	C_{110}	1.1733
C_{15}	-1.4052	C_{47}	-1.3003	C_{79}	-1.3763	C_{111}	1.4711
C_{16}	-0.8439	C_{48}	-0.3397	C_{80}	-0.6360	C_{112}	0.4881
C_{17}	-1.5992	C_{49}	-1.1051	C_{81}	-1.2947	C_{113}	0.7528
C_{18}	1.1975	C_{50}	1.2400	C_{82}	1.6436	C_{114}	-0.6417
C_{19}	-1.9525	C_{51}	-1.3975	C_{83}	-1.6564	C_{115}	1.0363
C_{20}	-1.5141	C_{52}	-0.7467	C_{84}	-1.1981	C_{116}	0.8002
C_{21}	0.7219	C_{53}	0.2706	C_{85}	0.8719	C_{117}	-0.0077
C_{22}	0.6982	C_{54}	0.7294	C_{86}	0.9992	C_{118}	-0.2336
C_{23}	1.2924	C_{55}	0.7444	C_{87}	1.4872	C_{119}	-0.4653
C_{24}	-0.9460	C_{56}	-0.3970	C_{88}	-0.4586	C_{120}	0.6862
C_{25}	-1.2407	C_{57}	-1.0718	C_{89}	-0.8404	C_{121}	1.2716
C_{26}	0.4572	C_{58}	0.6646	C_{90}	0.6982	C_{122}	-0.8880
C_{27}	-1.2151	C_{59}	-1.1037	C_{91}	-0.7959	C_{123}	1.4011
C_{28}	-0.9869	C_{60}	-0.5716	C_{92}	-0.5692	C_{124}	0.9531
C_{29}	1.2792	C_{61}	0.9001	C_{93}	1.3528	C_{125}	-1.1210
C_{30}	0.6882	C_{62}	0.7317	C_{94}	0.9536	C_{126}	-0.9489
C_{31}	1.2586	C_{63}	0.9846	C_{95}	1.1784	C_{127}	-1.2566

Table A.13: Time-domain Packet Synchronization Sequence for Preamble Pattern 4.

Index	Value	Index	Value	Index	Value	Index	Value
C_0	1.1549	C_{32}	-1.2385	C_{64}	1.3095	C_{96}	-1.0094
C_1	1.0079	C_{33}	-0.7883	C_{65}	0.6675	C_{97}	-0.7598
C_2	0.7356	C_{34}	-0.7954	C_{66}	1.2587	C_{98}	-1.0786
C_3	-0.7434	C_{35}	1.0874	C_{67}	-0.9993	C_{99}	0.6699
C_4	-1.3930	C_{36}	1.1491	C_{68}	-1.0052	C_{100}	0.9813
C_5	1.2818	C_{37}	-1.4780	C_{69}	0.6601	C_{101}	-0.5563
C_6	-1.1033	C_{38}	0.8870	C_{70}	-1.0228	C_{102}	1.0548
C_7	-0.2523	C_{39}	0.4694	C_{71}	-0.7489	C_{103}	0.8925
C_8	-0.7905	C_{40}	1.5066	C_{72}	0.5086	C_{104}	-1.3656
C_9	-0.4261	C_{41}	1.1266	C_{73}	0.1563	C_{105}	-0.8472
C_{10}	-0.9390	C_{42}	0.9935	C_{74}	0.0673	C_{106}	-1.3110
C_{11}	0.4345	C_{43}	-1.2462	C_{75}	-0.8375	C_{107}	1.1897
C_{12}	0.4433	C_{44}	-1.7869	C_{76}	-1.0746	C_{108}	1.5127
C_{13}	-0.3076	C_{45}	1.7462	C_{77}	0.4454	C_{109}	-0.7474
C_{14}	0.5644	C_{46}	-1.4881	C_{78}	-0.7831	C_{110}	1.4678
C_{15}	0.2571	C_{47}	-0.4090	C_{79}	-0.3623	C_{111}	1.0295
C_{16}	-1.0030	C_{48}	-1.4694	C_{80}	-1.3658	C_{112}	-0.9210
C_{17}	-0.7820	C_{49}	-0.7923	C_{81}	-1.0854	C_{113}	-0.4784
C_{18}	-0.4064	C_{50}	-1.4607	C_{82}	-1.4923	C_{114}	-0.5022
C_{19}	0.9035	C_{51}	0.9113	C_{83}	0.4233	C_{115}	1.2153
C_{20}	1.5406	C_{52}	0.8454	C_{84}	0.6741	C_{116}	1.5783
C_{21}	-1.4613	C_{53}	-0.8866	C_{85}	-1.0157	C_{117}	-0.7718
C_{22}	1.2745	C_{54}	0.8852	C_{86}	0.8304	C_{118}	1.2384
C_{23}	0.3715	C_{55}	0.4918	C_{87}	0.4878	C_{119}	0.6695
C_{24}	1.8134	C_{56}	-0.6096	C_{88}	-1.4992	C_{120}	0.8821
C_{25}	0.9438	C_{57}	-0.4322	C_{89}	-1.1884	C_{121}	0.7808
C_{26}	1.3130	C_{58}	-0.1327	C_{90}	-1.4008	C_{122}	1.0537
C_{27}	-1.3070	C_{59}	0.4953	C_{91}	0.7795	C_{123}	-0.0791
C_{28}	-1.3462	C_{60}	0.9702	C_{92}	1.2926	C_{124}	-0.2845
C_{29}	1.6868	C_{61}	-0.8667	C_{93}	-1.2049	C_{125}	0.5790
C_{30}	-1.2153	C_{62}	0.6803	C_{94}	1.2934	C_{126}	-0.4664
C_{31}	-0.6778	C_{63}	-0.0244	C_{95}	0.8123	C_{127}	-0.1097

Table A.14: Time-domain Packet Synchronization Sequence for Preamble Pattern 5.

Index	Value	Index	Value	Index	Value	Index	Value
C_0	0.9574	C_{32}	0.8400	C_{64}	0.5859	C_{96}	-0.8528
C_1	0.5270	C_{33}	1.3980	C_{65}	0.3053	C_{97}	-0.6973
C_2	1.5929	C_{34}	1.1147	C_{66}	0.8948	C_{98}	-1.2477
C_3	-0.2500	C_{35}	-0.4732	C_{67}	-0.6744	C_{99}	0.6246
C_4	-0.2536	C_{36}	-1.7178	C_{68}	-0.8901	C_{100}	0.7687
C_5	-0.3023	C_{37}	-0.8477	C_{69}	-0.8133	C_{101}	0.7966
C_6	1.2907	C_{38}	1.5083	C_{70}	0.9201	C_{102}	-1.2809
C_7	-0.4258	C_{39}	-1.4364	C_{71}	-1.0841	C_{103}	1.1023
C_8	1.0012	C_{40}	0.3853	C_{72}	-0.8036	C_{104}	0.4250
C_9	1.7704	C_{41}	1.5673	C_{73}	-0.3105	C_{105}	-0.1614
C_{10}	0.8593	C_{42}	0.0295	C_{74}	-1.0514	C_{106}	0.7547
C_{11}	-0.3719	C_{43}	-0.4204	C_{75}	0.7644	C_{107}	-0.6696
C_{12}	-1.3465	C_{44}	-1.4856	C_{76}	0.7301	C_{108}	-0.3920
C_{13}	-0.7419	C_{45}	-0.8404	C_{77}	0.9788	C_{109}	-0.7589
C_{14}	1.5350	C_{46}	1.0111	C_{78}	-1.1305	C_{110}	0.6701
C_{15}	-1.2800	C_{47}	-1.4269	C_{79}	1.3257	C_{111}	-0.9381
C_{16}	0.6955	C_{48}	0.3033	C_{80}	0.7801	C_{112}	-0.7483
C_{17}	1.7204	C_{49}	0.7757	C_{81}	0.7867	C_{113}	-0.9659
C_{18}	0.1643	C_{50}	-0.1370	C_{82}	1.0996	C_{114}	-0.9192
C_{19}	-0.3347	C_{51}	-0.5250	C_{83}	-0.5623	C_{115}	0.3925
C_{20}	-1.7244	C_{52}	-1.1589	C_{84}	-1.2227	C_{116}	1.2864
C_{21}	-0.7447	C_{53}	-0.8324	C_{85}	-0.8223	C_{117}	0.6784
C_{22}	1.1141	C_{54}	0.6336	C_{86}	1.2074	C_{118}	-1.0909
C_{23}	-1.3541	C_{55}	-1.2698	C_{87}	-1.2338	C_{119}	1.1140
C_{24}	0.7293	C_{56}	-0.7853	C_{88}	0.2957	C_{120}	-0.6134
C_{25}	0.2682	C_{57}	-0.7031	C_{89}	1.0999	C_{121}	-1.5467
C_{26}	1.2401	C_{58}	-1.1106	C_{90}	-0.0201	C_{122}	-0.3031
C_{27}	1.0527	C_{59}	0.6071	C_{91}	-0.5860	C_{123}	0.9457
C_{28}	0.1199	C_{60}	0.7164	C_{92}	-1.2284	C_{124}	1.9645
C_{29}	1.1496	C_{61}	0.8305	C_{93}	-0.9215	C_{125}	1.4549
C_{30}	-1.0544	C_{62}	-1.2355	C_{94}	0.7941	C_{126}	-1.2760
C_{31}	1.3176	C_{63}	1.1754	C_{95}	-1.4128	C_{127}	2.2102

Table A.15: Frequency Domain Channel Estimation Preamble Sequence.

Tone	Value	Tone	Value	Tone	Value	Tone	Value
-61	$(-1+j)/\sqrt{2}$	-30	$(1-j)/\sqrt{2}$	1	$(1+j)/\sqrt{2}$	32	$(1+j)/\sqrt{2}$
-60	$(-1+j)/\sqrt{2}$	-29	$(-1+j)/\sqrt{2}$	2	$(1+j)/\sqrt{2}$	33	$(1+j)/\sqrt{2}$
-59	$(-1+j)/\sqrt{2}$	-28	$(-1+j)/\sqrt{2}$	3	$(-1-j)/\sqrt{2}$	34	$(-1-j)/\sqrt{2}$
-58	$(-1+j)/\sqrt{2}$	-27	$(1-j)/\sqrt{2}$	4	$(1+j)/\sqrt{2}$	35	$(-1-j)/\sqrt{2}$
-57	$(-1+j)/\sqrt{2}$	-26	$(1-j)/\sqrt{2}$	5	$(-1-j)/\sqrt{2}$	36	$(1+j)/\sqrt{2}$
-56	$(1-j)/\sqrt{2}$	-25	$(1-j)/\sqrt{2}$	6	$(-1-j)/\sqrt{2}$	37	$(-1-j)/\sqrt{2}$
-55	$(1-j)/\sqrt{2}$	-24	$(-1+j)/\sqrt{2}$	7	$(1+j)/\sqrt{2}$	38	$(1+j)/\sqrt{2}$
-54	$(-1+j)/\sqrt{2}$	-23	$(1-j)/\sqrt{2}$	8	$(-1-j)/\sqrt{2}$	39	$(1+j)/\sqrt{2}$
-53	$(1-j)/\sqrt{2}$	-22	$(1-j)/\sqrt{2}$	9	$(1+j)/\sqrt{2}$	40	$(1+j)/\sqrt{2}$
-52	$(1-j)/\sqrt{2}$	-21	$(1-j)/\sqrt{2}$	10	$(-1-j)/\sqrt{2}$	41	$(-1-j)/\sqrt{2}$
-51	$(1-j)/\sqrt{2}$	-20	$(-1+j)/\sqrt{2}$	11	$(1+j)/\sqrt{2}$	42	$(-1-j)/\sqrt{2}$
-50	$(1-j)/\sqrt{2}$	-19	$(1-j)/\sqrt{2}$	12	$(1+j)/\sqrt{2}$	43	$(1+j)/\sqrt{2}$
-49	$(1-j)/\sqrt{2}$	-18	$(-1+j)/\sqrt{2}$	13	$(-1-j)/\sqrt{2}$	44	$(1+j)/\sqrt{2}$
-48	$(-1+j)/\sqrt{2}$	-17	$(1-j)/\sqrt{2}$	14	$(-1-j)/\sqrt{2}$	45	$(-1-j)/\sqrt{2}$
-47	$(1-j)/\sqrt{2}$	-16	$(1-j)/\sqrt{2}$	15	$(-1-j)/\sqrt{2}$	46	$(-1-j)/\sqrt{2}$
-46	$(-1+j)/\sqrt{2}$	-15	$(-1+j)/\sqrt{2}$	16	$(1+j)/\sqrt{2}$	47	$(1+j)/\sqrt{2}$
-45	$(-1+j)/\sqrt{2}$	-14	$(-1+j)/\sqrt{2}$	17	$(1+j)/\sqrt{2}$	48	$(-1-j)/\sqrt{2}$
-44	$(1-j)/\sqrt{2}$	-13	$(-1+j)/\sqrt{2}$	18	$(-1-j)/\sqrt{2}$	49	$(1+j)/\sqrt{2}$
-43	$(1-j)/\sqrt{2}$	-12	$(1-j)/\sqrt{2}$	19	$(1+j)/\sqrt{2}$	50	$(1+j)/\sqrt{2}$
-42	$(-1+j)/\sqrt{2}$	-11	$(1-j)/\sqrt{2}$	20	$(-1-j)/\sqrt{2}$	51	$(1+j)/\sqrt{2}$
-41	$(-1+j)/\sqrt{2}$	-10	$(-1+j)/\sqrt{2}$	21	$(1+j)/\sqrt{2}$	52	$(1+j)/\sqrt{2}$
-40	$(1-j)/\sqrt{2}$	-9	$(1-j)/\sqrt{2}$	22	$(1+j)/\sqrt{2}$	53	$(1+j)/\sqrt{2}$
-39	$(1-j)/\sqrt{2}$	-8	$(-1+j)/\sqrt{2}$	23	$(1+j)/\sqrt{2}$	54	$(-1-j)/\sqrt{2}$
-38	$(1-j)/\sqrt{2}$	-7	$(1-j)/\sqrt{2}$	24	$(-1-j)/\sqrt{2}$	55	$(1+j)/\sqrt{2}$
-37	$(-1+j)/\sqrt{2}$	-6	$(-1+j)/\sqrt{2}$	25	$(1+j)/\sqrt{2}$	56	$(1+j)/\sqrt{2}$
-36	$(1-j)/\sqrt{2}$	-5	$(-1+j)/\sqrt{2}$	26	$(1+j)/\sqrt{2}$	57	$(-1-j)/\sqrt{2}$
-35	$(-1+j)/\sqrt{2}$	-4	$(1-j)/\sqrt{2}$	27	$(1+j)/\sqrt{2}$	58	$(-1-j)/\sqrt{2}$
-34	$(-1+j)/\sqrt{2}$	-3	$(-1+j)/\sqrt{2}$	28	$(-1-j)/\sqrt{2}$	59	$(-1-j)/\sqrt{2}$
-33	$(1-j)/\sqrt{2}$	-2	$(1-j)/\sqrt{2}$	29	$(-1-j)/\sqrt{2}$	60	$(-1-j)/\sqrt{2}$
-32	$(1-j)/\sqrt{2}$	-1	$(1-j)/\sqrt{2}$	30	$(1+j)/\sqrt{2}$	61	$(-1-j)/\sqrt{2}$
-31	$(1-j)/\sqrt{2}$			31	$(1+j)/\sqrt{2}$		

References

[1] FCC 02-48 First Report and Order In the Matter of Revision of Part 15 of the Commission’s Rules Regarding Ultra-Wideband Transmission Systems, adopted Feb 14, 2002.

[2] Robert J. Fontana, “Recent System Applications of Short-Pulse Ultra-Wideband (UWB) Technonlogy”, *IEEE Transactions on Microwave Theory and Techniques*, vol. 52, no. 9, pp. 2087-2104, Sept 2004.

[3] Discrete Time Communications, “New” ultra-wideband technology, White Paper, Oct 2002.

[4] IEEE 802.15 High Rate Alternative PHY Task Group (TG3a) for Wireless Personal Area Networks, ”Multi-band OFDM Physical Layer Proposal for IEEE 802.15 Task Group 3a” IEEE P802.15-03/268r1.

[5] Lajos Hanzo, Matthias Munster, Byoung-Jo Choi and Thomas Keller, OFDM and MC-CDMA for Broadband Multi-user Communications, WLANs and Broadcasting, IEEE Press and John Wiley & Sons Ltd, West Sussex, 2003.

[6] Richard van Nee and Ramjee Prasad, OFDM for wireless multimedia communications, Artech House, Boston, 2000.

[7] T. Pollet, M. Van Bladel, and M. Moeneclaey, “BER sensitivity of OFDM systems to carrier frequency offset and Wiener phase noise”, *IEEE Transactions on Communications*, vol. 43, no. 234, pp 191-193, Feb./Mar/Apr 1995.

[8] H. Nishookar and R. Prasad, “On the sensitivity of multicarrier transmission over multipath channels to phase noise and frequency offset”, *IEEE International Symposium on Personal, Indoor and Mobile Radio Communications* (PIMRC'96), vol. 1, pp 68-72, Oct 1996.

[9] T. Pollet, P. Spruyt and M. Moeneclaey, “The BER performance of OFDM systems using non-synchronized sampling”, *IEEE Global Telecommunications Conference* (GLOBECOM '94), pp 253 – 257, Dec 1994.

[10] A. Molisch, J.R. Forester and M. Pendergrass, “Channel models for ultra-wideband personal area networks”, *IEEE Transactions on Wireless Communications*, vol. 10, pp. 14–21, December 2003.

[11] A. Saleh and R. Valenzuela, "A statistical model for indoor multipath propagation", *IEEE Journal on Selected Areas in Communications*, vol. SAC-5, no. 2, pp. 128–137, Feb 1987.

[12] R. G. Gallager, "Low density parity check codes", *IRE Transactions on Information Theory*, vol. IT-8, pp. 21–28, January 1962.

[13] D. J. C. Mackay and R. M. Neal, "Near shannon limit performance of low density parity check codes", *Electonics Letters*, vol. 32, no. 18, pp. 1645–1646, August 1996.

[14] D. J. C. Mackay, "Good error-correcting codes based on very sparse matrices", *IEEE Transactions on Information Theory*, vol. 45, pp. 399–431, March 1999.

[15] H. Futaki and T. Ohtsuki, "Performance of low-density parity check coded ofdm systems", *IEEE International Conference* (ICC 2002), vol. 3, pp. 1696–1700, 2002.

[16] T. Richardson, M. Shokrollahi, and R. Urbanke, "Design of capacity-approaching irregular low-density parity-check codes", *IEEE Transaction on Information Theory*, vol. 47, pp. 619–637, Feb 2001.

[17] T. Zhang and K. K. Parhi, "VLSI implementation-oriented (3,k)-regular low-density parity-check codes," *2001 IEEE Workshop on Signal Processing Systems*, pp. 25–36, Sep 2001.

[18] Png Khiam Boon, Peng Xiaoming and Francois Chin, "Performance Studies of a Multi-band OFDM System Using a Simplified LDPC Code", *Proceedings of Joint UWBST & IWUWBS 2004*, pp 376-380, May 2004.

[19] S. Hara and R. Prasad, "Design and performance of multicarrier cdma system in frequency-selective rayleigh fading channels," *IEEE Transactions on Vehicular Technology*, vol. 48, pp. 1584–1594, Sep 1999.

[20] J. P. L. N. Yee and G. Fettweis, "Multi-carrier cdma in indoor wireless radio networks," *Proceedings PIMRC 1993*, vol. 1, pp. 109 –113, 1993.

[21] X. Peng, A. Madhukumar, and F. Chin, "Performance studies of interleaving schemes for mc-cdma systems," *IEEE Wireless Communications and Networking Conference (WCNC), 2004*, vol. 4, pp. 2081– 2086, March 2004.

[22] A. B. A. Chouly and S. Jourdan, "Othogonal multicarrier techniques applied to direct sequence spread spectrum cdma systems," *IEEE GLOBECOM 1993*, pp. 1723–1728, Nov 1993.

[23] R. Raulefs, A. Dammann, S. Sand, S. Kaiser, and G. Auer, “Rotated walsh-hadamard spreading with robust channel estimation for a coded MC-CDMA system,” *EURASIP Journal on Wireless Communication and Networking*, vol. 1, pp. 74–83, Aug 2004.

[24] P.H. Moose, “A Technique for Orthogonal Frequency Division Multiplexing Frequency Offset Correction”, *IEEE Transactions on Communications*, vol. 42, pp 2908-2914, Oct 1994.

[25] Wen Lei, Weiming Cheng, Liming Sun, “Improved Joint Carrier and Sampling Frequency Offset Estimation Scheme for OFDM Systems”, *IEEE Global Telecommunications Conference* (GLOBECOM '03), vol. 4, pp 2315-2319, Dec 2003.

[26] M. Sliskovic, “Carrier and Sampling Frequency Offset Estimation and Correction in Multicarrier Systems”, *IEEE Global Telecommunications Conference* (GLOBECOM '01), vol. 1, pp 285 - 289, Nov 2001.

[27] Fu Yanzeng, Zhang Hailin and Wang Yumin, “Frequency synchronization in OFDM systems”, *2nd International Conference on 3G Mobile Communication Technologies, 2001*, No. 477, pp 92-98, Mar 2001.

[28] T.M. Schmidl and C.C. Donald, “Robust Frequency and Timing Synchronization for OFDM”, *IEEE Transactions on Communications*, vol. 45, pp 1613-1621, Dec 1997.

[29] F.M. Gardner, “Interpolation in Digital Modems - Part I: Fundamentals”, *IEEE Transactions on Communications*, Vol. 41, pp 501-507, Mar 1993.

[30] Eric W. Weisstein. "Least Squares Fitting", from *MathWorld – A Wolfram Web Resource,* http://mathworld.wolfram.com/LeastSquaresFitting.html

[31] John G. Proakis, Digital Communications, McGraw-Hill Book Co – Singapore, 4th Edition, Singapore, 2001.

[32] Roger L. Peterson, Rodger E. Ziemer and David E. Borth, Introduction to Spread Spectrum Communications, Prentice Hall Inc., Upper Saddle River, New Jeresy, 1995.

[33] J.-J van de Beek, O. Edfors, M. Sandell, S.K. Wilson and P.O. Borjesson, “On Channel Estimation in OFDM System”, *IEEE 45th Vehicular Technology Conference*, Vol. 2, pp 815-819, Jul 1995.

[34] O. Edfors, M. Sandell, J.-J van de Beek, S. Wilson and P.O. Borjesson, “OFDM Channel Estimation by Singular Value Decomposition”, *IEEE Transactions on Communications*, Vol. 2, pp 501-507, Mar 1993.

List of Publications

Below are some papers that are based on the results of this thesis and have been published, submitted or will be submitted.

[1] Png Khiam Boon, Peng Xiaoming and Francois Chin, "Performance Studies of a Multi-band OFDM System Using a Simplified LDPC Code", *Proceedings of Joint UWBST & IWUWBS 2004*, pp 376-380, May 2004.

[2] Png Khiam Boon, Peng Xiaoming, Fu Hongyi and Francois Chin, "A Two-dimensional Estimation Method of Sampling Frequency Offset using Subcarrier Pilot for an MB-OFDM UWB System". Prepared for ICC 2006.

[3] Peng Xiaoming Png Khiam Boon, and Francois Chin, "Performance Improvement of Chip Interleaved Scheme for MB-OFDM system for 480 Mbps". submitted to PIMRC 2005.

[4] Peng Xiaoming, Png Khiam Boon, Fu Hongyi and Francois Chin, "A Two-dimensional Estimation Method of Sampling Frequency Offset using Subcarrier Pilot for an MB-OFDM UWB System". Prepared for IEEE Transaction on Vehicular Technology.

Notes

Please note that parts of this thesis have been submitted for patent application.